

# Elliptic flow at different collision stages



ANDREA DUBLA

A catalogue record is available from Utrecht University Library

ISBN: 978-90-393-6524-3

Copyright © 2016 by A. Dubla All rights reserved. No part of this book may be reproduced, stored in a database or retrieval system, or published, in any form or in any way, electronically, mechanically, by print, photoprint, microfilm or any other means without prior written permission of the author.

Typeset using L<sup>A</sup>T<sub>E</sub>X

# Elliptic flow at different collision stages

Elliptische stroming tijdens verschillende botsingsstadia  
(met een samenvatting in het Nederlands)

Proefschrift

ter verkrijging van de graad van doctor aan de Universiteit Utrecht op  
gezag van de rector magnificus, prof. dr. G.J. van der Zwaan, ingevolge  
het besluit van het college voor promoties in het openbaar te verdedigen  
op woensdag 6 april 2016 des middags te 2:30 uur

ANDREA DUBLA

geboren op 18 april 1985 te Turijn, Italië

**Promotor:** Prof.dr. R.J.M. Snellings  
**Copromotor:** Dr. A. Grelli

*And sometimes you close your eyes  
and see the place where you used to live  
when you were young...*



---

---

# Contents

---

---

<b>Introduction</b>	<b>1</b>
<b>1 Heavy Ion physics</b>	<b>3</b>
1.1 Quantum ChromoDynamics . . . . .	3
1.2 The QCD phase diagram . . . . .	4
1.3 Evolution of the collision . . . . .	6
1.3.1 Different collision stages . . . . .	6
1.4 Anisotropic flow as experimental observable . . . . .	8
1.4.1 Radial Flow . . . . .	10
1.4.2 Elliptic Flow . . . . .	11
1.5 Soft Probes . . . . .	13
1.6 Hard Probes . . . . .	18
1.7 Electromagnetic Probes . . . . .	24
<b>2 The ALICE experiment</b>	<b>33</b>
2.1 Detector design . . . . .	33
2.2 Inner Tracking System . . . . .	36
2.3 Time Projection Chamber . . . . .	40
2.4 Time of Flight . . . . .	42
2.5 Electromagnetic Calorimeter . . . . .	44

2.6	VZERO detector . . . . .	45
<b>3</b>	<b>Flow analysis methodologies</b>	<b>47</b>
3.1	Event plane method . . . . .	48
3.1.1	Event plane with three sub-events resolution . . . . .	50
3.2	Scalar product method . . . . .	51
3.2.1	Scalar product with three sub-events . . . . .	53
3.3	Q-Cumulant and multi-particle correlation . . . . .	53
<b>4</b>	<b>Event selection</b>	<b>55</b>
4.1	On-line and Off-line event selection . . . . .	56
4.1.1	Additional event selection . . . . .	57
4.2	Centrality determination . . . . .	59
4.2.1	Centrality flattening for the 2011 data . . . . .	60
4.3	Event plane determination . . . . .	63
4.3.1	Further correction in most central collision . . . . .	66
4.4	EMCal Trigger studies . . . . .	67
<b>5</b>	<b>Elliptic flow of <math>\phi</math>-mesons</b>	<b>73</b>
5.1	Two particle resonance flow . . . . .	74
5.2	$\phi$ -meson reconstruction . . . . .	76
5.2.1	Track selection . . . . .	76
5.2.2	Bayesian particle identification . . . . .	78
5.2.3	Combinatorial background estimation . . . . .	81
5.2.4	Signal extraction . . . . .	84
5.3	Invariant mass fit method and $v_2^\phi(p_T)$ . . . . .	90
5.4	Systematic studies on $\phi$ -meson $v_2$ . . . . .	92
5.5	Results and discussion . . . . .	94
5.5.1	Comparison with other particle species . . . . .	95
5.5.2	The meson-baryon scaling at LHC . . . . .	97
5.5.3	Comparison with hydrodynamical model . . . . .	100

---

## CONTENTS

---

<b>6</b>	<b>Elliptic flow of heavy-flavour decay electrons</b>	<b>105</b>
6.1	Inclusive electron identification . . . . .	106
6.1.1	ITS–TOF–TPC . . . . .	107
6.1.2	TPC–EMCal . . . . .	110
6.1.3	Inclusive electron purity . . . . .	112
6.1.4	Inclusive electron $v_2$ . . . . .	119
6.1.5	Systematic uncertainties . . . . .	120
6.2	Photonic electron background . . . . .	124
6.2.1	Invariant mass method . . . . .	124
6.2.2	Photonic electron reconstruction efficiency . . . . .	127
6.2.3	$(1 + R_{SB})$ and systematic uncertainties . . . . .	131
6.2.4	Background $v_2$ . . . . .	134
6.2.5	Cocktail simulation method . . . . .	136
6.2.6	Late photon conversions . . . . .	139
6.3	Heavy-flavour decay electrons measurements . . . . .	143
6.3.1	Model comparison . . . . .	147
<b>7</b>	<b>Elliptic flow of direct photons</b>	<b>149</b>
7.1	Inclusive photon reconstruction . . . . .	150
7.1.1	Electron identification . . . . .	150
7.1.2	Topological cut selection . . . . .	151
7.1.3	Purity and efficiency . . . . .	155
7.1.4	Inclusive photon $v_2$ . . . . .	156
7.1.5	Systematic uncertainties . . . . .	158
7.2	Photon conversion background . . . . .	159
7.2.1	Photon background $v_2$ . . . . .	159
7.2.2	Double ratio . . . . .	161
7.3	Direct photon measurements . . . . .	162
7.3.1	Model comparison . . . . .	163
7.4	Ongoing and future activities . . . . .	165
	<b>Conclusion</b>	<b>169</b>
	<b>Bibliography</b>	<b>174</b>

---



---

---

# Introduction

---

---

ALICE (A Large Ion Collider Experiment) is one of the four main experiments at the Large Hadron Collider (LHC) optimized for the study of heavy-ion collisions. The prime aim of the experiment is to study in detail the behaviour of nuclear matter at high densities and temperatures. In ALICE also proton-proton collisions are studied both as a reference for lead-lead collisions and in physics areas where ALICE is competitive, like the low  $p_T$  region, with other LHC experiments.

In order to characterise the system produced in heavy-ion collisions, it is necessary to use a wide variety of experimentally accessible observables, which can help to disentangle the different physical mechanisms that characterise the various collision stages. Among the different experimental observables, the focus of this thesis will be on anisotropic flow, one of the most important experimental observables used in heavy-ion collisions to study the properties of the QGP.

For this purpose, a comprehensive study of the elliptic flow of hadrons, electrons from heavy-flavour hadron decays, and direct photons, all which are assumed to interact differently with medium, has been carried out. The  $v_2$  coefficient of low  $p_T$  hadrons, mainly coming from the hadronization of soft partons within the bulk, carries information on the hydrodynamic properties of the partonic medium created in heavy-ion collisions. Among

the different hadron species, the  $\phi$ -meson is of great interest because it is predicted to have a small hadronic cross section, and is therefore less affected by the interactions between hadrons during the hadronization phase of the collision. Furthermore the  $v_2$  coefficient allows to study the interaction strength of heavy-quarks with the expanding medium and their possible thermalisation in the medium itself. Due to their large masses, heavy quarks are produced at the initial stage of the collision, almost exclusively in hard partonic scattering processes. Therefore, they experience the full evolution of the system, propagating through the hot and dense medium and losing energy via radiative and collisional scattering processes. Thus heavy-flavour hadrons and their decay products are effective probes to study the properties of the medium created in the heavy-ion collisions. Direct photons on the other hand, since they do not interact with the strongly-coupling medium created in these collisions, carry undistorted information about the system at their production time. The elliptic flow of direct photons strongly depends on the production mechanism. Small flow would be associated with early production while a large, hadron-like flow, would point towards late production in the medium.

---

---

# Chapter 1

## Heavy Ion physics

---

---

### 1.1 Quantum ChromoDynamics

The strong interaction, the force that binds the nucleons in the nucleus, is a residual force of another fundamental interaction (*Quantum ChromoDynamics*) that acts on the quarks and gluons, the constituents of the nucleons.

One of the fundamental properties of QCD is the dependence of the coupling constant of the interaction on the energy scale involved in the process (*running coupling*). Calculations in perturbative QCD give us the evolution of the coupling with the momentum transferred  $Q^2$  [1], which is shown in the Eq. 1.1:

$$\alpha_s(Q^2) = \frac{12\pi}{(33 - 2N_f) \ln \frac{Q^2}{\Lambda_{QCD}^2}}, \quad (1.1)$$

with the QCD scale parameter  $\Lambda_{QCD} \approx 200$  MeV and the number of flavours  $N_f$ .

It clearly exhibits asymptotic freedom from the fact that the coupling decreases for high  $Q^2$ . On the other hand,  $\alpha_s$  increases for smaller  $Q^2$  and diverges when  $Q^2$  approaches  $\Lambda_{QCD}$ .

Unfortunately, the largeness of  $\alpha_s$  calls into question the usage of perturbation theory, and by this makes the equation above unreliable for small  $Q^2$ . Thus it is not possible to directly predict the quantitative behaviour this way apart from the fact that the coupling does increase, which is likely related to the experimentally observed confinement of colour charges.

In this case QCD can not be calculated using perturbative methods. Lattice-QCD (LQCD) [2] is a non perturbative treatment of QCD, formulated on a discrete space-time lattice. LQCD provides a quantitative understanding of the new phase of matter at high temperature and allows to study quark and gluon interactions over a large distance scale.

## 1.2 The QCD phase diagram

LQCD predicts a phase transition between hadronic matter and the *Quark Gluon Plasma* (QGP), where the confinement of partons is resolved.

Depending upon the temperature  $T$  and on the chemical potential  $\mu_B$ , the strongly interacting matter is expected to be in different phases. This is shown in a sketch of the QCD phase diagram in Fig. 1.1.

At low temperatures and for  $\mu_B \sim 1$  GeV (corresponding to the nuclear density) there is the ordinary hadronic matter. For sufficiently high values of the baryo-chemical potential, the system exhibits a first order transition between hadronic matter and the QGP [3]. LQCD calculations at non-zero chemical potential [2] suggest the existence of a critical point  $(\mu_{B,c}, T_c)$ , such that the transition is no longer first-order for  $\mu_B < \mu_{B,c}$ . Recent calculations [4], suggest that the transition at low values of the baryo-chemical potential is not a phase transition, but rather a rapid crossover that occurs in a small, well defined, temperature interval.

In the early universe, the transition from a QGP to hadrons occurred at vanishing baryo-chemical potential and high temperatures during a rapid expansion and cooling. In the neutron stars the QGP state is expected to be

## 1.2 The QCD phase diagram

---

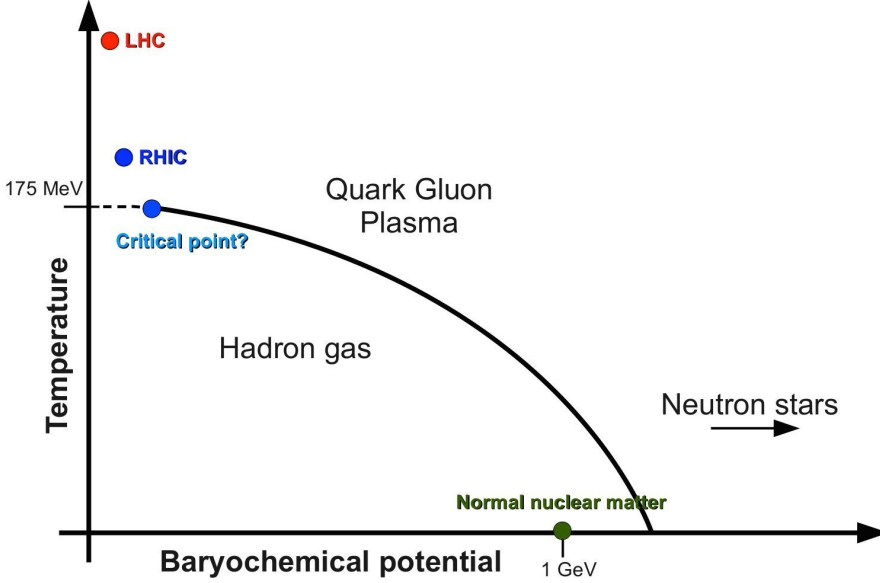


Figure 1.1: Sketch of the phase diagram of nuclear matter. Different phases of nuclear matter, beside the QGP, are presented and the regions explored with heavy ion collisions at RHIC and LHC are indicated.

formed for high values of the baryo-chemical potential and at a temperature close to zero, due to the gravitational collapse. In both cases the deconfined phase of hadronic matter appears to play an important role. Nowadays the region of high  $T$  and low  $\mu_B$  is investigated with relativistic heavy-ion collisions at accelerators like the Relativistic Heavy Ion Collider (RHIC) and the Large Hadron Collider (LHC). The high  $\mu_B$  and  $T \sim 0$  regime is indirectly investigated in the context of astrophysical studies [5].

### 1.3 Evolution of the collision

Concepts like a phase transition and temperature are properly defined for systems composed of many particles. Those extended system can be described by thermodynamical and hydrodynamical laws. The experimental tools for creating deconfined matter are heavy-ion collisions, which satisfy the following requirements:

- the number of constituents of the system is large (thousands of particles), therefore the system might be described by macroscopic variables;
- the system is long-lived compared to the typical time-scales of the strong interactions ( $\sim 1 \text{ fm}/c$  [6]) and thus might reach equilibrium.

With the increase of center-of-mass energy of the colliding system, the initial conditions in the collision region change gradually from 'baryon rich' to 'baryon free'. At center-of-mass energies of around  $\sqrt{s_{NN}} = 10 \text{ GeV}$ , incoming nucleons lose a substantial part of their initial energy in multiple collisions and are likely to be stopped in the collision region. This leads to a high baryonic content and therefore to a large  $\mu_B$  of the system. However, when the center-of-mass energy is high enough ( $\sqrt{s_{NN}} > 100 \text{ GeV}$ ), the stopping power is not sufficient to stop incoming nucleons and they escape from the interaction region after releasing a fraction of their energy. In this situation, the mid-rapidity region is 'baryon free' and the system is closer to the conditions of the early universe.

#### 1.3.1 Different collision stages

A good understanding of the evolution of the system created in heavy-ion collision is necessary to study the properties of the QGP, and can be reached using various experimental observables. The evolution of the system created in the collision of two nuclei can be divided into different phases shown in Fig. 1.2.

### 1.3 Evolution of the collision

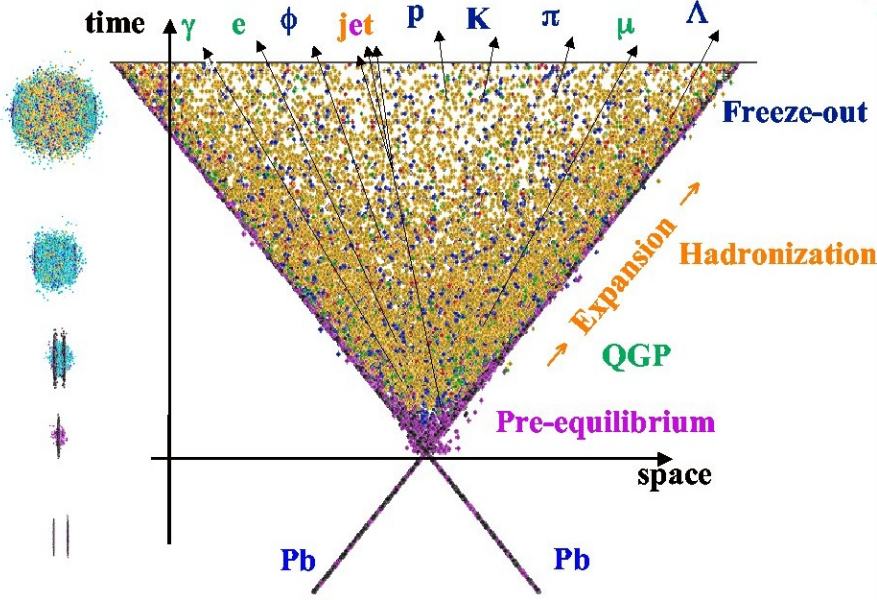


Figure 1.2: space-time evolution according to Bjorken's hydrodynamic model [7].

- **Pre-equilibrium**( $\tau < \tau_{th}$ )  $\rightarrow$  hard processes occur during the parton scattering, leading to the creation of high- $p_T$  probes, like jets, heavy quarks, direct photons.
- **Thermalization and QGP phase**( $\tau_{th} \sim 1 \text{ fm}/c$ )  $\rightarrow$  multiple scatterings among the constituents of the system created in the collision lead to thermal equilibrium after a certain time  $\tau_{th}$ . If the energy density is high enough ( $\varepsilon_c \sim 1 \text{ GeV}/\text{fm}^3$ ), the mean free path in the interacting system is expected to be small compared to the system size and the resulting thermalized QGP expands hydrodynamically and cools down due to the expansion of the system.

- **Hadronization**  $\rightarrow$  temperature of the expanding medium decreases and, when it goes below the critical temperature  $T_c$ , a transition takes place and the quarks and gluons are again confined into ordinary hadrons. The system can still be in local thermal equilibrium because inelastic interactions take place.
- **Chemical freeze-out**  $\rightarrow$  further expansion and dropping temperature leads to the inelastic processes among hadrons to cease. At this instant, the relative abundances of hadron species are fixed.
- **Kinetic freeze-out**  $\rightarrow$  At this stage the momentum spectra of the produced particles are fixed because the elastic collisions cease.

In order to characterize the system produced in heavy-ion collisions as a state of matter, it is necessary to determine its parameters, such as temperature, chemical potential, flow velocity and equation of state. The parameters can be inferred from a wide variety of experimentally accessible observables, which can help to disentangle the different physical mechanisms that characterize the various collision stages. This is nicely depicted in Fig. 1.2 where the different particle names are shown in different colours also used to display the stage of the collision from which they carry information. Among the several experimental observables, the focus of this thesis will be on the anisotropic flow, one of the most important experimental observables used in heavy ion collision to study the properties of the QGP.

### 1.4 Anisotropic flow as experimental observable

Measurements of the collective expansion of the matter created in heavy-ion collisions, nowadays spanning collision energies from a few MeV up to several TeV per nucleon pair, have proven to be one of the best ways to study in detail the properties of the QGP. Heavy ions are extended objects and the system created in a head-on collision is different from that in a peripheral collisions<sup>1</sup>. The geometry of the collision between two nuclei is

---

<sup>1</sup>concept as collision centrality will be explained in detail in chapter 4

## 1.4 Anisotropic flow as experimental observable

---

schematically represented in Fig. 1.3, seen in the plane transverse to the beam direction ( $z$  axis). One of the most relevant quantities, that defines the overall geometry of the collision is the impact parameter vector  $b$ , that is the vector defined by the centres of the two colliding nuclei in the transverse plane.

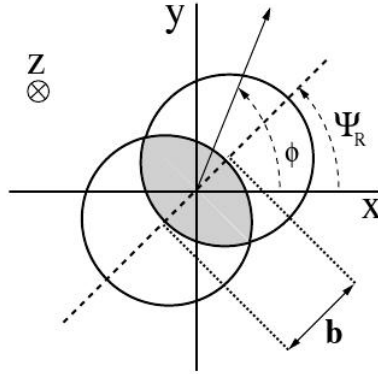


Figure 1.3: Schematic view of the collision geometry as seen in the plane transverse to the beam direction ( $z$  axis). See text for details.

In the most central collisions (small impact parameter  $b$ ) the spatial distribution of the created system is approximately azimuthal symmetric, resulting in a symmetric expansion called radial flow. However, in non-central heavy-ion collisions, an initially asymmetric overlap region is created, which gives rise to anisotropic flow. Due to the pressure gradients, the almond shaped region tends to assume a more symmetric shape as the system expands and cools down. If the particles produced in the collision are subject to a large number of rescatterings in the overlap region, the spatial anisotropy is converted into a momentum anisotropy of the produced particles with respect to the reaction plane ( $\Psi_R$ ), which is the plane defined by the beam axis and the impact parameter. This particle anisotropy is observed experimentally with anisotropic flow measurements, which provide information on the properties of the QGP and on the energy loss mecha-

nisms for high- $p_T$  partons when traversing the medium.

### 1.4.1 Radial Flow

At chemical freeze-out, hadronic abundances are fixed, but spectral shapes can be modified in the subsequent hadronic phase due to elastic scatterings, which are expected to occur until the kinetic freeze-out.

The shape of the low  $p_T$  spectrum of each particle shows an almost exponential shape, typical of a thermal spectrum:

$$\frac{d^2N}{m_T dm_T dy} = e^{-\frac{m_T}{T_{slope}}} \quad (1.2)$$

where  $m_T = \sqrt{p_T^2 + m_i^2}$  is the transverse mass,  $m_i$  is the particle mass,  $y = \ln((E + p_L)/(E - p_L))$  is the particle rapidity and  $T_{slope}$  is the parameter that represent the slope of the  $p_T$  distribution. For an expanding system  $T_{slope}$  depends on the temperature at kinetic freeze-out ( $T_{kin}$ ) and on the expansion velocity of the system ( $\langle v_\perp \rangle$ ). In nuclear collisions this expansion is called *radial flow* [8] and  $T_{slope}$ , in a non-relativistic case, has the form:

$$T_{slope} = T_{kin} + \frac{1}{2} m_i \langle v_\perp \rangle^2 \quad (1.3)$$

In Fig. 1.4 the spectra for  $\pi^\pm$ ,  $K^\pm$ ,  $p$ , and  $\bar{p}$  for pp and for several centrality classes in Au–Au collisions within  $|y| < 0.1$  are reported as measured by the STAR Collaboration at  $\sqrt{s_{NN}} = 200$  GeV [9]. While the pion spectra shapes are similar for pp and Au–Au, the kaon and proton spectra show a progressive flattening from pp to the most central Au–Au events. A two parameter fit from RHIC data gives a thermal freeze-out temperature  $T_{kin} \sim 90$  MeV and a value of  $\beta_\perp = v_\perp/c \sim 0.55$  for the most central events. In minimum bias pp collisions, the  $T_{slope}$  parameter assumes the same value for each specie indicating the absence of transverse collective flow.

Radial flow is a collective phenomenon which affects all hadrons produced in a heavy-ion collision depending on their mass. It is observed as

## 1.4 Anisotropic flow as experimental observable

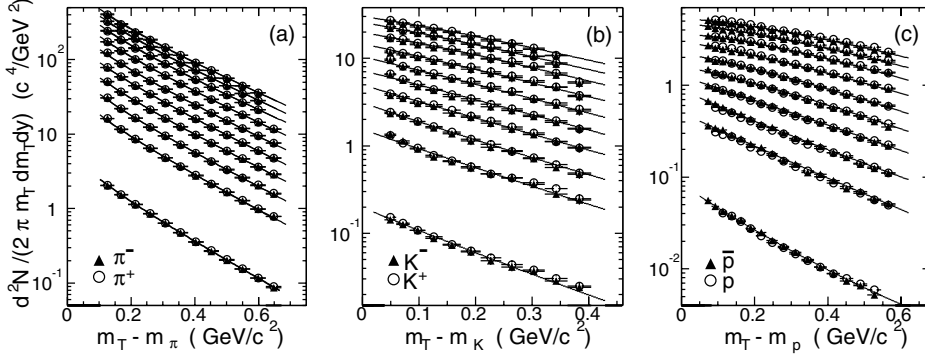


Figure 1.4: Invariant yield as functions of transverse mass for  $\pi^\pm$ ,  $K^\pm$ ,  $p$ , and  $\bar{p}$  at mid-rapidity for pp (bottom) and Au–Au events from the most peripheral (second from bottom) to the central centrality classes (top).

a collective motion pattern superimposed on the chaotic thermal motion. It is defined as an azimuthally symmetric radial motion of the final state particles due to the collective velocity originating from the expansion of the fireball. At LHC energies a stronger radial flow is observed [10], and this can be explained by the presence of a higher energy density which leads to stronger pressure gradients.

### 1.4.2 Elliptic Flow

In the presence of strongly interacting matter, the spatial anisotropy in the initial shape of the fireball in non central collisions is converted into an azimuthal dependence of the momentum distribution of final state particles. In general, anisotropies in the particle distribution as a function of the azimuthal angle can be parameterized by a Fourier expansion usually written as [11]:

$$\frac{dN}{d(\varphi - \Psi_R)} = \frac{N_0}{2\pi} \left( 1 + 2 \sum_n v_n \cos[n(\varphi - \Psi_R)] \right) \quad (1.4)$$

where  $N_0$  is the mean number of selected particles per event and  $\varphi$  the azimuthal angle of the detected particles.

The Fourier coefficients are in general  $p_T$  and rapidity ( $y$ ) dependent and are given by:

$$v_n(p_T, y) = \langle \langle \cos[n(\varphi - \Psi_R)] \rangle \rangle \quad (1.5)$$

where the  $\langle \langle \dots \rangle \rangle$  denotes an average over events and particles. The first coefficients of the series,  $v_1$  and  $v_2$ , are called directed flow and elliptic flow, respectively. Non-zero directed flow implies a preferred direction for particle emission, either parallel ( $v_1 > 0$ ) or anti-parallel ( $v_1 < 0$ ) to the impact parameter. The elliptic flow separates two other directions, *in-plane* flow, when  $v_2 > 0$  indicates a preferred direction for particle emission around  $\Delta\varphi = 0$  and  $\Delta\varphi = \pi$ , and for *out-of-plane* flow, when  $v_2 < 0$ , the preferred direction is around  $\Delta\varphi = \pi/2$  and  $\Delta\varphi = 3\pi/2$ . Some of the experimental methods used to measure  $v_2$  are reported in detail in chapter 3.

The elliptic flow is a very powerful observable because it is sensitive to several properties of the matter depending on the particle under investigation and on its transverse momentum. In this thesis the elliptic flow of various particle species created in different collision stages, that are assumed to interact differently with medium, have been measured.

The  $v_2$  coefficient of low  $p_T$  hadrons, mainly coming from the hadronization of soft partons within the bulk, carries information on the hydrodynamic properties of the partonic medium created in heavy ion collisions. Among the different hadron species, the  $\phi$ -meson is of great interest because it is predicted to have a small hadronic cross section [12], and is therefore less affected by the interactions between hadrons during the hadronic phase of the collision. The  $v_2$  of the  $\phi$ -meson, reported in chapter 5, has been measured and compared with the  $v_2$  values of other hadron species. Furthermore, the  $v_2$  coefficient allows to study the interaction strength of hard and electromagnetic probes with the expanding medium. Hard probes are produced almost exclusively via hard partonic scattering processes in the earliest stage of the collision, therefore they are expected to experience the full collision history while propagating through the QCD medium. On the

## 1.5 Soft Probes

---

other hand, the electromagnetic probes are produced over the whole time evolution of heavy-ion collisions, but since photons do not strongly interact with the medium constituents, they are not affected by the presence of the medium. In chapter 6 and 7 it is described how  $v_2$  measurements help to study the different energy loss mechanism in the QGP of the heavy quarks and also to constrain the production time of direct photons respectively.

In the next three sections of this chapter the elliptic flow of soft, hard and electromagnetic probes are described together with theoretical models that aim to predict those measurements.

## 1.5 Soft Probes

Elliptic flow measurements of particles created within the bulk can constrain properties, such as the ratio of shear viscosity to entropy density ( $\eta/s$ ), of the system created in heavy-ion collision. For relativistic fluids the shear viscosity over entropy ratio  $\eta/s$ , which is predicted to be equal to  $1/4\pi$  (natural units) in case of an almost perfect liquid [13], is one of the most relevant variables. The elliptic flow is specifically studied in order to test hydrodynamical models which aim at describing the evolution of the medium created in the collision as the evolution of a fluid. At RHIC energies the comparison of  $v_2(p_T)$  measurements to hydrodynamic calculations in the low transverse momentum region provided evidence for strongly interacting matter which appears to behave almost like a perfect liquid [14, 15]. A measurement of elliptic flow at the LHC is therefore crucial to test the validity of a hydrodynamic description of the medium and to measure its thermodynamic properties in a new energy domain.

Elliptic flow measurements for charged particles at the LHC [16–18] at  $\sqrt{s_{NN}} = 2.76$  TeV are reported in the left panel of Fig. 1.5 for the 20-30% centrality interval. In comparison to the elliptic flow measurements in Au–Au collisions at  $\sqrt{s_{NN}} = 200$  GeV, an increase is observed of about 30% in the magnitude of  $v_2$  at the LHC energy.

The evolution of the  $v_2$  coefficient moving from RHIC to LHC energies is further investigated comparing elliptic flow measurements as a function

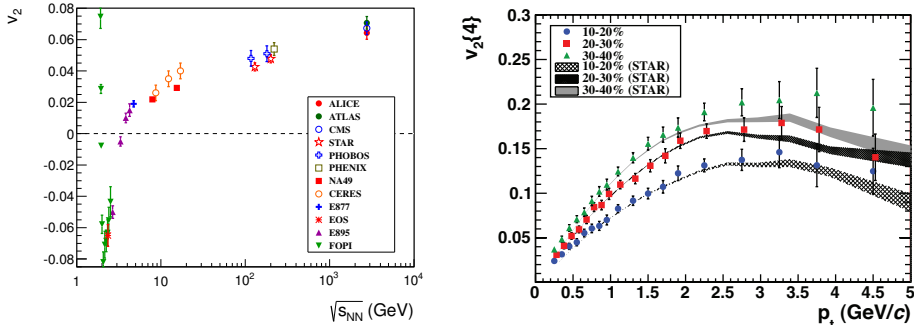


Figure 1.5: Left panel: Integrated elliptic flow as a function of the centre of mass energy of the collision for the 20-30% centrality interval. Right panel: comparison of  $v_2\{4\}(p_T)$  for various centralities measured by the ALICE (markers) and the STAR (dashed areas) experiments, figure taken from [16].

of transverse momentum. The right panel of Fig. 1.5 shows the charged particle  $p_T$ -differential  $v_2\{4\}$  measured by ALICE in three different centrality intervals [16]. STAR measurements are reported for comparison (dashed areas) in the same centrality classes. Despite the difference observed before at the integrated  $v_2$  level, the  $p_T$ -differential measurements are in remarkable agreement within uncertainties in the low transverse momentum region. The observed 30% increase in the integrated flow is therefore understood to be caused by an increase of the average transverse momentum. In the hydrodynamical picture this effect is explained by an increase of the radial flow. Finally, a comparison among the elliptic flow measurements of identified hadron species further constrains the hydrodynamical model and will help to understand the effect of the radial flow in elliptic flow measurements. The interplay of radial and elliptic flow is expected to lead to a dependence of the  $p_T$ -differential flow on the mass of the particle species. A clear mass ordering is observed at the RHIC energy [19] when comparing  $v_2$  among different particle species, as shown in the left panel of Fig. 1.6. Hydrody-

## 1.5 Soft Probes

dynamic calculations [20] are also reported and it is observed that in the hydro picture the mass ordering is naturally generated, where flow decreases with increasing particle mass. The stronger push to higher  $p_T$  values for heavier particles is introduced by the mass dependence of the radial flow, which is the reason that at a fixed value of  $p_T$  heavier particles have a smaller  $v_2$ .

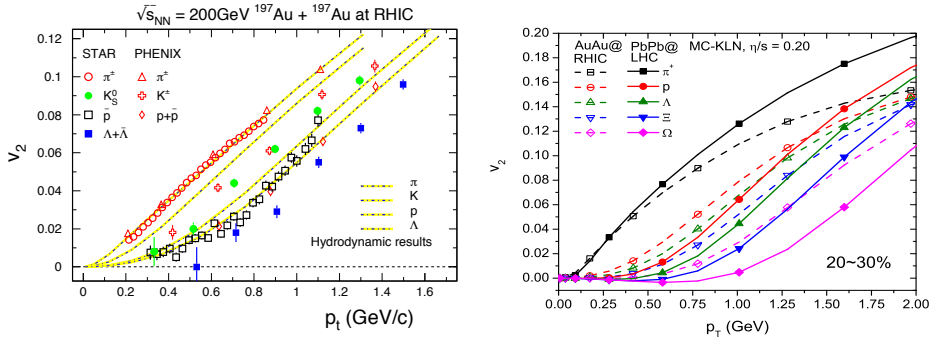


Figure 1.6: Left panel: Elliptic flow for different particle species measured by STAR and PHENIX compared to hydrodynamic model predictions. Right panel:  $p_T$ -differential  $v_2$  for identified hadrons for the 20-30% centrality using a pure hydrodynamic calculation for  $\sqrt{s_{NN}} = 200$  GeV (dashed lines) and 2.76 TeV (solid line).

The expectation of an increase of the radial flow, when moving to LHC energies, argued from the observed charged particle  $v_2$  measurements at the LHC, is once more naturally reproduced by pure hydrodynamic calculation shown in the right panel of Fig. 1.6, where the predictions at both RHIC and LHC energies are reported together for the 20-30% centrality class [21]. This comparison shows how the  $v_2$  of lighter particles increases while for heavier particle species it decreases from RHIC to LHC, leading to the similar observed charged particle  $v_2$  at the two energies. The extrapolation from RHIC to LHC is based on the assumption that the QGP's shear viscosity over entropy ratio  $\eta/s$  does not change much, staying close to the value  $\eta/s = 0.2$ . In the model the initial geometry (eccentricity of the system

and its event-by-event fluctuations) is calculated by using the KLN Monte Carlo [22], in which the density profiles of the colliding nuclei are obtained from a parameterization of the Colour Glass Condensate (CGC) [23], a theoretical model of gluon saturation. Also the initial geometry according to a Monte Carlo implementation of the Glauber model (MC-Glauber) has been tested [24]. It has been observed [21] that with MC-Glauber initial conditions a lower viscosity ( $\eta/s = 0.08$ ) has to be used in the model because of the smaller eccentricity from the MC-Glauber with respect to the MC-KLN model. The shear viscosity degrades the ability of the fluid to convert the pressure anisotropies in flow anisotropies.

It is seen that pure hydrodynamic calculation only roughly describe the  $v_2$  measurements at RHIC, especially for heavier particles, like  $p$  and  $\Lambda$ , in which case the elliptic flow is clearly over predicted.

**VISH2+1 and VISHNU at the LHC** The VISH2+1 model [25], just introduced for the comparison with the RHIC data and for the prediction for the LHC, is a model based on pure  $(2 + 1)$ -dimensional viscous relativistic hydrodynamics, which uses a chemical freeze-out at  $T_{chem} = 165$  MeV and a decoupling temperature (kinetic freeze-out)  $T_{dec} = 120$  MeV. The initial geometry in the simulation is from MC-KLN because of the more sophisticated fluctuations of the initial condition implemented in the model with respect to the MC-Glauber approach. The interactions among particles during the full evolution of the system are described in a pure hydrodynamical picture. The difference between the data and the model for the proton elliptic flow at RHIC can be due to the incorrect description, in this pure viscous hydrodynamic model, of the late hadronic collision stage, in which interaction among hadrons may further develop the radial flow. The increase of the radial flow component would be observed in the  $v_2$  measurements as a wider mass difference among the hadrons. To isolate the  $\eta/s$  of the partonic QGP matter indeed it requires knowledge of the relative contributions from both the partonic and hadronic phase. An improved viscous hydrodynamic calculation VISHNU [26], coupled with an hadronic cascade model UrQMD [27], takes into account the interactions among particles during

## 1.5 Soft Probes

the hadronic phase differently, reducing the discrepancy observed for the heavier particles  $v_2$ . The switching temperature between the two phases is fixed at  $T_{sw} = 165$  MeV. The hadron cascade model UrQMD propagates particles until kinetic freeze-out, where all the interactions cease.

In Fig. 1.7 the viscous hydrodynamical models (prediction for the LHC energy) calculated with and without a contribution of the hadronic cascade afterburner are compared. In the top panels the VISH2+1 calculation is shown for the 10-20% and 40-50% centrality intervals, while in the two lower panels the VISHNU model calculation is shown for the same centrality classes.

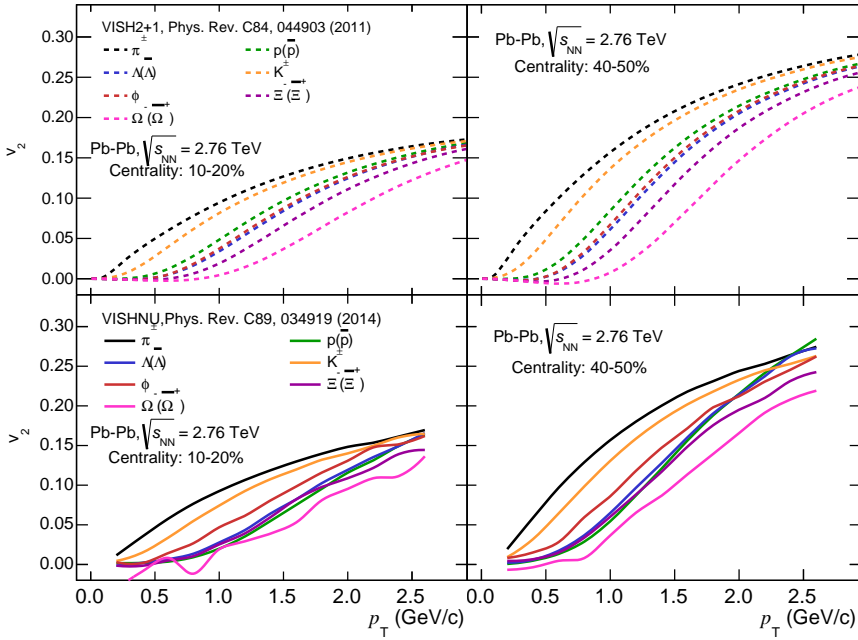


Figure 1.7: Top panels: VISH2+1 prediction in the 10-20% and 40-50% centrality intervals for several hadron species. Bottom panels: VISHNU prediction in the same centrality intervals and hadron species.

The increased mass splitting between pions and protons for VISHNU, with respect to the pure hydro model, illustrates the larger radial flow in the hybrid calculation due to the contribution of the hadronic cascade. In the model the splitting becomes less for strange and multi-strange particles. This is understood because in the hadronic cascade model a small hadronic cross section is assigned to strange hadrons. In the UrQMD model the magnitude of the hadronic re-interaction is related to the number of strange quarks contained in the hadron. Hence the amount of radial flow that the hadrons pick up in the hadronic phase depends on their strange quark content. This also explains why the strongest variation is observed for the protons because they do not contain strange quarks, resulting in a stronger coupling to the medium. On the other hand the prediction for the  $\phi$ -meson (containing an  $s$  and  $\bar{s}$  quarks) do not drastically change. Due to its small hadronic cross section in UrQMD the  $\phi$ -meson is rather weakly coupled to the hadronic medium and it decouples from the system almost immediately after hadronization. As a consequence of the hadronic re-interactions implemented in VISHNU, the clear and well-defined mass ordering observed in the VISH2+1 model is not preserved anymore. In chapter 5 detailed comparisons of identified particle elliptic flow measurements at the LHC energy, including rarer particles which have small hadronic cross sections like the  $\phi$ -meson, are reported and compared with the models.

### 1.6 Hard Probes

Hard probes are the particles originating from parton collisions with high momentum transfer. Such processes mostly occur at the initial stage of the collision between partons of incoming nuclei. These partons travel through the QGP and are penetrating probes of the matter. Due to their large mass, heavy quarks (charm and beauty) are also mostly produced in hard partonic scattering processes with large momentum transfer ( $Q^2 \geq 4m_{c,b}^2$ ). While traversing the hot and dense matter, the initially produced hard partons lose energy, mainly due to multiple scatterings (elastic collisions) and medium-induced gluon radiation (inelastic processes). In addition to the mechanisms

## 1.6 Hard Probes

---

of energy loss also hadronization can influence the  $v_2$  measurements.

- **Radiative energy loss:** the emission of gluons by high- $p_T$  partons due to QCD interactions with the medium constituents, are expected to lead to a substantial energy loss. In the BDMPS model [28] this phenomena depends on the properties of the medium, such as the in-medium path length of the parton, the mean free path, the transport coefficient, defined as the squared transverse momentum transferred to the emitted gluon over the mean free path of the traversing particle [29], and the colour factor, which is equal to  $4/3$  for quark-gluon coupling and which is  $3$  for gluon-gluon coupling<sup>2</sup>. The difference among gluons and quarks is due to their different colour factors and it leads to a larger suppression of particles coming from gluon fragmentation with respect to those originating from quarks. A large fraction of the light-flavoured hadrons are produced in the late stages of the collision evolution from the fragmentation of gluons, while charmed and bottom mesons mainly originate from the fragmentation of heavy quarks directly produced in the early stages of the collision. Consequently, this effect should be seen as a bigger suppression for light mesons with respect to the charmed and beauty ones. The quark mass is believed to further discriminate in the radiative energy loss process. Due to the so-called dead-cone effect [30], which predicts a suppression of the gluon radiation at forward angles  $\vartheta$  smaller than  $\vartheta_0 = m/E$ : and since  $\vartheta_0$  is larger for heavy quarks than for light quarks, the cone where gluon radiation is forbidden is larger for heavy quarks.
- **Collisional energy loss:** partons also lose energy via elastic collisions with the constituents of the hot and dense plasma. This mechanism was expected to play a non-negligible role for heavy quarks at the LHC mainly in the low transverse momentum region. Recent studies [31] showed that, radiative and collisional energy losses for heavy

---

<sup>2</sup>The colour factor are calculated through the Casimir operators of the gauge group  $SU(N_C)$

quarks are comparable, and therefore collisional energy loss cannot be neglected.

- **Hadronization:** it is usually considered that a parton, which traversed the medium, hadronizes in the vacuum. However, if the parton density is large it could happen that partons undergo hadronization via coalescence inside the medium [32, 33]. In this scenario a heavy quark picks up other quarks from the medium. Also the elliptic flow can be affected by the relative contribution of different hadronization mechanisms. For fragmentation, charmed hadron elliptic flow is essentially identical to the charm quark  $v_2$ . On the other hand, if hadronization happens via coalescence, the hadron elliptic flow is approximately the sum of the constituent quark flows [32].

The  $v_2$  coefficient of charmed and beauty mesons (and of their semi-leptonic decay products) can be used to investigate the interaction strength of heavy quarks with the expanding medium. At low transverse momenta, it is sensitive to the degree of thermalization of heavy quarks in the deconfined medium, while at high  $p_T$  it carries information on the fragmentation and on the energy loss mechanisms of high energy partons in the medium. The lost energy of a high  $p_T$  parton strongly depends on the path length traversed in the medium by the parton itself. The path length, because of the spatial anisotropy of the created system, depends on the azimuthal emission angle of the parton, hence a parton that will travel in the out-of-plane direction will travel through less matter losing less energy with respect to parton traveling in the in-plane direction. This difference in the traversed matter is reflected in an azimuthal distribution of the emitted particles with respect to the reaction plane [34, 35].

The ALICE collaboration has measured the elliptic flow  $v_2$  of open heavy-flavour hadrons at mid-rapidity ( $|y| < 0.5$ ) via their hadronic decays in Pb–Pb collisions at  $\sqrt{s_{NN}} = 2.76$  TeV. The measured averaged  $v_2$  of prompt  $D^0$ ,  $D^+$  and  $D^{*+}$ , shown in left panel of Fig. 1.8, indicates a positive  $v_2$  in semi-central (30-50%) Pb–Pb collisions with a significance of about  $5.7\sigma$  for  $2 < p_T < 6$  GeV/ $c$  [36]. The anisotropy of prompt  $D^0$

## 1.6 Hard Probes

mesons was measured in the three centrality classes 0-10%, 10-30% and 30-50% [37]. The results show a hint of increasing  $v_2$  from central to semi-peripheral collisions and are comparable in magnitude to that of inclusive charged particles, suggesting that charm quarks participate in the collective flow of the expanding medium.

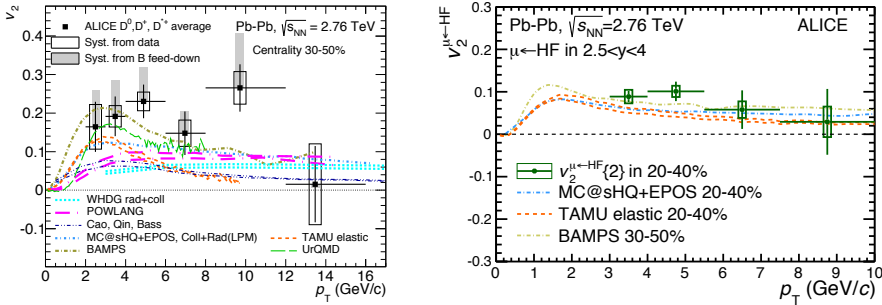


Figure 1.8: Left Panel: Average D meson  $v_2$  as a function of  $p_T$  in the 30-50% centrality class. Right panel:  $p_T$ -differential elliptic flow of muons from heavy-flavour decays in  $2.5 < y < 4$  for the centrality class 20-40%. Both the measurements are compared to various transport model predictions.

The elliptic flow of muons from heavy-flavour hadron decays at forward rapidity ( $2.5 < y < 4$ ) was also measured with the ALICE detector at the LHC in Pb-Pb collisions at  $\sqrt{s_{NN}} = 2.76$  TeV in the three centrality classes 0-10%, 10-20% and 20-40% [38]. The  $p_T$ -differential  $v_2$  is reported in the right panel of Fig. 1.8 in the interval  $3 < p_T < 10$  GeV/c for the 20-40% centrality class. A positive  $v_2$  is observed in the range  $3 < p_T < 5.5$  GeV/c for semi-central collisions with a significance larger than  $3\sigma$  when combining statistical and systematic uncertainties.

Heavy-flavour hadrons can be also studied by measuring electrons produced via semi-leptonic decay channels. STAR and PHENIX have measured the elliptic flow coefficient of electrons from heavy-flavour hadron decays [39, 40] in the 0-60% centrality class, finding positive values of  $v_2$  at the top RHIC energy. The results, at both RHIC and LHC energy, reported

in Fig. 1.9 are compared to model calculations describing the interactions of heavy quarks and open heavy-flavour hadrons with the high-density medium formed in high-energy heavy-ion collisions.

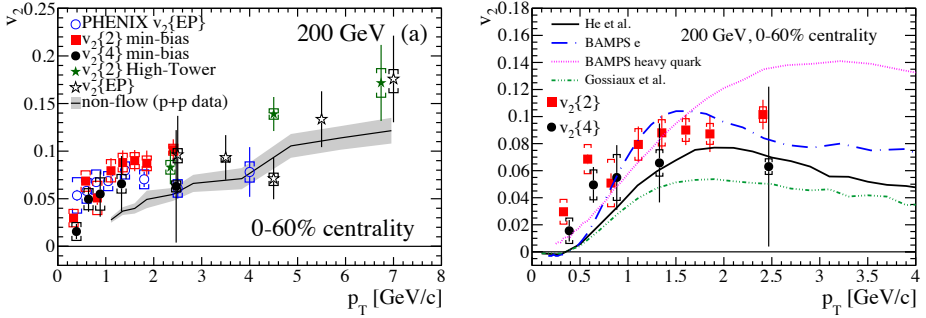


Figure 1.9: Left panel:  $v_2$  coefficient for heavy-flavour decay electron measured by STAR and PHENIX at  $\sqrt{s_{NN}} = 200$  GeV. Right panel: heavy-flavour decay electron azimuthal anisotropy compared to model calculations.

The anisotropy is qualitatively described by the models that include both heavy quark energy loss in a geometrically anisotropic medium and mechanisms that transfer to charm quarks the elliptic flow induced during the system expansion. The same agreement among models and data is independently observed when looking at the fully reconstructed D-meson or at their semi-leptonic decay products. Models that do not include a collective expansion of the medium or lack a contribution to the hadronization of charm quarks from recombination with light quarks from the medium predict in general a smaller anisotropy than observed in the data.

A complementary elliptic flow measurement of the heavy-flavour decay electrons at central rapidity with the ALICE detector at the LHC, reported in chapter 6, is of great interest by itself and it provides new and additional constraints on theoretical calculations which aim at describing heavy quark production and its interactions with the medium. In the following the models aiming to describe the measured anisotropy of the heavy-flavour are briefly described. The reported models will later be used for the comparison

## 1.6 Hard Probes

---

with the heavy-flavour decay electron  $v_2$  in this thesis.

**BAMPS** [41, 42]. This partonic transport model is based on the Boltzmann approach to multi-parton scattering. Heavy quarks interact with the medium via collisional processes computed with a running strong coupling. Hadronization is performed using vacuum fragmentation functions. In [41] the lack of radiative processes is accounted for by scaling the binary cross section with a correction factor ( $K = 3.5$ ), which is tuned to describe the heavy-flavour decay electron measurements at RHIC. More recent BAMPS calculation [42] including both collisional and radiative processes for light and heavy quarks in a static thermal medium are also available.

**TAMU elastic** [43]. This is a heavy-flavour transport model based on the Langevin equation which includes collisional elastic processes only. The heavy-quark transport coefficient is calculated within a non-perturbative approach, where the interactions proceed via resonance formation that transfers momentum from the heavy quarks to the medium constituents. The model includes the hydrodynamic medium evolution and a component of recombination of heavy quarks with light-flavour quarks from the QGP.

**MC@HQ+EPOS, Coll+Rad(LPM)** [44]. This pQCD model includes collisional and radiative (with a Landau-Pomeranchuk-Migdal correction [45]) energy loss mechanisms for heavy quarks with a running strong coupling. The medium fluid dynamical expansion is based on the EPOS model [46]. A component of recombination of heavy quarks with light-flavour quarks from the QGP is also incorporated in the model.

**POWLANG** [47]. This transport model is based on collisional processes treated within the framework of Langevin dynamics, within an expanding deconfined medium described by relativistic viscous hydrodynamics. Hadronization is implemented in the model via vacuum fragmentation.

## 1.7 Electromagnetic Probes

Photons are produced in all the stages of heavy-ion collisions in processes involving different momentum transfer  $Q^2$ . Since photons do not interact with the medium once they are created, they carry undistorted information about the system from the time of their production.

1. In the first stage of the collision, 'prompt' photons originate mainly from hard parton-parton scatterings. For large enough values of the photon transverse momentum  $p_T$ , this process can be calculated using perturbative QCD [48]. The photon production decreases as an inverse power of  $p_T$  and increases with the center-of-mass energy and they are expected to be produced isotropically.
2. During the quark-gluon plasma phase, 'thermal' photons are emitted from quarks that undergo collisions with other quarks and gluons in the medium. These photons have an exponentially suppressed spectrum, extending up to several GeV. The shape of this spectrum is determined by the plasma temperature. Therefore, these photons could serve as a thermometer of the QGP.
3. Then the system expands and cools down. At hadronization, 'hadron-gas' photons are produced either in the scatterings of  $\pi, \rho, \omega$  and others, or from resonance decays. This mechanism survives until the resonances cease to interact. The energy of these photons ranges from a few hundred MeV to several GeV. The usual considered contributions in models to the production rate of the photons from this stage are  $\pi\pi(\rho) \rightarrow \gamma\rho(\pi)$  as well as the meson - meson(baryon) bremsstrahlung radiation  $m + m(B) \rightarrow m + m(B) + \gamma$ .
4. Finally, after freeze-out, additional photons can be produced by  $\pi^0 \rightarrow \gamma\gamma$  and  $\eta \rightarrow \gamma\gamma$  decays and higher resonances. Their energy lies in the range of up to a few GeV.

Direct (thermal and hadron-gas) photons produced in phase 2 and 3 give information on the extent of thermalization of the created system.

## 1.7 Electromagnetic Probes

---

Experimentally they have to be extracted from the huge background of photons produced by the decays of  $\pi^0$ ,  $\eta$  and from the prompt photons.

Since the azimuthal anisotropy of direct photons strongly depends on their production mechanism, a measurements of  $v_2^{\gamma,dir}$  allows to put further constraints on their production time.

Prompt photons from the initial hard scatterings processes are expected to be produced isotropically, if they do not interact with the medium the  $v_2^{\gamma,pQCD} = 0$ . On the other hand, thermal photon production is affected by the hydrodynamic flow, so that photons emitted along  $\Psi_R$  get a stronger boost. This results in a positive  $v_2$  for thermal photon, while the magnitude depends on the properties of the system at the photon production time.

Consequently, the thermal radiation emitted from the QGP phase is expected to have a small and positive  $v_2$ , while photons from the hadron-gas are produced in a later stage, where the elliptic flow is fully developed, with a  $v_2$  similar to hadrons. The strength of the  $v_2$  signal depends then on the different fraction of photons coming from the different stages, for instance prompt photons can washout half of the  $v_2$  signal coming from the thermal component.

Recently the ALICE experiment measured the direct photon  $p_T$  spectra in the 0-40% centrality interval at  $\sqrt{s_{NN}} = 2.76$  TeV [49]. The measurement is reported in Fig. 1.10 where the direct photon spectrum shows at low  $p_T$  a significant excess above the pQCD predictions which is described also in this case by an exponential function with an inverse slope parameter of  $T_{eff} = (304 \pm 51^{\text{stat}+\text{syst}})$  MeV. At higher  $p_T$  the signal is well described by binary scaled NLO (pQCD) calculations for pp.

PHENIX presented new preliminary results [50] of direct photon spectra measurements in Au–Au collisions at  $\sqrt{s_{NN}} = 200$  GeV as a function of the transverse momentum. This measurements, reported in Fig. 1.11, allows for an estimate of the QGP initial temperature which is about  $T_{eff} = 240$  MeV in the most central collisions, and no significant centrality dependence was observed. The temperature is extracted with an exponential fit of the low  $p_T$  part of the spectra, while the higher  $p_T$  region is found to be in agreement with pQCD calculation scaled by the number of binary collision.

In addition to the direct photon yield in several centrality classes, the

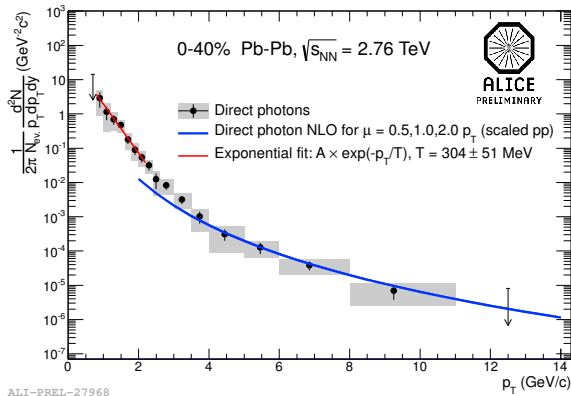


Figure 1.10: Direct photon  $p_T$  spectra in Pb-Pb collisions at  $\sqrt{s_{NN}} = 2.76$  TeV for 0-40% centrality class with NLO pQCD predictions (blue line) and low  $p_T$  exponential fit (red line).

PHENIX collaboration measured the direct photon azimuthal anisotropy [51]. In Fig. 1.12 the elliptic and triangular flow are reported as a function of the transverse momentum in three centrality classes. At high transverse momentum the measured  $v_2$  is consistent with zero within uncertainties, which is expected from the dominance of the prompt photons. At lower momenta the measured azimuthal anisotropy shows an unexpected large photon elliptic flow, comparable in magnitude to that of hadrons. Since the anisotropic flow builds up in time, the thermal photon anisotropy is expected to be smaller than the radiation emitted in the hadronic phase of the collision. A large direct photon  $v_2$  can indicate a large contribution to the direct photon yield from the late stage of the collision evolution.

Nowadays several models are aiming to describe the strong excess over the known pQCD sources that have been attributed to thermal radiation and its relative azimuthal anisotropy.

Hydrodynamic calculations [52, 53], using the dynamic evolution of the radiating system modelled with the VISH2+1 model and including event-by-event density fluctuations, are studied also for the photon case. Momentum

## 1.7 Electromagnetic Probes

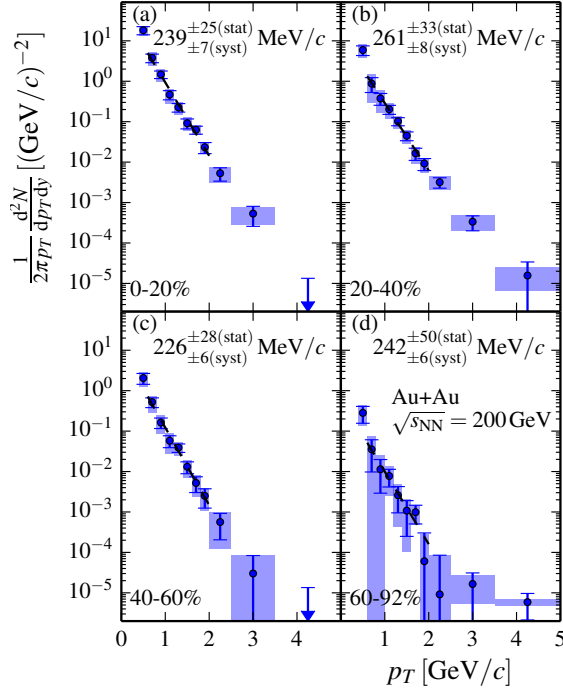


Figure 1.11: Direct photon  $p_T$  spectra in different centrality classes as measured by PHENIX in Au–Au collisions at  $\sqrt{s_{NN}} = 200$  GeV. Dashed lines are the exponential fits at low transverse momentum.

spectra and anisotropic flow are computed, both with and without accounting for the viscous correction to the standard thermal emission rate. The hadronic phase is modelled as an interacting meson gas, where the chemical freeze-out temperature is fixed again at  $T_{chem} = 165$  MeV. In the model only the prompt and the thermal component radiated by the plasma are included, while the hadronic emission processes, which involve meson and baryon interactions, as well as the bremsstrahlung processes are neglected. It is found that in order to describe the recently measured total thermal

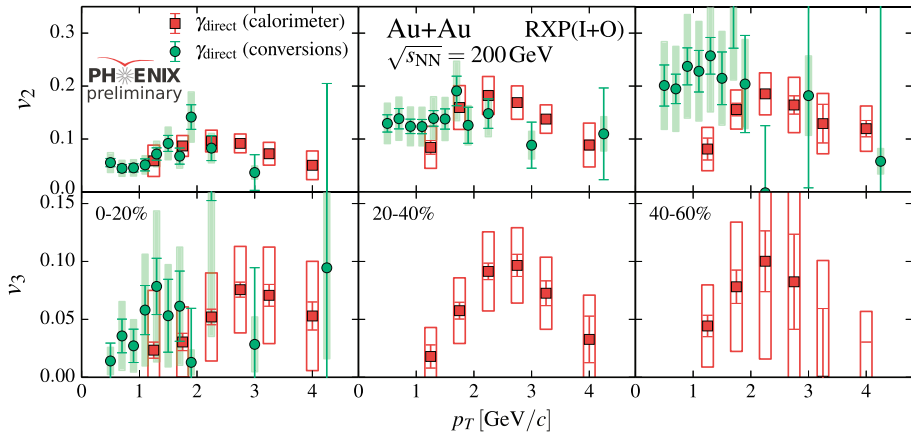


Figure 1.12: Direct photon  $v_2$  and  $v_3$  as a function of  $p_T$  in three centrality bins as measured by the PHENIX in Au–Au collisions at  $\sqrt{s_{NN}} = 200$  GeV.

photon yield, an additional contribution of photons from late emission has to be incorporated in the model. The large observed effective temperature of thermal photons emitted from the collision is then interpreted to be generated mostly from the strong radial flow in these collisions.

In Fig. 1.13 the  $v_n$  coefficients are reported for central and semi-central Au–Au and Pb–Pb collisions at RHIC and LHC respectively for two different assumption for the initial condition, the MC-KLN and MC-Glauber, including viscous contributions to the evolution of the hydrodynamic flow in the medium. The difference between the solid and dashed line represents the effect of including viscous corrections to the photon emission rate. It has been observed that viscous corrections to the emission rate have a larger effect on the  $v_n$  coefficients than the viscous suppression due to hydrodynamic flow in the medium.

The direct photon flow is calculated using the weighted sum of the different sources. An increase of the thermal photon  $v_n$  at the LHC is predicted due the longer lifetime of the QGP, which allows to develop larger flow

## 1.7 Electromagnetic Probes

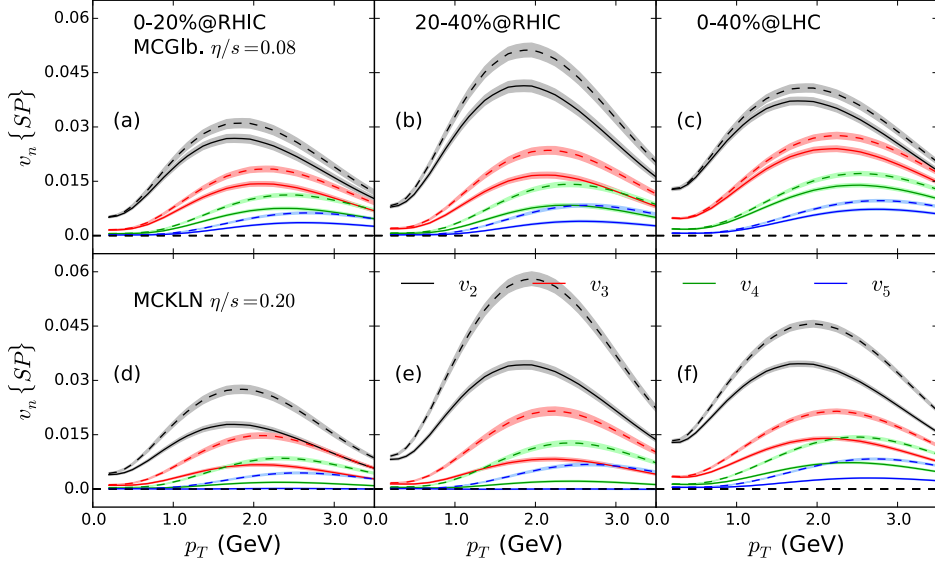


Figure 1.13: Direct photon  $v_n$  from hydrodynamic model including initial state fluctuation and shear viscosity corrections for different initial conditions. Figure taken from [52]

anisotropies. The hydrodynamic predictions are systematically lower than the measured  $v_2$  and  $v_3$  coefficient by the PHENIX experiment, indicating also for this observables the possible lack of photon emission during the hadronic phase of the collision, when the anisotropic flow is fully developed. Other theoretical models [54, 55] including slightly different assumption on the photon production rate and on the hydrodynamic evolution of the system also predict a smaller  $v_2$  for the direct photon with respect to the one measured at RHIC.

Collisions among hadrons as well as meson-meson and meson-baryon bremsstrahlung are included in the Parton-Hadron-String Dynamics (PHSD) transport approach [56, 57]. Within this approach, the partonic channels are found to contribute up to 50% of the direct photon spectrum at pho-

ton momenta  $p_T > 1 \text{ GeV}/c$ , while the low transverse momentum region ( $p_T < 1 \text{ GeV}/c$ ) is dominated by photon bremsstrahlung in meson+meson and meson+baryon collisions. The model reproduces the transverse momentum spectrum and remarkably also the effective temperature measured at the top RHIC energy [57]. This observation indicates that the high slope parameter mainly reflect the boost of the photon spectra due to the collective flow of hadrons. In PHSD the  $v_2$  coefficient is calculated, as well as for the hydro models, using the weighted sum of the different channels. The results obtained with this model give slightly higher  $v_2$  values than pure hydrodynamic calculations, an effect that is attributed to the additional hadronic channels included. The large uncertainty band is coming from the modelling of the cross section for the individual channels. The prediction at the RHIC energy is compared in the left panel of Fig. 1.14 with the PHENIX measurements [58, 59] in Au–Au collisions in the 0-40% centrality class, and a rough agreement is observed within the large systematic uncertainties of both the measurement and the prediction.

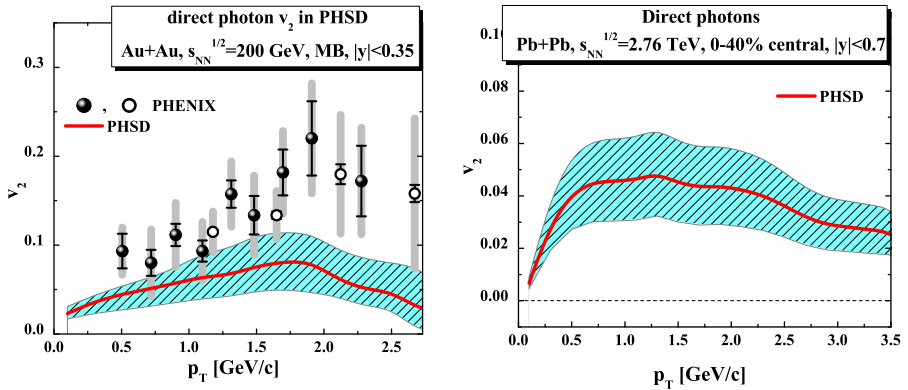


Figure 1.14: Elliptic flow  $v_2$  as a function of the transverse momentum for the direct photon calculated within the PHSD model, in the left panel the model is compared with PHENIX measurements [58, 59], while in the right panel the prediction for the LHC energy is shown.

## 1.7 Electromagnetic Probes

---

In the right panel of Fig. 1.14 the prediction for Pb–Pb collisions at the LHC is shown for the same centrality interval. These results might also indicate the importance of the photons produced in the hadronic phase of the heavy-ion collision.

In chapter 7 of this thesis the measurement of the direct photon elliptic flow measured in Pb–Pb collisions with the ALICE detector is reported and a comparison with theoretical predictions is shown.



---

---

## Chapter 2

# The ALICE experiment

---

---

The data analyzed in the presented work were collected with ALICE (A Large Ion Collider Experiment) [60–62], which is a detector setup built mainly to the study Pb–Pb collisions at the Large-Hadron-Collider (LHC). The main goal of the experiment is to study in detail the properties of Quantum Chromodynamics (QCD) at high densities and temperatures. In the first part of this chapter a general overview of the ALICE detector is given. In the second part the sub-detectors used for the measurements reported in this thesis are described in more detail.

### 2.1 Detector design

The ALICE detector consists of a central barrel embedded in a solenoidal magnet (devoted to the study of hadronic and electromagnetic signals) and a muon arm with a separate dipole magnet (devoted to study the behaviour of quarkonia in dense matter). The acceptance of the central detector system ranges from  $-0.9 < \eta < 0.9$  over the full azimuth and the

## 2. The ALICE experiment

---

muon arm covers  $-4 < \eta < -2.4$ .

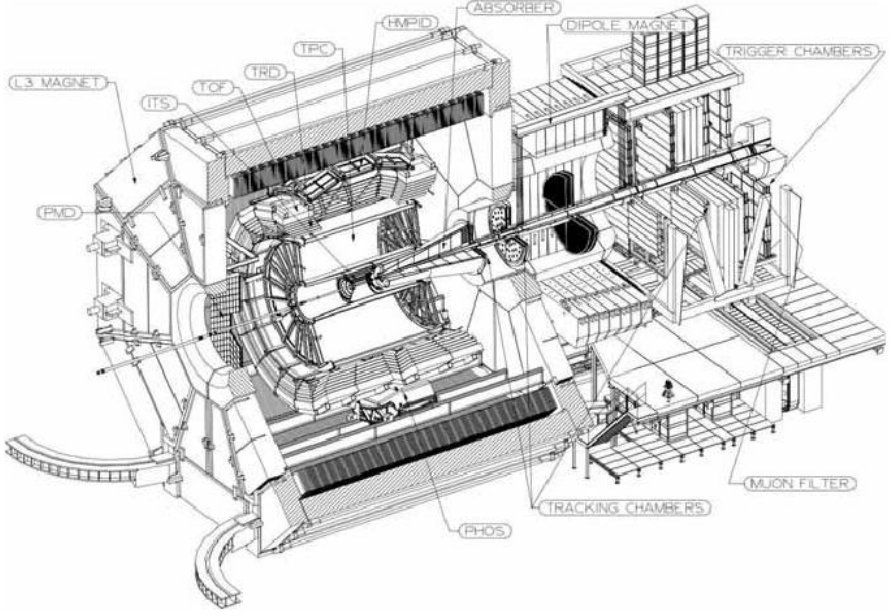


Figure 2.1: A sketch of the ALICE detector

ALICE has a cylindrical geometry with the symmetry axis coinciding with the nominal position of the LHC beam, as illustrated in Fig. 2.1. The global reference frame is as follows: the  $z$  axis is parallel to the beam and pointing to the opposite direction of the muon arm,  $x$  and  $y$  are in the transverse plane to the beam direction. The spacial coordinates of a particle are given in terms of their azimuthal angle  $\varphi$  and pseudo-rapidity  $\eta$ . The latter is defined in Equation: 2.1, as a function of the polar angle  $\theta$ , the angle with respect to the beam axis.

$$\eta = -\ln \left( \tan \frac{\theta}{2} \right) \quad (2.1)$$

## 2.1 Detector design

---

The beam pipe, that is made out of beryllium, an element with a low atomic number, to minimize multiple scattering in the material, has an outer radius of 3 cm and a thickness of 0.8 mm. The ALICE magnet (constructed for the L3 experiment at LEP) provides a magnetic field of 0.5 T, parallel to the beam axis. The field strength has been chosen to have both a good acceptance for low momentum tracks and a good momentum resolution for high- $p_T$ .

The ALICE central barrel includes many sub-detectors. Going outwards from the beam pipe, the central barrel detector systems are:

- Inner Tracking System (ITS) [63], a silicon detector system for tracking, vertexing and particle identification.
- Time-Projection-Chamber (TPC) [64], a cylindrical chamber filled with gas, which acts as the main ALICE tracking and particle identification detector.
- Transition-Radiation-Detector (TRD) [65], excellent for high energy electron identification exploiting transition radiation emission.
- Time-of-Flight (TOF) [66], dedicated to particle identification, capable of  $\pi/K$  separation up to 2.2 GeV/c and of K/p separation up to 4 GeV/c.
- High-Momentum-Particle-Identification (HMPID) [67], which is a Ring Imaging Cherenkov detector used for identification of  $\pi$ , K, p in the  $1 < p_T < 5$  GeV/c range.
- Two electromagnetic calorimeters, PHOS [68] and EMCal [69]; PHOS has an higher granularity than EMCal, but has a smaller acceptance.
- ACORDE, a scintillator array placed outside the magnet for cosmic ray measurements.

---

## 2. The ALICE experiment

---

In addition a number of small and specialized detector systems, that are used for triggering or to measure global event characteristics, are located at forward rapidity.

- The T0 detector [70] which is mounted around the beam pipe and which is the fast timing and trigger detector ( $< 25$  ps).
- The VZERO scintillator detectors [71] are used as a minimum bias trigger, for rejection of beam gas background and for the centrality class measurements in Pb–Pb collisions.
- The Forward-Multiplicity-Detector [72] (FMD) provides charged multiplicity information over a large fraction of the solid angle.
- The Photon-Multiplicity-Detector [73] (PMD) measures the multiplicity and spatial distribution of photons even-by-event in the region  $2.3 < \eta < 3.7$ .
- The Zero-Degree Calorimeters [74] (ZDC) provide information on the centrality of the collision as well as on the reaction plane by measuring the energy of the nucleons not involved in the collision (spectators).
- The muon spectrometer [75] is primarily designed to measure the production of heavy-quark resonances ( $J/\psi, \psi', \Upsilon, \Upsilon', \Upsilon''$ ) through their decay into  $\mu^+\mu^-$  pairs, with a mass resolution sufficient to separate all states.

In the next sections the detectors used for the measurements reported in this thesis, ITS, TOF, TPC ,EMCal and V0, are described in more detail.

### 2.2 Inner Tracking System

The Inner Tracking System [63] consists of six cylindrical layers of coordinate-sensitive detectors, covering the central rapidity region ( $|\eta| < 0.9$ ) for vertices located within the interaction diamond ( $\pm 1\sigma = 5.3$  cm ) along the

## 2.2 Inner Tracking System

---

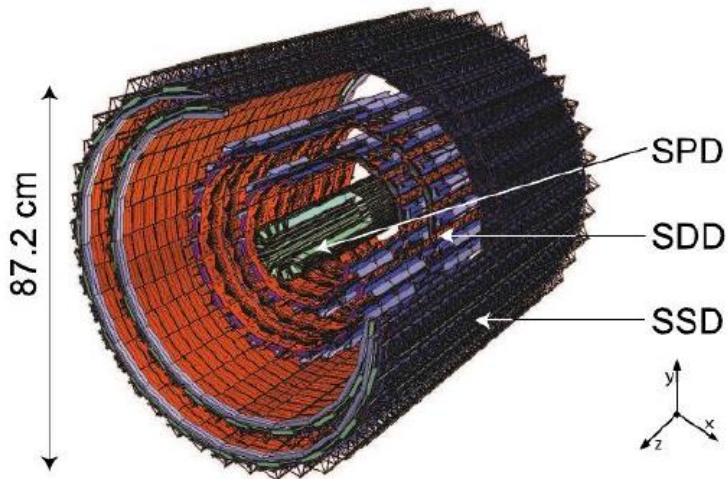


Figure 2.2: The ALICE Inner Tracking System. Figure taken from [63]

beam direction ( $z$ ), and it provides a full coverage in azimuthal angle. The layout of the ITS is shown in Fig. 2.2.

The basic functions of the ITS are:

- primary and secondary vertex reconstruction with the high resolution required for the detection of particles with open charm and open beauty.
- Measurement with a resolution better than  $100\ \mu\text{m}$  of the impact parameter of the tracks. The impact parameter is defined as the distance of closest approach of the track to the primary vertex.
- Improvement of the momentum resolution for high momentum particles.

## 2. The ALICE experiment

- Reconstruction and identification of low momentum tracks with  $p_T < 200$  MeV/c, which are bent too strongly by the magnetic field to be reconstructed by the TPC.
- Particle-identification with  $dE/dx$  measurements.

The first two layers are positioned at 3.9 and 7.6 cm from the interaction point. The high particle density in this region requires an excellent position resolution, which is achieved with a silicon pixel detector (*SPD*) with a cell size of  $50(r\varphi) \times 425(z)\mu m^2$ . At  $r = 15$  and 23.9 cm there are two layers of silicon drift detectors (*SDD*) and at  $r = 38.5$  and 43.6 cm two layers of silicon strip detectors (*SSD*). The SDD gives a good 2-dimensional space-point resolution together with excellent two-tracks separation capability and energy loss measurements. At larger distances from the interaction point (where the particle density can be lower than one track per  $cm^2$ ) the double-sided micro-strip detectors also allow for  $dE/dx$  measurements and deliver important information for the connection of tracks from the TPC and ITS. The main parameters for each of the three detector types are summarized in Table 2.1

Detector	r(cm)	$ \eta $	Resolution $\sigma_{r\varphi} \times \sigma_z (\mu m)^2$	main purposes
SPD	3.9	2.0	$12 \times 100$	tracking, vertexing
SPD	7.6	1.4		tracking, vertexing
SDD	15.0	0.9	$38 \times 28$	tracking, vertexing, $dE/dx$
SDD	23.9	0.9		tracking, vertexing, $dE/dx$
SSD	38.5	1.0	$20 \times 830$	tracking, vertexing, $dE/dx$
SSD	43.6	1.0		tracking, vertexing, $dE/dx$

Table 2.1: Summary of the ITS main characteristics

The performance of the  $dE/dx$  capabilities as a function of track momentum for the ITS is shown in Fig. 2.3 for Pb–Pb collisions. The estimated

## 2.2 Inner Tracking System

overall resolution of the ITS  $dE/dx$  measurement is about 11%, which allows for a good  $e/K$  separation up to 500 MeV/c and a  $e/p$  separation up to about  $\sim 1.5$  GeV/c. The lines are parameterizations of the detector response based on the Bethe-Bloch formula.<sup>1</sup>

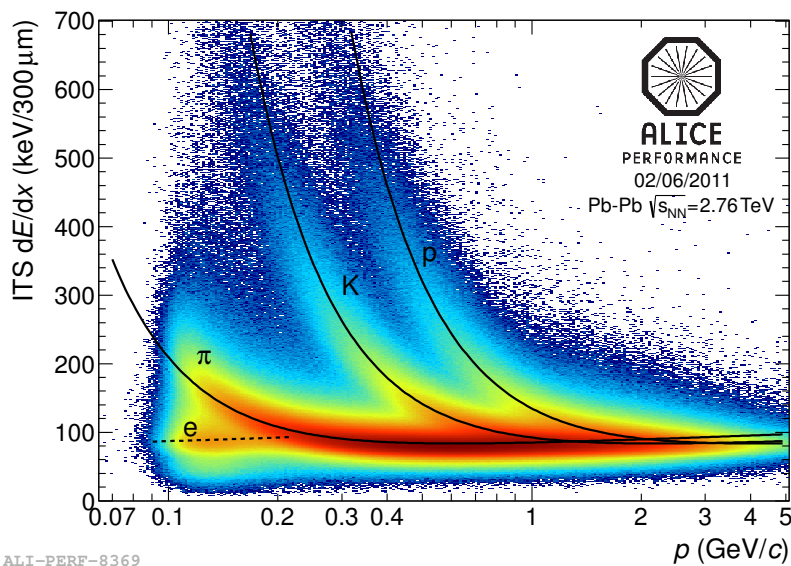


Figure 2.3:  $dE/dx$  of charged particles as a function their momentum, both measured by the ITS standalone, in Pb-Pb collisions at 2.76 TeV.

<sup>1</sup>The Bethe-Bloch formula can be parameterized as in Equation: 2.2 for a particle with speed  $\beta$ , charge  $z$ , and energy  $E$ , traveling a distance  $x$  into a target of electron number density  $n$  and mean excitation potential  $I$

$$-\frac{dE}{dx} = \frac{4\pi}{m_e c^2} \cdot \frac{n z^2}{\beta^2} \cdot \left( \frac{e^2}{4\pi\epsilon_0} \right)^2 \cdot \left[ \ln \left( \frac{2m_e c^2 \beta^2}{I \cdot (1 - \beta^2)} \right) - \beta^2 \right] \quad (2.2)$$

where  $c$  is the speed of light and  $\epsilon_0$  the vacuum permittivity,  $e$  and  $m_e$  the electron charge and rest mass respectively.

### 2.3 Time Projection Chamber

The Time-Projection Chamber [64] (Fig. 2.5) is the main tracking detector of the central barrel and is optimized to provide, together with the other central barrel detectors, charged-particle momentum measurements with good two-track separation, particle identification, and vertex determination. The global acceptance is  $-0.9 < \eta < 0.9$  for full radial tracks and full azimuthal coverage.

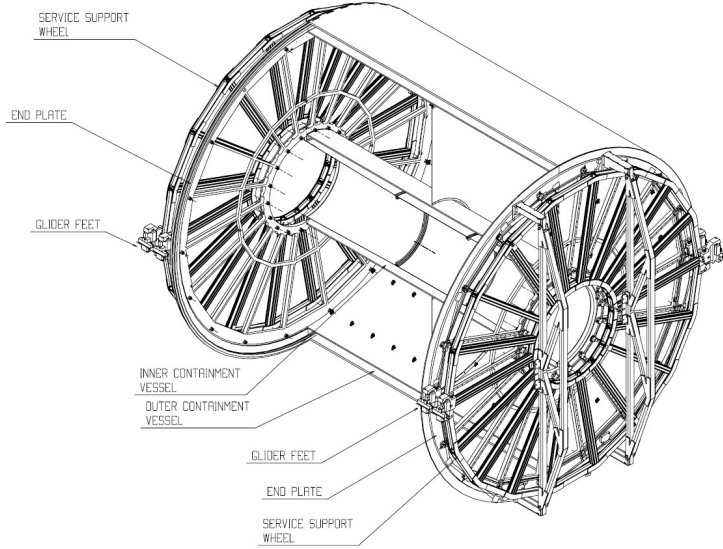


Figure 2.4: The ALICE Time-Projection-Chamber. Figure taken from [62]

The TPC is cylindrical in shape with an inner radius of 85 cm and an outer radius of 247 cm. The overall length of the TPC detector along the beam direction is 510 cm. The active volume of the detector is 88 m<sup>3</sup>, and it is filled with a gas mixture (90%-10%) of  $Ne/CO_2$ . This particular mixture was used in order to provide a large drift velocity of the charges (to keep the pile-up under control), a low diffusion coefficient and negligible Coulomb

## 2.3 Time Projection Chamber

multiple scattering (to increase the spatial resolution). The TPC is capable of three-dimensional reconstruction of charged particles with a high number of space points and with an excellent spatial resolution. The Multi-wire proportional chambers with segmented cathode pad read out are mounted into 18 trapezoidal sectors of each end-plate, and allow a bidimensional measurement, while the third coordinate is obtained by measuring the drift time. The resolution for the track momentum is as low as 1% for low momentum tracks ( $p_T \sim 1$  GeV/c), and degrades with increasing momenta (about 3.5% for  $p_T \sim 100$  GeV/c).

This detector also helps to reconstruct vertices and can provide particle identification in the low and intermediate  $p_T$  region via  $dE/dx$  measurement.

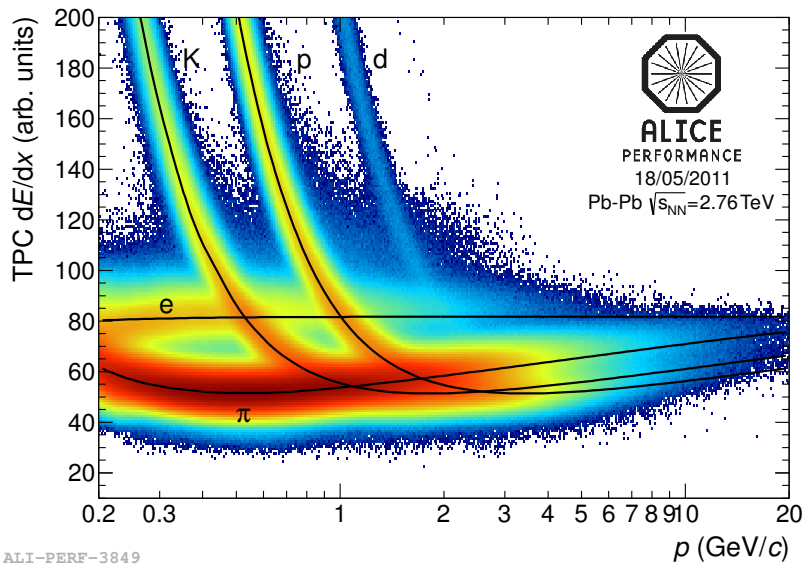


Figure 2.5:  $dE/dx$  of charged particles as a function their momentum, both measured by the TPC detector, in Pb–Pb collisions at 2.76 TeV.

The analog nature of the signal collected by the MWPC readout also

allows to measure the energy loss of the charged particles while traversing the gas ( $dE/dx$ ). The resolution on the  $dE/dx$  determination, for tracks crossing the entire detector, was measured to be about 5.5% [64]. This gives good particle identification capabilities from 200 MeV/ $c$  up to almost 1.5 GeV/ $c$  (e.g. p/K separation) as shown in Fig. 2.5, where the performance of the  $dE/dx$  capabilities as a function of the track momentum is shown. The parameterizations of the detector response based on the Bethe-Bloch formula are also plotted in the figure.

### 2.4 Time of Flight

The geometry of the TOF [66] detector is very similar to that of the detectors discussed previously. Its elementary unity is a MRPC (Multi-gap Resistive-Plate Chamber) strip, which is subdivided in 96 readout pads and installed inside the gas volume, forming a module. A group of 5 modules composes a super-module covering the whole detector in pseudo-rapidity ( $|\eta| < 0.9$ ) and full azimuth. This arrangement is illustrated in Fig. 2.6. This detector is a cylindrical detector with an internal radius of 370 cm and an external one of 390 cm and an overall longitudinal length of 7.45 m.

The main task of the TOF (Fig. 2.7) detector is particle identification of charged tracks via the measurement of their time of flight over a known distance. Particles with different masses can be identified once their times of flight and momenta are known. The difference in flight time for two particles with equal momenta  $p_1 = p_2 = p$  and different masses  $m_1$  and  $m_2$  is given by :

$$\Delta t = \frac{Lc}{2p^2}(m_1^2 - m_2^2).$$

The main purpose of the TOF is particle identification at low- $p_T$  ( $p_T < 2.5$  GeV). It provides a good separation of electrons from kaons and protons up to a track momentum  $p_T \simeq 2.5$  GeV/ $c$  and  $p_T \simeq 4$  GeV/ $c$ , respectively. Furthermore, the TOF information is combined with that of the TPC and ITS to improve track reconstruction.

## 2.4 Time of Flight

---

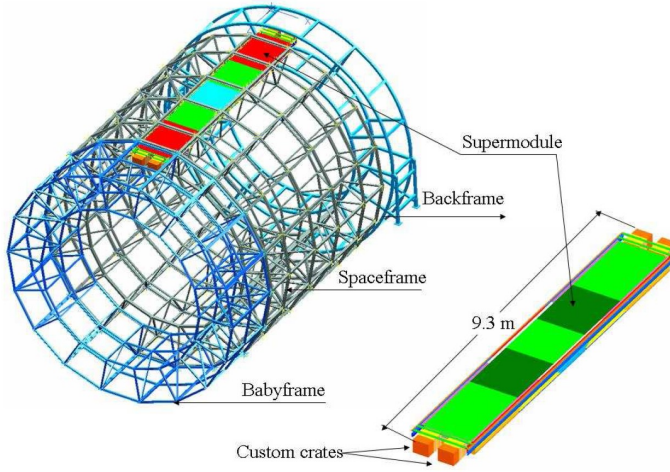


Figure 2.6: The ALICE Time Of Flight detector. Figure taken from [62].

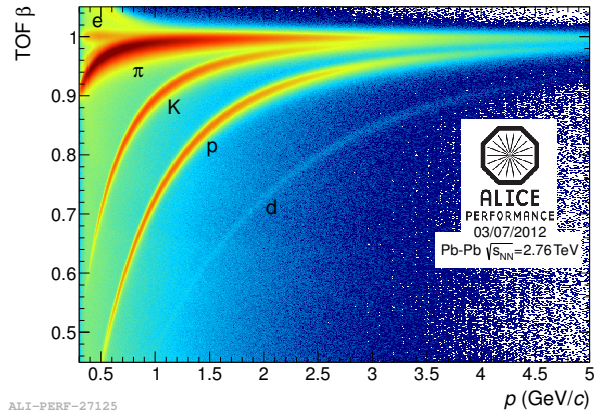


Figure 2.7: Measurement of the velocity of different particle species as function of charged particle momentum with the TOF detector for Pb-Pb collisions.

### 2.5 Electromagnetic Calorimeter

In order to enhance the capabilities for measuring jets, direct photons and electrons from heavy-flavour decays, the electromagnetic calorimeter EMCal [69] was installed in ALICE.

The EMCal is located adjacent to the ALICE magnet coil at a radius of  $\sim 4.5$  m from the beam line. The full detector spans  $|\eta| < 0.7$  in pseudorapidity with an azimuthal acceptance of  $\Delta\phi = 107^\circ$ . The size of the EMCal is constrained by the available free space and the maximum weight that can be supported by the L3 magnet.

The detector contains several modules each consisting of sampling calorimeters made of alternating layers of 1.44 mm Pb and 1.76 mm polystyrene, the latter is the scintillating material [69]. The cell size of the EMCal is approximately  $0.014 \times 0.014$  rad in  $\Delta\phi \times \Delta\eta$ . It is optimized to measure jet production rates and their fragmentation functions in conjunction with charged particle tracking in the other detectors. The energy resolution was measured to be  $1.7 \oplus 11.1/\sqrt{E(\text{GeV})} \oplus 5.1/E(\text{GeV})\%$  [76].

Particles produce an electromagnetic shower when traversing the detector. Due to the choice of the cell size and the detector thickness ( $\sim 20.1$  radiation length), the shower produced by a particle is used to discriminate among electromagnetic and hadronic probes. Electrons and photons deposit their total energy in the detector, while hadrons deposit only a small fraction of their energy.

The EMcal has also been used to provide a fast and efficient trigger (Level 0 and Level 1) for jets, photons and electrons. The Level 0 trigger requires a certain energy deposit in patches of  $4 \times 4$  cells. At Level 1 the EMCal provides triggers on the neutral components of jets and photons. More detail on the EMCal trigger and on the data sample used are reported in chapter 4.

## 2.6 VZERO detector

The VZERO detector [71] consists of two arrays of 32 scintillators each. They are arranged in four rings around the beam pipe on either side of the interaction region, covering the pseudo-rapidity ranges  $2.8 < \eta < 5.1$  (VZERO-A) and  $3.7 < \eta < 1.7$  (VZERO-C), respectively.

The VZERO is used to select beam-beam interactions in the central region of ALICE and to discriminate against interactions of the beam with gas molecules in the beam pipe. For Pb–Pb collisions, the signal amplitude from its segments is used to classify events according to their centrality, while the azimuthal segmentation allows for an estimation of the reaction plane.



---

---

## Chapter 3

# Flow analysis methodologies

---

---

Elliptic flow, first mentioned in section 1.4.2, is described by the second Fourier coefficients of the azimuthal distribution of the invariant particle yield with respect to the reaction plane [11]. In this equation the elliptic flow coefficient is defined as a correlation with the reconstructed event plane. Another experimental technique to measure the elliptic flow coefficient is the scalar product method, a two-particle correlation technique.

Recently a clear disadvantage of using the standard event plane method has been pointed out [77]. The event plane method yields ambiguous  $v_2$  measurements which are somewhere between the event-averaged mean value  $\langle v_2 \rangle$  and the root-mean-square value  $\sqrt{\langle v_2^2 \rangle}$ . The exact value measured from the event plane method depends on the resolution  $R_2$  (which will be defined in equation: 3.5), which strongly depends on the experimental setup. Therefore, the event plane method could lead to systematically different  $v_2$  results obtained in different experiments, complicating a comparison with theoretical model calculations. This dependence has been shown to be stronger for higher harmonic coefficients than for  $v_2$ . In order to provide non ambiguous measurements, it has been suggested [77] to measure the elliptic

flow coefficient (as well as higher order harmonics) with the scalar product method, which has the advantage of measuring always the  $\sqrt{\langle v_2^2 \rangle}$ , removing any ambiguity from the experimental elliptic flow measurements.

In this chapter the event plane method and the scalar product method, both used in this thesis to carry out elliptic flow measurements, are described in detail.

## 3.1 Event plane method

In order to determine the second harmonic coefficient  $v_2$ , the  $\vec{Q}_2$  vector, as defined in equation 3.1, is calculated from the azimuthal distribution of charged particles (so called Reference Flow Particles RFP)

$$\vec{Q}_2 = \sum_{i=1}^N w_i e^{2i\varphi_i}, \quad (3.1)$$

where  $\varphi_i$  are the azimuthal angles and  $N$  the multiplicity of the RFP. The weight  $w_i$  is described later in the text. The azimuthal angle of the  $\vec{Q}_2$  vector

$$\psi_2 = \frac{1}{2} \tan^{-1} \left\langle \frac{Q_{2,y}}{Q_{2,x}} \right\rangle \quad (3.2)$$

is called the event plane,  $\psi_2$ , and is an estimate of the symmetry plane. The observed  $v_2$  is then calculated using equation 3.3:

$$v_2^{obs} = \langle \cos[2(\varphi_i - \psi_2)] \rangle, \quad (3.3)$$

where the averaging is over all particles in all events and  $\varphi_i$  is the azimuthal angle of the particles of interest (POI) for which the  $v_2$  is calculated. In order to avoid autocorrelations the event plane is re-calculated for each particle ( $i$ ) by first removing the track itself from the RFP sample before the  $\vec{Q}_2$  calculation.

### 3.1 Event plane method

---

The measured event plane angle has a finite resolution due to the finite multiplicity of tracks used to reconstruct the  $\vec{Q}_2$ . Because of this, the  $v_2^{obs}$  has to be corrected for the event plane resolution  $R_2$ .

$$v_2 = \frac{\langle \cos[2(\phi - \psi_2)] \rangle}{R_2}. \quad (3.4)$$

The event plane resolution [78], a quantity smaller than one that depends on the multiplicity and  $v_2$  of the RFP, is calculated for equal multiplicity sub-events A and B as:

$$R_2 = \langle \cos[2(\psi_2^A - \psi_2^B)] \rangle. \quad (3.5)$$

Two slightly different methods can be used to calculate the  $v_2$  coefficient. The first one consists of extracting the POI yields with respect to the event plane  $\Delta\varphi = \varphi - \Psi_2$ . For a fixed  $p_T$  bin the number of POIs as a function of  $\Delta\varphi$  is then fitted with equation 3.6, where  $v_2^{obs}$  is in this case a fit parameter and is afterwards corrected for the event plane resolution.

$$dN/d\varphi = N_0 \cdot (1 + 2v_2^{obs} \cos[2(\varphi - \psi_2)]). \quad (3.6)$$

The second and more recent method used in [37] consists of measuring the  $p_T$  spectra of the POIs in the *in*-plane ( $N_{in}$ ) and *out*-of-plane ( $N_{out}$ ) direction as reported in equation 3.7

$$\begin{aligned} N_{in} &= \int_{-\pi/4}^{\pi/4} \frac{dN}{d\Delta\varphi} d\Delta\varphi + \int_{3\pi/4}^{5\pi/4} \frac{dN}{d\Delta\varphi} d\Delta\varphi, \\ N_{out} &= \int_{\pi/4}^{3\pi/4} \frac{dN}{d\Delta\varphi} d\Delta\varphi + \int_{5\pi/4}^{7\pi/4} \frac{dN}{d\Delta\varphi} d\Delta\varphi. \end{aligned} \quad (3.7)$$

Considering only the  $v_2$  coefficient, the integrals can be calculated:

$$\begin{aligned} N_{in} &= a(\pi + 4v_2), \\ N_{out} &= a(\pi - 4v_2), \end{aligned} \quad (3.8)$$

---

### 3. Flow analysis methodologies

---

where  $a$  is a constant factor. From the  $N_{in}$  and  $N_{out}$  yield, and introducing the event plane resolution, it is then possible to calculate the  $v_2$  coefficient according to equation 3.9

$$v_2 = \frac{1}{R_2} \frac{\pi}{4} \frac{N_{in} - N_{out}}{N_{in} + N_{out}}. \quad (3.9)$$

Experimentally the measured elliptic flow is not just the result of the initial spatial anisotropy due to the collision geometry but it can be affected by so-called non-flow contributions. These contributions include resonance decays and jet correlations. The non-flow contributions can be suppressed [79] imposing a pseudo-rapidity gap between the RPF and POIs. In the analysis reported in this thesis the non-flow contributions are suppressed using the three sub-events method [78], in which a large pseudo-rapidity gap is imposed.

#### 3.1.1 Event plane with three sub-events resolution

In order to suppress the non-flow effects, which are correlations not associated with the event plane, a three sub-events technique, which includes a gap between POIs and RFPs in pseudo-rapidity, has been used. If the sub-events do not cover the same pseudo-rapidity range one needs at least three pseudo-rapidity regions to determine the event plane resolution for each of them [78].

In this thesis the  $\vec{Q}_2$  vector is determined from the azimuthal distribution of signals in the segments of the VZERO detectors, which detect particles produced at forward and backward rapidity. The  $\vec{Q}_2$  vector is calculated using equation 3.1, with the sum running over the eight azimuthal sectors of each VZERO detector, where  $\varphi_i$  is defined by the central azimuth of the  $i^{th}$  sector.  $w_i$  is equal to the signal amplitude in the  $i^{th}$  sector for the selected event, which is proportional to the number of charged particles crossing the sector. Non-uniformities in the VZERO acceptance and efficiency were corrected for using the procedure described in [80].

The large gap in pseudo-rapidity ( $|\Delta\eta| > 0.9$ ) between the reconstructed tracks in the TPC (POIs) and those in the VZERO detectors is observed

### 3.2 Scalar product method

---

to suppress non-flow contributions to the measured  $v_2$  [79]. With this procedure the event plane is reconstructed with a different detector compared to the one used for the POIs selection, removing a priori all possible auto-correlations.

The resolution of the event plane determined with the VZERO detectors, equation 3.10, is measured with the three sub-events method [37], using the signals in the VZERO detectors (both A and C sides) and either the tracks in the positive ( $0 < \eta < 0.8$ ) or in the negative ( $-0.8 < \eta < 0$ ) pseudo-rapidity regions of the TPC.

$$R_2 = \sqrt{\frac{\langle \cos[2(\psi_2^{V0} - \psi_2^{TPCpos})] \rangle \langle \cos[2(\psi_2^{V0} - \psi_2^{TPCneg})] \rangle}{\langle \cos[2(\psi_2^{TPCpos} - \psi_2^{TPCneg})] \rangle}}. \quad (3.10)$$

The average  $R_2$  values in the three centrality classes used in this thesis are  $\sim 57\%$  (0-10%),  $\sim 76\%$  (10-20%) and  $\sim 77\%$  (20-40%).

The event plane method for a detector system which has a low resolution of the reconstructed event plane, as observed for the VZERO detectors, gives a  $v_2$  value closer to the root-mean-square value  $\sqrt{\langle v_2^2 \rangle}$  [77] and should give comparable results with the scalar product, if the same pseudo-rapidity gap between POIs and RFPs is applied.

### 3.2 Scalar product method

A more sophisticated two-particle correlation technique is the scalar product, a method that does not depend on explicit construction of an event plane, but calculates  $v_2$  directly from two-particle correlations [81]. It is based on the scalar product of a unit vector for particle  $i$  denoted as  $\vec{u}_2$  with the  $\vec{Q}_2$  vector, calculated as in equation 3.11.

$$v_2 = \frac{\langle \vec{u}_2 \cdot \frac{\vec{Q}_2}{M} \rangle}{\sqrt{\langle \frac{\vec{Q}_2^A}{M^A} \cdot \frac{\vec{Q}_2^B}{M^B} \rangle}} \quad (3.11)$$

### 3. Flow analysis methodologies

---

where A and B are two sub-events and  $M$ ,  $M^A$  and  $M^B$  are the multiplicity of the full-event and the two sub-events A and B, respectively. The scalar product has the additional advantage of providing an easy and detector independent method to compare results from different experiments and with theoretical model calculations.

Also in this case it is important to remove autocorrelations between POIs and RFP from the  $v_2$  measurements by recomputing the  $\vec{Q}_2$  for each particle by first removing the track itself from the RFP sample.

With the scalar-product method, combining measurements from two reference detectors A and B is straightforward if they are identical [77]. One simply has to measure  $v_2$  independently with respect to A and to B. By linearity of the scalar product, the combined  $v_2$  is obtained by taking a plain average between the two measurements as in equation 3.12:

$$v_2 = \frac{1}{2} \left( \frac{\langle \vec{u}_2^A \cdot \frac{\vec{Q}_2^B}{M^B} \rangle}{\sqrt{\langle \frac{\vec{Q}_2^A}{M^A} \cdot \frac{\vec{Q}_2^B}{M^B} \rangle}} + \frac{\langle \vec{u}_2^B \cdot \frac{\vec{Q}_2^A}{M^A} \rangle}{\sqrt{\langle \frac{\vec{Q}_2^A}{M^A} \cdot \frac{\vec{Q}_2^B}{M^B} \rangle}} \right). \quad (3.12)$$

The  $\vec{u}_2^A$  ( $\vec{u}_2^B$ ) is the unit vector of POIs in sub-event A (sub-event B). The sub-event procedure is applied in this thesis in order to avoid autocorrelations between the POI candidates and the  $\vec{Q}_2$  vectors and in order to suppress the non-flow contributions.

The sub-events method uses the  $\vec{Q}_2$  vectors of reconstructed TPC tracks in the positive ( $0 < \eta < 0.8$ ) and negative ( $-0.8 < \eta < 0$ ) pseudo-rapidity regions separately. The two sub-events A and B defined in this way have similar multiplicity and  $v_2$ . The  $\vec{Q}_2^A$  and  $\vec{Q}_2^B$  are calculated using equation 3.1, where the sum is over reconstructed tracks in the TPC selected with the following criteria: at least 70 associated space points out of the maximum of 159, a  $\chi^2$  per TPC cluster in the range  $0.2 < \chi^2/\text{ndf} < 4$  and a transverse momentum in the interval  $0.2 < p_T < 5$  GeV/c. In addition, tracks are rejected if their distance of closest approach to the primary vertex is larger than 3.2 cm in the z directions and 2.4 cm in the (x,y) plane. In order to minimize the non-uniformities in the azimuthal acceptance, no requirement was applied on the number of ITS points associated to the track.

### 3.3 Q-Cumulant and multi-particle correlation

---

The weights  $w_i$  correct for non-uniformities in the acceptance and for the efficiency of the TPC [78]. The  $\vec{Q}_2$  vectors are then correlated with the POI candidates coming from the opposite  $\eta$  region. To reduce the statistical errors on the final measurements an  $\eta$  gap between POIs and RPF of  $|\Delta\eta| > 0$  has been used in this thesis.

#### 3.2.1 Scalar product with three sub-events

If the two sub-events A and B cover an asymmetric pseudo-rapidity region, the usage of the modified Scalar Product method with three sub-events [77, 82] has been introduced. It calculated using to equation 3.13

$$v_2 = \sqrt{\frac{\langle \vec{u}_2^A \cdot \frac{\vec{Q}_2^B}{M_B} \rangle \langle \vec{u}_2^A \cdot \frac{\vec{Q}_2^C}{M_C} \rangle}{\langle \frac{\vec{Q}_2^B}{M_B} \cdot \frac{\vec{Q}_2^C}{M_C} \rangle}}, \quad (3.13)$$

where  $M_B$  and  $M_C$  are the estimates of the multiplicity in the VZERO-A and VZERO-C detectors, and  $\vec{Q}_2^B$ ,  $\vec{Q}_2^C$  are the flow vectors calculated in sub-events B and C, respectively. The non uniformity of the detector azimuthal efficiency is also taken into account in the scalar produce method by applying the inverse of the event-averaged signal as a weight for each of the VZERO segments, together with a re-centring procedure (i.e. subtraction of the average centroid position of each sector [80]). The sub-event A, from which the POIs are selected, is within the full TPC detector and also in this case a pseudo-rapidity gap of  $|\Delta\eta| > 0.9$  is applied by default, largely suppressing non-flow contributions in the  $v_2$  measurements.

### 3.3 Q-Cumulant and multi-particle correlation

As already explained, non-flow correlations that bias the elliptic flow measurements originate largely from few particle correlations like resonance decay (which usually involve two correlated decay products) and structures like mini-jets. Genuine multi-particle correlation methods that involve more

### 3. Flow analysis methodologies

---

than just two particles have the property to drastically reduce the non-flow correlations [83].

One of the problems in using multi-particle correlations is the computing power needed to go over all possible particle multiplets, which practically prohibits calculations of correlations of order larger than three-particle correlations. To avoid this problem, it was suggested in [84] to express cumulants in terms of moments of the magnitude of the corresponding flow vectors  $\vec{Q}_n$ , which are calculated in a single pass over the particles.

To estimate how non-flow in 2-particle correlations scales, for the case of two-particle resonance decay a simple combinatorics argument can be used. Since the average needs to be computed over all pairs, the probability for a particle to be correlated with another one is proportional to  $1/(M-1)$  with  $M$  the number of particles in an event. This means that the magnitude of the non-flow correlation will be proportional to:

$$\delta_{2\text{-particle}} \sim \frac{1}{M}. \quad (3.14)$$

The same type of arguments can be applied to genuine 4-particle correlations; for which the non-flow will be proportional to:

$$\delta_{4\text{-particle}} \sim \frac{1}{M^3}, \quad (3.15)$$

which means that the genuine 4-particle correlations are less affected by non-flow correlations with respect to the 2-particle technique. For the Q-cumulant approach [83, 84] the 4-particle cumulant explicitly removes all 2-particle correlations and it is therefore unbiased by 2-particle non-flow. Due to equation 3.15, the 4-particle cumulant is also reasonably insensitive to 4-particle non-flow correlations, which are expected to be rare to begin with. In this thesis the 4-particle cumulant method has been tested in order to compute the elliptic flow for the different analyses. Unfortunately in these specific cases, the small statistics of the particles of interest, and hence the small numbers of quadruplets reconstructed, did not allow to extract statistically reliable measurements using a 4-particle correlation technique.

---

---

## Chapter 4

# Event selection

---

---

In this chapter the criteria applied to select a clean sample of data, used in the different flow analyses carried out in this thesis, is described. Collisions between lead ions recorded by the ALICE detector in the years 2010 and 2011 at a collision energy of  $\sqrt{s_{NN}} = 2.76$  TeV are used. According to the statistics required, dictated by the different analyses reported in this thesis, the 2010 or 2011 Pb–Pb data have been used. For the  $\phi$ -meson and the direct photon analysis the 2010 minimum bias data sample was used, while for the heavy-flavour decay electrons, due to the large statistic required in this analysis, the 2011 data have been used. Due to different detector conditions in the two data taking periods, the different data samples have not been mixed. In addition, a sample of EMCal trigger events has been used in order to extend the heavy-flavour decay electrons measurements to higher transverse momentum. In the last section of this chapter detailed studies on charged particle elliptic flow using the EMCal triggered events are reported. This check was done to verify if this triggered data sample can be safely used for azimuthal anisotropy measurements.

## 4.1 On-line and Off-line event selection

In this section a brief introduction to the different trigger setting used to record events with the ALICE detector is given. The trigger setting between the data recorded in 2010 and 2011 are slightly different, for instance in the 2011 data not only minimum bias events (MB) were recorded, but also specific centrality and more rare triggers have been employed.

The selection of the minimum bias events was done using a combination of online and offline triggers [85]. The online minimum bias trigger used to record the data, which is a hardware level trigger, used in Pb–Pb collisions requires the following conditions to be satisfied:

- two hits in the outer layer of the SPD
- signal in VZERO-A
- signal in VZERO-C

Usually an event is selected when two out of the three conditions are met, however, depending on the run conditions different triggering scenarios were used for the selection, such as a full coincidence between the requirements (3-out-of-3) or only a signal in both the VZERO detectors. The VZERO-based trigger was complemented by a requirement of signals in both ZDCs in order to suppress the electromagnetic interactions between the lead ions during the high luminosity Pb–Pb runs in 2011.

The centrality trigger employed in 2011 data is mainly based on the same conditions listed for the MB bias trigger with an additional threshold requirement on the integrated VZERO signals. This threshold was used to define central 0-10% and semi central 0-50% Pb–Pb triggers. The threshold was applied separately to the sums of the output charges of the VZEROA and VZEROC, and a coincidence of the two sides was required.

Furthermore, an off-line selection is applied in which the on-line trigger is validated and the remaining background events from beam-gas interactions are rejected using the time measured in the VZERO detector at which the

## 4.1 On-line and Off-line event selection

---

particles arrive with respect to the time when the bunch crossed the nominal interaction point in ALICE.

In addition to the MB centrality triggers, also other more rare triggers have been used in ALICE to select events. One of the EMCal triggers is based on the EMCal single shower (SSh) trigger, which utilizes the fast hardware based sum of transverse energy ( $E_T$ ) in groups of  $4 \times 4$  adjacent EMCal towers (corresponding to  $0.056 \times 0.056$  in  $\phi \times \eta$ ). An SSh trigger is issued if the threshold is exceeded by at least one EMCal tower group. The nominal trigger threshold varied approximately from  $\sim 7$  GeV in 0-10% most central events to  $\sim 2$  GeV in 80-90% most peripheral events. An event is accepted if it also passes the MB trigger requirements.

### 4.1.1 Additional event selection

After the standard ALICE physics selection, additional filtering on the recorded events is necessary to further clean up the data sample used for the analysis described in this thesis.

One of the most important quantities is the reconstruction of the primary interaction vertex. Global tracks, reconstructed in the TPC and ITS, are used to find the interaction vertex with high precision. Only events with at least two tracks and a vertex found within 10 cm from the centre of the detector along the beam line are used in the analysis ( $|V_z| < 10$  cm). The value of the primary vertex cut is chosen to ensure a uniform reconstruction efficiency of charged particles. The primary interaction vertex can also be estimated using the two innermost layers (SPD) of the ITS. If the absolute difference between the primary vertex estimated in the two strategies is larger than 0.5 cm the event is not selected.

As an additional quality check on the events, the correlation between the Global track and standalone TPC track multiplicity have been investigated, to check if outlier/pile-up events are observed. Some of the events are affected from outliers as shown in Fig. 4.1, where the correlation between Global and TPC tracks is shown for the 2011 centrality trigger events. The events for which the multiplicity values measured in the two cases do not follow the expected correlation are most probably affected by pile-up. These

## 4. Event selection

outliers are only visible for standalone TPC tracks, because the dead time in the TPC is much larger than that in the ITS. The TPC multiplicity outliers were removed, for both the 2010 and 2011 data, by a correlation cut placed at a  $3\sigma$  distance from the central value of the correlation band, plotted in Fig. 4.1 by the red lines.

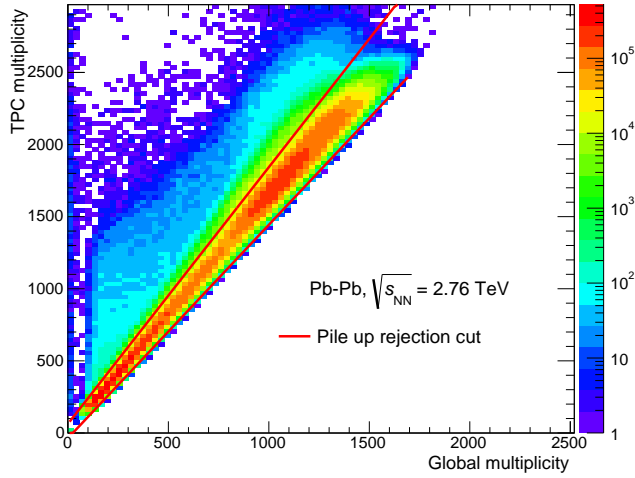


Figure 4.1: Correlation between the number of global tracks (ITS+TPC) and standalone TPC tracks for the 2011 Pb–Pb centrality trigger. The red line represent the cut placed at a  $3\sigma$  distance from the central value of the correlation band.

The multiplicity measured in the VZERO detectors is used to estimate the event centrality, as explained in detail in the next section. Since the impact parameter distribution could slightly depend on the acceptance of the detector used for the centrality determination, this was investigated by comparing the centrality value measured by the VZERO with the one measured using the number of tracks in the TPC. Events that have an absolute difference larger than 5% between the two estimates are rejected from the event sample.

Finally in Table 4.1 all the additional event cuts applied to clean the

## 4.2 Centrality determination

---

data sample are listed. The total number of events rejected by the event cuts is about 2.5%. The event sample analyzed is verified to be an unbiased sample for the centrality intervals used in the analysis.

Type	Value
# of tracks	$> 2$
$ V_z $	$< 10 \text{ cm}$
$ SPD_{V_z} - TPC_{V_z} $	$< 0.5 \text{ cm}$
Global vs TPC multiplicity	required
$ V0^{cent} - TPC^{cent} $	$< 5\%$

Table 4.1: Event selection cuts.

## 4.2 Centrality determination

Measurements in heavy-ion collisions are usually reported as a function of the collision centrality. Head-on collisions are referred to as *central* collisions, in which thousands of particles are produced. The collisions in which the overlap region between the two nuclei is small are called *peripheral*, and for those collisions the particle multiplicity is much lower than for the most central. Ideally the centrality would be determined by the impact parameter  $b$ , however this geometrical parameter is not known in experiments.

Experimentally, the centrality is defined [86] as the fraction of the number of observed events  $N_{ev}$  (corrected for the trigger efficiency and for the non-hadronic interaction background) with the largest detected charged particle multiplicity  $N_{ch}$ :

$$c \approx \frac{1}{N_{ev}} \int_{N_{ch}}^{\infty} \frac{dN_{ev}}{dN'_{ch}} dN'_{ch}, \quad (4.1)$$

where the assumption is made that the particle multiplicity increases monotonically with centrality at mid-rapidity. The connection between the experimental centrality definition and the model dependent quantities is

calculated with the Glauber Monte-Carlo model [87, 88]. It defines, for an event with a given impact parameter  $b$ , the corresponding  $\langle N_{part} \rangle$ , which are the nucleons which at least had one collision, and  $\langle N_{coll} \rangle$ , which are the total number of binary nucleon-nucleon collisions. In the model a nucleus-nucleus collision is treated as a sequence of independent nucleon-nucleon collisions, where the nucleons are assumed to travel on straight line trajectories and the inelastic nucleon-nucleon cross section is assumed to be independent of the number of collisions a nucleon underwent previously. The Glauber Monte-Carlo model is then augmented with a simple two-component model for particle production (in which both  $\langle N_{part} \rangle$  and  $\langle N_{coll} \rangle$  contribute to the total multiplicity) to simulate the multiplicity distribution using a negative binomial distribution (NBD). To use this model for a collision with a given  $\langle N_{part} \rangle$  and  $\langle N_{coll} \rangle$ , the number of independently emitting sources of particles is assumed to be parameterized as  $f \times N_{part} + (1 - f) \times N_{coll}$ . The distribution of the measured VZERO signal amplitude, which is proportional to the event multiplicity, is shown in Fig. 4.2. The distribution is overlaid with the amplitude distribution simulated with the NBD-Glauber model (red line in the figure).

In ALICE several detectors can be used to measure the charged particle multiplicity in order to determine the centrality of a collision. As already mentioned in the previous section on the event selection cuts, in this thesis both the sum of the amplitudes in the VZERO detector and number of reconstructed tracks in the TPC are used as centrality estimators. The VZERO amplitude is used as the default method for the analysis discussed in this thesis, because it has a better resolution compared to the other detectors. The resolution in the centrality estimated for the VZERO detector ranges from 0.5% in central to 2% in peripheral Pb–Pb collisions.

#### 4.2.1 Centrality flattening for the 2011 data

Anisotropic flow measurements depend on the centrality, hence a flat centrality distribution is necessary to ensure that each narrow centrality bin contributes equally to the measured  $v_2$  in a wider bin, and to ensure that the centre of a wide centrality bin represents the mean centrality.

## 4.2 Centrality determination

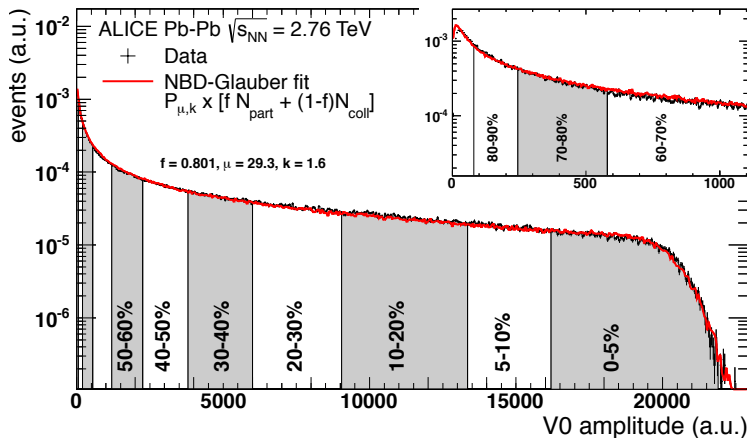


Figure 4.2: Distribution of the V0 amplitude (sum of V0A and V0C) for the 2010 MB bias events. The inset shows a zoom of the low amplitude part of the distribution. The curve shows the result of the Glauber model fit to the measurement. Figure taken from [86]

For the 2010 MB data the centrality distribution is observed to be fully uniform over the whole range used in the analysis. Due to the threshold applied on the signal of the VZERO detectors in the 2011 centrality trigger, it was 100% efficient up to  $\sim 8\%$  centrality. This is reflected in the centrality distribution, as shown in Fig. 4.3, which is approximately flat up to  $\sim 8\%$ . Between 8% - 10% centrality the effect of the trigger becomes visible. This shows that in order to use a wider centrality bin in the flow analysis, for example 0-10%, a correction has to be applied.

To account for the trigger bias a centrality flattening procedure is used. The centrality distribution of the triggered events is used to define centrality weights  $w_i$  in 1% wide bins, defined as the ratio between the minimum of the centrality distribution in the range in which the flattening has to be applied and the value of the centrality distribution in the bin. The weights for the 0-10% centrality range are reported in the left panel of

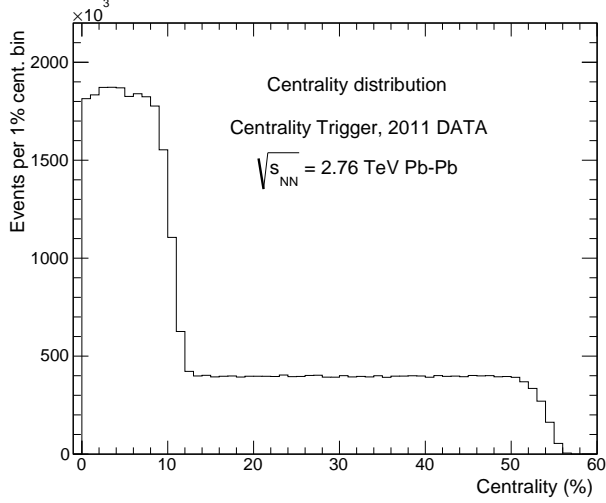


Figure 4.3: Centrality distribution evaluated in case of the 2011 centrality trigger.

Fig. 4.4. The minimum value of events in the centrality distribution is between 9% and 10% and as expected in this interval the weights are equal to one. For the flattening, events are assigned a random number between  $0 < y < 1$  based on the centrality value and are rejected if  $y > w_i(x)$ . The number of events rejected with this procedure is  $\sim 14\%$  of the full event statistics in the 0-10% centrality class. This procedure has been applied because it had already been used previously for the heavy-flavour elliptic flow measurements [37]. In addition, a weighting procedure that uses extra event weights, as explained later in the text for the event plane, has been used. The centrality distribution, after the rejection of the events in the 0-10% centrality class, and after all the selection cuts previously explained, is shown in the right panel of Fig. 4.4, where the centrality classes are separated and reported according to those used in the heavy-flavour decay electrons analysis for which the 2011 centrality trigger is employed. Finally the total number of events analyzed in this thesis from the 2010 and 2011

### 4.3 Event plane determination

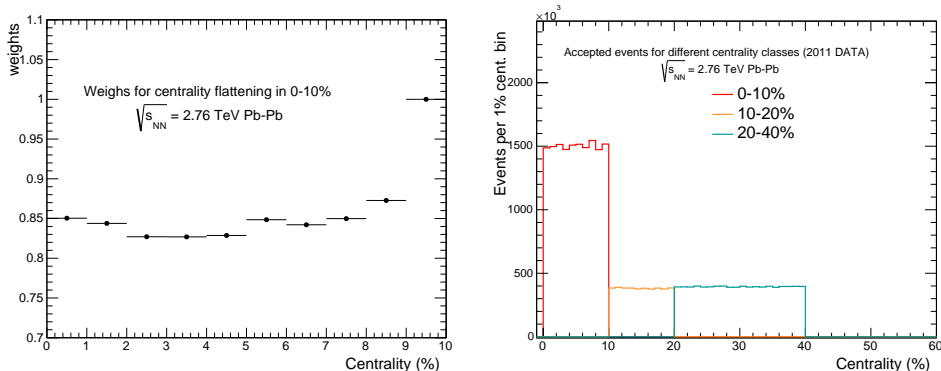


Figure 4.4: Left panel: centrality weights as a function of the centrality percentile used for the flattening procedure in the 0-10% centrality class. Right panel, centrality class distribution after that all event cuts have been applied for the 2011 centrality trigger.

data sample for different triggers are summarized in Table 4.2.

### 4.3 Event plane determination

The orientation of the  $2^{nd}$ -harmonic collision symmetry plane is estimated with the  $2^{nd}$ -harmonic event-plane angle,  $\Psi_2^{EP}$ . As previously explained, one constructs the  $\vec{Q}_2 = (Q_{2,x}, Q_{2,y})$  from the measured azimuthal distribution of particles produced in the event with a specific detector. The event plane can then be calculated using the following equation:

$$\Psi_2^{EP} = \frac{1}{2} \arctan 2(Q_{2,y}, Q_{2,x}), \quad (4.2)$$

where  $\arctan 2(x, y)$  returns the arc tangent of  $\frac{x}{y}$  in the interval  $(-\pi, \pi]$ . In this section the event plane determination using the VZERO detector for the 2011 data will be discussed. Measurements and comparison with published results [79] of charged particle  $v_2$  are reported for different cases, to check possible biases in the flow measurements.

#### 4. Event selection

Data	Centrality class	Trigger	$N_{ev}$
2011			
	0 - 10%	Centrality	$\sim 15 \times 10^6$
	10 - 20%	Centrality	$\sim 4 \times 10^6$
	20 - 40%	Centrality	$\sim 8 \times 10^6$
	10 - 20%	EMCal Ssh	$\sim 7 \times 10^5$
	20 - 40%	EMCal Ssh	$\sim 1 \times 10^6$
2010			
	10-60%	Minimum Bias	$8 \times 10^6$

Table 4.2: Summary of the final number of events analyzed in this thesis.

In order to ensure a flat  $\Psi_2^{EP}$  distribution the V0 detector has to be calibrated to correct for effects from detector inefficiencies. The calibration is done in two steps according to the procedure reported in [80]: gain equalization of the VZERO detector signal and re-centering of the flow vector  $\vec{Q}_2$ .

Even after the VZERO calibration and  $\vec{Q}_2$  re-centering have been properly applied, a non-flat distribution of the event plane is observed for the 0-10% most central events, where the trigger bias discussed in the centrality determination section is not negligible. For the 10-20% and 20-40% the measured event plane distribution is flat after the calibration. The event plane distributions measured with the VZERO detector in the different centrality classes are plotted in Fig. 4.5.

The observed non-flatness of the event plane distribution in the 10% most central collisions could lead to a bias in the elliptic flow measurements if the azimuthal distribution of the POIs is not completely flat due to detector effects. For instance, if the tracks are required to have a matching cluster in the EMCal detector, the resulting  $\varphi$  distribution of the POIs would be restricted to the azimuthal acceptance of the calorimeter. In addition, in the 2011 data, a few pixel chips in the SPD detector were damaged, so when

### 4.3 Event plane determination

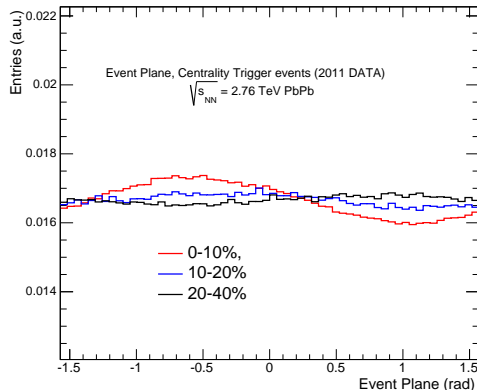


Figure 4.5: Event plane distribution measured using the VZERO detector for the different centrality classes using the 2011 centrality trigger data.

for each track one or two hits are required in the two innermost ITS layers<sup>1</sup>, holes in the azimuthal distribution of the tracks are observed.

To check for possible effects introduced by the non-flatness of the VZERO event plane in 0-10% centrality class, charged particle  $v_2$  is measured using standalone TPC tracks (which are isotropic in azimuth) for which no bias is expected for the  $v_2$  measurement, and also requiring a match in the EMCal detector in order to have a very limited  $\varphi$  acceptance. The results, together with the measured charged particle  $v_2$  published by ALICE [79] using the 2010 MB data sample, are shown in Fig. 4.6 for the three different centrality classes. In the left panel the 0-10% centrality class is shown, while in the middle and in the right panels the 10-20% and 20-40% are reported. The ALICE published results, plotted with open blue markers, are measured with the VZERO event plane method as well, and are used as comparison for the results measured here using the 2011 data sample.

The magenta markers represent the  $v_2$  results in case the POIs are selected using standalone TPC tracks, and as expected those results do not show any bias in the  $v_2$  measurements in all the centrality classes. They are

---

<sup>1</sup>for instance in the case of the heavy-flavour decay electron analysis (chapter 6)

## 4. Event selection

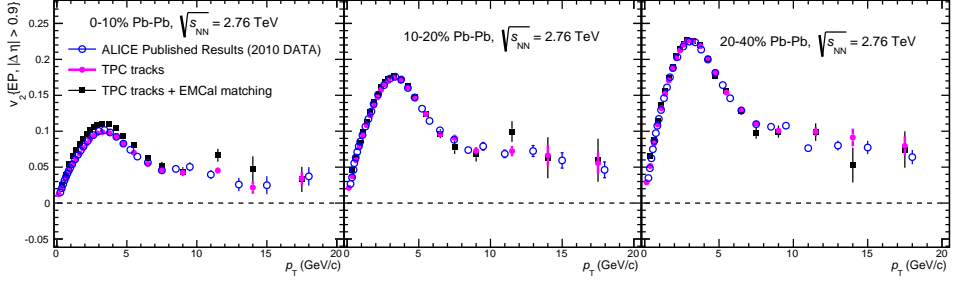


Figure 4.6: Charged particle  $v_2$  measured with different detector combination using the 2011 centrality trigger sample. Standalone TPC and TPC+EMCal are plotted with magenta and black markers respectively. For comparison also the ALICE published measurements are plotted with the open blue markers. All the results are measured with the event plane VZERO method.

fully compatible with the previous ALICE measurements within their statistical uncertainties. On the other hand, when EMCal matching is required for selecting the POIs, the measured charged particle  $v_2$ , reported with the black markers, shows a systematic difference resulting in higher  $v_2$  values for the full  $p_T$  region in the 0-10% central class, where the non-flatness of the event plane is observed. It is important to mention that measurements with the EMCal calorimeter below  $p_T < 2$  GeV/c are affected from the very limited detector resolution. Nevertheless the TPC+EMCal  $v_2$  measurements are compatible with the published results within the statistical uncertainties in the 10-20% and 20-40% centrality classes, where the event plane distribution is observed to be flat. From this comparison it is clear that a correction to the event plane distribution in the 0-10% centrality class has to be applied.

### 4.3.1 Further correction in most central collision

An event weighting approach has been used for the charged particle  $v_2$  in order to correct for the event plane bias in the 0-10% centrality. The weights

## 4.4 EMCal Trigger studies

---

$w_i$  are evaluated with the following equation:

$$w_i = \frac{\langle N \rangle}{N_i} \quad (4.3)$$

where the average expected number of events per bin of the event plane distribution,  $\langle N \rangle$ , is estimated from integrating the even plane distribution, reported in Fig. 4.5, and dividing the integral value by the total number of bins. The weights are obtained dividing  $\langle N \rangle$  by the observed number of events in a given event plane bin  $N_i$ . As was done for the centrality flattening, see section 4.2.1, a random rejection of events has been used in order to check the stability of the approach. The resulting even plane distributions in 0-10% centrality, corrected using the two different approaches, are reported in the left panel of Fig. 4.7 together with the reconstructed event plane distribution before the corrections. For both the strategies, the event plane distribution after correction becomes completely flat in the 0-10% centrality class.

In the right panel of Fig. 4.7 the charged particle  $v_2$  measurements, for which EMCal matching is required, before and after the event plane correction are shown. The published charged particle  $v_2$  is plotted again for comparison. After the corrections have been applied the charged particle  $v_2$  results are compatible within statistical uncertainties with the previous ALICE measurements. Both correction procedures are observed to restore the charged particle  $v_2$  values, removing the bias introduced by the non-flatness of the event plane. The weighting procedure correction, which has the advantage of preserving the full event statistics, is applied for the heavy-flavour decay electron  $v_2$  analysis reported in chapter 6.

## 4.4 EMCal Trigger studies

In this last section, detailed studies on the event plane determination and on charged particle  $v_2$  are reported for the EMCal single shower trigger events. Since this specific set of triggered data has been used to extend the heavy-flavour decay electrons  $v_2$  measurements to higher  $p_T$ , these studies have

## 4. Event selection

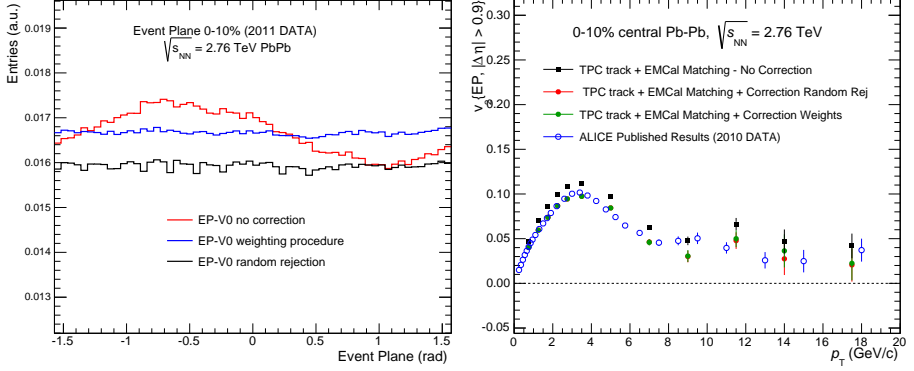


Figure 4.7: Left panel: Event plane distribution measured using the VZERO detector in the 0-10% centrality class for the 2011 centrality trigger data before and after corrections. Right panel: Charged particle  $v_2$  measured with the TPC and EMCal detectors before (black marker) and after corrections, green marker for weighting and red marker for event rejection, compared to the ALICE published results from 2010 MB data.

been performed to check possible trigger biases that could affect elliptic flow measurements.

A simple toy MC model [89, 90], has been used to investigate possible trigger biases. The event plane distribution is sampled from a uniform distribution, but the events are analyzed only when the trigger condition is met. In the toy model and in data, the events are accepted, if a high  $p_T$  track ( $p_T \geq 5$  GeV/c) ends up in a specific  $\eta$  and  $\varphi$  region selected according to the EMCal geometry. The results from this simple toy MC are shown in Fig. 4.8. In the left panel the event plane distribution of the triggered events is shown, while the right panel shows the comparison of the generated (red line) and reconstructed (black marker)  $v_2$ .

It is seen that the event plane distribution obtained from the triggered events is not a flat distribution due to the trigger. The comparison between the generated and reconstructed  $v_2$  shows that above the trigger threshold the reconstructed  $v_2$  is fully compatible with the generated value. However,

## 4.4 EMCal Trigger studies

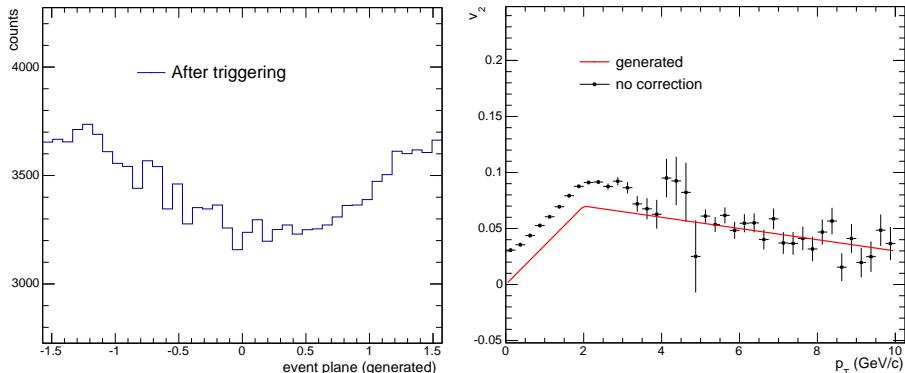


Figure 4.8: Left Panel: Event plane distribution of triggered events in a simple toy MC model. Right panel: Comparison of generated and reconstructed  $v_2$  in the same toy MC. See text for more details.

below the threshold the  $v_2$  values are not properly reconstructed due to the trigger threshold bias. In conclusion this simple toy MC model shows that no bias is expected in the  $v_2$  measurements above the trigger threshold and that the non-flatness of the event plane is indeed introduced by triggering on an high  $p_T$  particle.

After those simple MC studies the Ssh trigger data have been analyzed, in order to understand if the same effect observed in MC is seen also in data. The centrality and the event plane distributions, both measured via the VZERO detector as previously described, are reported in the left and right panel of Fig. 4.9 respectively.

The centrality distribution, due to the trigger bias, is not flat, but due to the small event statistics in the trigger sample, the centrality distribution is not further corrected for these preliminary studies. The event plane distribution is shown for the same centrality classes, namely 0-10%, 10-20% and 20-40%. For the EMCal Ssh trigger data the event plane distribution is observed to be not flat in all the three centrality classes. Since the Ssh trigger data are a sub-sample of the centrality trigger, this observation reflects the behaviour observed in MC, however different for the 0-10% centrality,

## 4. Event selection

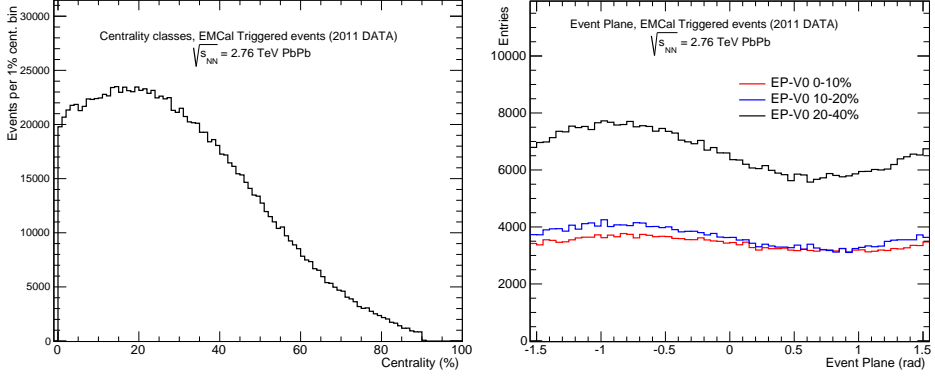


Figure 4.9: Centrality (left panel) and event plane (right panel) distributions evaluated in case of the EMCal single shower trigger events.

where the event plane is observed not to be flat after the calibration even in the minimum bias centrality trigger.

After the event plane determination for the EMCal triggered events, the elliptic flow for charged particles has been measured. In Fig. 4.10 the charged particle  $v_2$  for the 0-10% and for the 20-40% centrality classes is shown in the left and right panel respectively.

Once more, for comparison, the ALICE published results measured with the same methods are shown with the blue open markers for these centrality classes. With the magenta markers the centrality trigger results for standalone TPC tracks are plotted as well. Finally the  $v_2$  measurements are shown for the Ssh trigger with red markers for which matching with a cluster in the EMCal detector is required for the POI's. For the Ssh trigger the measured charged particle  $v_2$  shows a large bias in both centrality classes below the trigger threshold ( $p_T < 6$  GeV/c), resulting in a systematic higher  $v_2$  with respect to the published results. For the 20-40% results, as also observed in the toy MC model, above the trigger threshold no bias is observed and the correct  $v_2$  is obtained. For the 10% most central collision the measured  $v_2$  shows a large bias even above the threshold. For this

## 4.4 EMCal Trigger studies

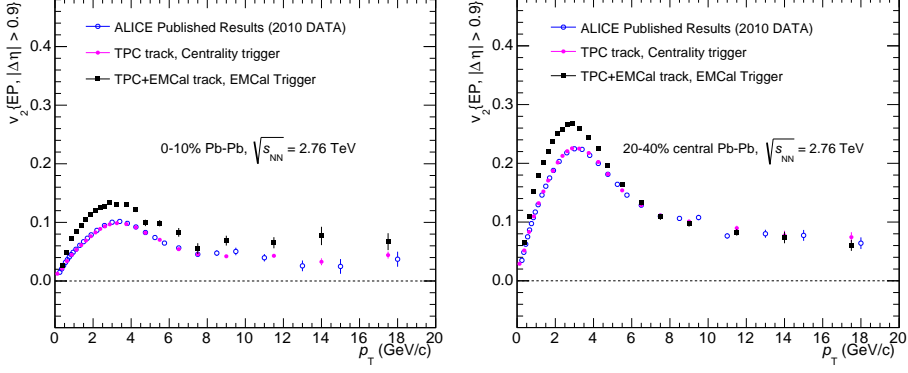


Figure 4.10: Charged particle  $v_2$  measured with different detector combination using the EMCal single shower and centrality trigger from 2011 data sample. All the results are measured with the event plane VZERO method. See text for more details

reason the Ssh trigger events, in the 0-10% centrality class, are not used in this thesis.



---

---

## Chapter 5

# Elliptic flow of $\phi$ -mesons

---

---

In this chapter detailed measurements of the elliptic flow of the  $\phi$ -meson in Pb–Pb collisions will be presented and discussed together with the estimation of the systematic uncertainties. The excellent particle identification capabilities for charged hadrons in ALICE, provides some clear advantages for the  $\phi$ -meson  $v_2$  measurement via the  $K^+ + K^-$  channel. The  $v_2$  results for the  $\phi$ -meson are reported for  $|\eta| < 0.8$  and  $0.6 < p_T < 6.0$  GeV/ $c$  for the centrality intervals covering 10-60% of the inelastic cross section.  $\phi$ -meson measurements constitute a crucial probe of the high energy density medium because the  $\phi$  has a mass similar to that of the proton and  $\Lambda$  baryon, but it is argued that it has a smaller hadronic cross section [12]. Given this smaller cross section, if hadronic re-scatterings are important, a significantly lower  $v_2$  would be expected for the  $\phi$ , because its mean free path (in hadronic matter) is larger. Therefore, the  $\phi$ -meson is a sensitive probe for the flow development mechanisms providing insight to the collective motion of the partonic phase at LHC energies.

In the next sections the full description of the analysis strategy and methods will be given together with a detailed description of the ingredi-

ents necessary to extract the  $\phi$ -meson  $v_2$ , i.e. the signal and combinatorial background extraction from the invariant mass distribution. A comparison of the  $\phi$ -meson elliptic flow with identified charged hadrons elliptic flow [82] measured by ALICE is also shown. In the comparison with the other hadron measurements, mass scaling properties and the number of constituent quark (NCQ) scaling of  $v_2$  have been tested and reported in the section dedicated to the discussion of the physics results. Comparison with theoretical predictions, using a pure hydrodynamic model (VISH2+1) [25] or with a hybrid model including a hadronic cascade afterburner (VISHNU) [26], are reported as well at the end of this chapter.

### 5.1 Two particle resonance flow

Particles that decay via the strong interaction cannot be directly observed in the detector due to their short lifetime and can therefore only be reconstructed from their decay products. For a successful resonance reconstruction, one generally turns to the Lorentz invariant mass  $m_{inv}$ , which for the two-particle case is defined as in equation 5.1

$$m_{inv} = \sqrt{[(E_a + E_b)^2 - (\mathbf{p}_a + \mathbf{p}_b)^2]}, \quad (5.1)$$

where  $a$  and  $b$  are the decay products, with their energy  $E$  and their momentum  $p$ .

The flow analysis techniques explained in chapter 3 can be extended to accommodate resonance flow.

This section will provide a general discussion of the flow of resonance particles [91, 92], and gives a description of the invariant mass fit method that has been used to extract the  $\phi$ -meson elliptic flow coefficient.

One first has to combine a pair of particles to obtain a pair angle  $\varphi_{pair}$ , which, for resonance particles, is taken to be the angle of the total transverse momentum,  $p_T^a + p_T^b$ . For a symmetric colliding system the azimuthal angle distribution with respect to the reaction plane  $\Psi_R$  for pairs can be trivially

## 5.1 Two particle resonance flow

---

rewritten using the Fourier expansion as for single particle studies:

$$\frac{dN}{d\varphi_{pair} - \Psi_R} = \frac{N_0}{2\pi} \left( 1 + 2 \sum_{n=1}^{\infty} v_n^{pair} \cos[n(\varphi_{pair} - \Psi_R)] \right) \quad (5.2)$$

and similarly, the azimuthal dependency of pairs is completely characterized by the pair flow harmonic coefficient,  $v_n^{pair}$ , which means that the flow methods as described in chapter 3 can be applied directly on candidate tracks, which are reconstructed from the daughter particle's mass,  $p_T$ ,  $|\eta|$  and azimuthal angle  $\varphi$ .

Although the  $\phi$ -meson can be reconstructed by means of the invariant mass of its daughters, due to the presence of a large combinatorial background it is not possible to uniquely determine which kaons are daughters of the  $\phi$ -decay. Exploiting the additive property of the elliptic flow coefficient, the kaon pair  $v_2$  can be written according to:

$$N^{pairs}(m_{inv})v_2^{pairs}(m_{inv}) = N^{\phi}(m_{inv})v_2^{\phi}(p_T) + N^{bg}(m_{inv})v_2^{bg}(m_{inv}), \quad (5.3)$$

where  $N^{pairs}(m_{inv})$ ,  $N^{\phi}(m_{inv})$  and  $N^{bg}(m_{inv})$  are the total number of unlike-sign kaon pairs, the number of  $\phi$ -mesons and the total amount of the combinatorial background respectively, extracted from the  $\phi$ -meson reconstruction.  $v_2^{bg}(m_{inv})$  is the elliptic flow of the pairs belonging to the combinatorial background and  $v_2^{\phi}(p_T)$  is the elliptic flow of the  $\phi$ -meson as a function of the transverse momentum.

From equation 5.3 the  $v_2^{pairs}(m_{inv})$  can be trivially derived as:

$$v_2^{pairs}(m_{inv}) = \frac{N^{\phi}(m_{inv})}{N^{pairs}(m_{inv})}v_2^{\phi}(p_T) + \frac{N^{bg}(m_{inv})}{N^{pairs}(m_{inv})}v_2^{bg}(m_{inv}). \quad (5.4)$$

$v_2^{\phi}(p_T)$  is then measured via the invariant mass fit method [92], a technique that consists of measuring the  $v_2^{pair}$  of all kaon pairs as a function of the invariant mass in different  $p_T$  bins. From this the  $v_2^{\phi}(p_T)$  will be

extracted with a fitting routine that takes the output of the  $\phi$ -meson reconstruction in terms of raw yields and background as function of invariant mass.

## 5.2 $\phi$ -meson reconstruction

$\phi$ -meson resonance decays via the strong interaction and does not live long enough to be observed in a detector and can therefore only be reconstructed from their decay products. The main decay channel for the  $\phi$ -meson, with a branching ratio of about 48.9%, is:

$$\phi \longrightarrow K^+ + K^- \quad (5.5)$$

The value of the  $\phi$ -meson's invariant mass given by the Particle Data Group [93] is  $m_{inv} = 1.019445 \pm 0.000020$  (GeV/ $c^2$ ). Starting from the  $K^+ + K^-$  decay channel the  $\phi$ -meson reconstruction is performed in several steps. First the invariant mass distribution of a sample of unlike sign kaon pairs is constructed. After that, the  $\phi$ -meson yield is extracted removing the combinatorial background, where different techniques have been tested, and, in addition, using a set of fitting routines to estimate the residual background.

The quality of the  $\phi$ -meson reconstruction also strongly depends on the kaon selection criteria; therefore an overview of the track selection criteria and particle identification strategies that are specific to this study are given.

### 5.2.1 Track selection

A very important step in the quality assurance is imposing cuts on individual tracks. Track selection is applied to clean up the track sample used in the analysis from unwanted tracking features and other contamination sources, while at the same time maintaining as much as possible the track reconstruction efficiency. A summary of all kinematic constraints and quality track cuts imposed are listed in Table 5.1. Tracks were selected in the mid-rapidity region with a  $|\eta| < 0.8$  to ensure a uniform acceptance and

## 5.2 $\phi$ -meson reconstruction

efficiency in the TPC. Tracks are required to have at least 70 associated clusters in the TPC, which helps in reducing split tracks. The average  $\chi^2$  of the track fit per TPC space point was required to be smaller than 4 (one TPC space point had two degrees of freedom). These selections reduce the contribution from short tracks, which are unlikely to originate from the primary vertex. Only global tracks, defined when the track reconstruction is done with both the ITS and TPC detectors, are accepted. The definition of global tracks also requires a minimum of 2 clusters in the ITS. Finally, kink daughters are rejected.

Kinematic	Type	Range
	$p_T$ (GeV/ $c$ )	(0.2, 5.0)
	$\eta$	(-0.8, 0.8)
Track quality	Type	Requirement
	TPC clusters	> 70
	ITS clusters	> 2
	$\chi^2$ per TPC cluster	[0.1, 4.0]
	TPC dE / dx [au]	> 10
	Require TPC refit	yes
	Require ITS refit	yes
	Accept kink daughters	no
	DCA <sub><math>x,y</math></sub>	$< 0.0105 + 0.035 \cdot p_T^{-1.1}$ (cm)
	DCA <sub><math>z</math></sub>	< 2 (cm)

Table 5.1: Track selection for kaon candidate selection.

In addition to the usual quality track criteria, also a specific selection motivated by this analysis needs to be imposed. Global tracks allow for a precise determination of the DCA <sub>$x,y$</sub>  (distance of closest approach of the track to the primary vertex in the transverse plane) and thus a rejection of secondaries. Secondary tracks are defined here as particles produced from displaced weak decays and from material interactions. A parameterization of the DCA <sub>$x,y$</sub>  is obtained from Monte-Carlo studies, performed on events simulated with the HIJING generator [94], where it is possible to have a

## 5. Elliptic flow of $\phi$ -mesons

clear separation of primary and secondary tracks. A  $p_T$ -dependent cut in the  $DCA_{x,y}$  can be parameterised with a function  $x(p_T)$ . This is evaluated from the r.m.s. of the  $DCA_{x,y}$  distribution of primary tracks in the MC sample. The parameterization is placed at  $5\sigma$  from the mean value obtaining Eq. 5.6.

$$x(p_T) = 0.0105 + \frac{0.035}{p_T^{1.1}} \quad (5.6)$$

To remove secondary tracks, this parameterization is used as a default  $DCA_{x,y}$  cut for the  $\phi$ -meson analysis. The analysis has been redone using also a  $p_T$  independent cut on the  $DCA_{x,y}$  parameter, placed at 0.3 cm, and the effect of this variation is taken into account in the systematic uncertainties. Those two different  $DCA_{x,y}$  cuts are shown by the red lines in the left and right panel of Fig. 5.1.

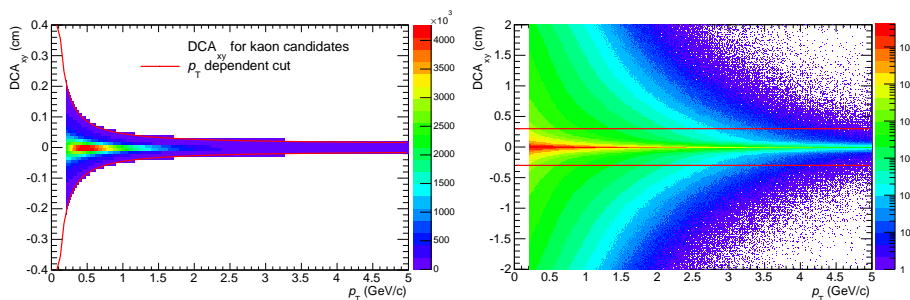


Figure 5.1: The DCA distribution of charged kaon candidates in 10-20% centrality.  $p_T$  dependent (left) and independent (right) cuts are shown.

In the left panel the  $DCA_{x,y}$  distribution is shown only for the kaon tracks that pass the  $DCA_{x,y}$  selection, while in the right panel the full  $DCA_{x,y}$  distribution for identified charged kaons is shown.

### 5.2.2 Bayesian particle identification

ALICE has several detectors providing particle identification information as explained in chapter 2. In the  $\phi$ -meson analysis the TPC and TOF detector

## 5.2 $\phi$ -meson reconstruction

---

signals have been used. In general, each detector measures a certain raw signal, and one of the simplest ways of performing particle identification is to directly cut on the signal, which can be e.g. the flight-time information measured with the TOF detector or the specific energy loss measured with the TPC. Starting from the detector signals, the particle identification strategy applied in this analysis is the combined particle identification using a Bayesian method [95], which allows to use the combined information from multiple detectors.

Let  $r(s | i)$  be a conditional probability density function to observe in a detector a signal  $s$  if a particle of type  $i$  ( $i = \pi, k, p, e, \mu$ ) is detected. The probability for a particle, if the signal  $s$  is observed to be of type  $i$ , is called the identification weight  $w(i | s)$ . The weights do not only depend on  $r(s | i)$ , but also on how often this type of particle is produced; i.e., it also depends on the *a priori* probability  $C_i$ . The final conditional probability, including the probability factor  $C_i$ , is given by Bayes' formula:

$$w(i | s) = \frac{r(s | i)C_i}{\sum_{j=\pi,k,p,\dots} r(s | j)C_j}. \quad (5.7)$$

The particle identification procedure is performed initially using the detector response and a set of values  $r(s | i)$  is assigned to each track. Then, the relative concentration of particle species ( $C_i$ ) is estimated iteratively.

**Combined particle identification** The advantage of using probabilities is that the probabilities from different detectors, also without a Gaussian response, can be combined simply by multiplying them. The Bayesian particle identification method can be extended to a system of  $N$  contributing detectors.

$$R(\bar{s} | i) = \prod_{j=1}^N r(s_j | i), \quad (5.8)$$

To do so, the combined identification weights  $W(i | \bar{s})$  are written in a

form similar to that of 5.7:

$$W(i | \bar{s}) = \frac{R(\bar{s} | i)C_i}{\sum_{j=\pi,k,p\dots} R(\bar{s} | j)C_j}, \quad (5.9)$$

where

$$\bar{s} = s_1, s_2, \dots, s_N \quad (5.10)$$

is the signal in detectors 1 through  $N$ ,  $C_i$  are the a priori probabilities for a particle to be of type  $i$  and  $R(\bar{s} | i)$  are the combined response functions of the whole system of detectors.

### Purity and efficiency

In ALICE most of the kaons are identified by means of a combined TPC and TOF signal with a Bayesian approach. However, particles traversing the TPC do not necessarily reach the TOF (e.g. they can be absorbed by the TRD), or tracks in the TPC may not (satisfactorily) match a TOF track. In case of a TPC-TOF mismatch, which occurs more frequently at low  $p_T$  ( $p_T < 1.5$  GeV/ $c$ ), the TOF is excluded from the identification process, and the PID relies solely on the TPC signal.

The Bayesian PID provides a probability  $W(i | \bar{s})$  of a track belonging to a certain particle species. For a track to be selected as a kaon, one must set a certain threshold value  $P$ , which determines if a particle is accepted as a kaon or not:

$$\text{kaon ?} \begin{cases} \text{true} & \text{if } W(i | \bar{s}) \geq P; \\ \text{false} & \text{if } W(i | \bar{s}) < P. \end{cases} \quad (5.11)$$

The value of the threshold probability  $P$  determines both the purity and efficiency of the particle identification procedure. Figure 5.2 shows the kaon efficiency and purity as a function of the transverse momentum for several probability thresholds  $P$  for the 10-20% centrality class. These values are obtained for Pb–Pb data by computing a Bayesian fit: for each track the TOF and TPC signals are weighted by the Bayesian probability for all

## 5.2 $\phi$ -meson reconstruction

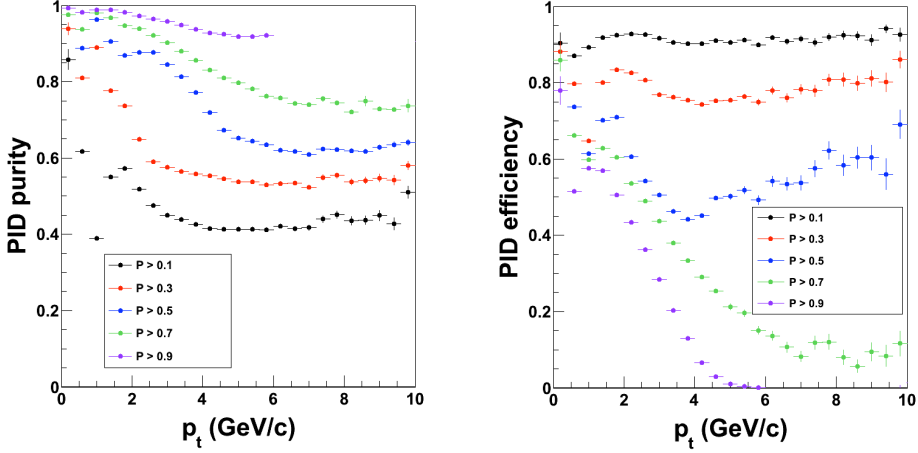


Figure 5.2: Kaon purity (left panel) and efficiency (right panel) for different Bayesian probability thresholds  $P$ . Figure taken from [96]

species to determine the most probable contributions of all the individual species (the sum of which equals the total signal). In this way background and signal yield can be determined, from which one can calculate the purity and efficiency. For the  $\phi$ -meson analysis the kaon sample does not need to have a very high purity, because hadron contamination will be subtracted later by the combinatorial background estimation. Therefore the default probability threshold is set at  $P = 0.3$  in order not to reduce too much the kaon efficiency. However other probability values have been tested as well for the systematic uncertainty estimation.

### 5.2.3 Combinatorial background estimation

To extract the yields of  $\phi$ -mesons in each  $p_T$  and centrality bin, the following procedure is used. The invariant mass distribution of unlike-charge kaon pairs is computed. A cut is performed on  $\eta$  for the reconstructed candidate pairs at  $|\eta| < 0.8$  to reduce the combinatorial background, since the same

kinematic constraints is placed at the level of the kaon selection (see table 5.1). However, most of the kaons that are used to construct the invariant mass spectrum are produced in processes other than  $\phi$ -meson decay. The combinatorial background in the  $\phi$  invariant mass distribution is estimated and subtracted from the unlike-charge distribution in two steps: the combinatorial background estimation and residual background approximation.

The first consists of building invariant mass spectra of like-sign pairs of kaons from the same event. The like-sign kaon spectrum is expected to have a shape similar to that of the unlike-sign kaon spectrum, with the exception of the  $\phi$ -meson contribution. The combinatorial background has been evaluated using the total like-sign kaon pairs ( $n^{--} + n^{++}$ ) in each  $p_T$  and centrality interval, where  $n^{--}(n^{++})$  is the number of  $K^-K^-$  ( $K^+K^+$ ) pairs in the bin. The like-sign background  $m_{inv}$  distribution is normalized to the corresponding distribution of unlike-sign pairs in the region above the  $\phi$ -meson mass ( $1.04 < m_{inv} < 1.08$  GeV/ $c^2$ ), where most of the combinatorial background is located.

After this subtraction, a residual background is still observed, requiring an additional fit of the residual background in order to extract the  $\phi$ -meson signal.

### Residual background approximation

The shape of the residual background is estimated by fitting the invariant mass distribution (combinatorial background subtracted) with a polynomial function. The fit consists of two steps, initially only the residual background is approximated by fitting with a  $2^{nd}$ -order polynomial the mass distribution in regions surrounding the  $\phi$ -meson peak. Using the parameters of the background fit obtained in the first step, the invariant mass spectrum is fitted again using a combined function used to fit both the background and the  $\phi$ -meson peak in order to have a full and stable description of the total invariant mass distribution. This function is the sum of a  $2^{nd}$ -order polynomial and a Breit-Wigner function (the Breit-Wigner will be explained and described in detail in the next subsection).

## 5.2 $\phi$ -meson reconstruction

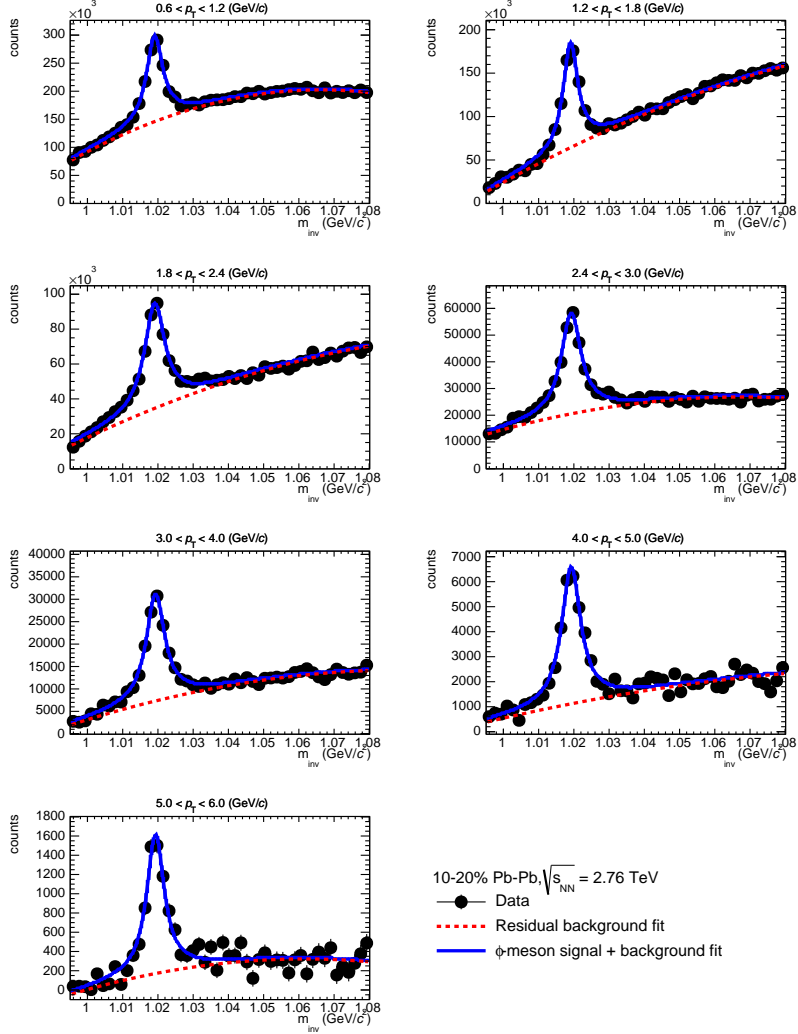


Figure 5.3: Invariant mass distribution after the combinatorial background subtraction in the 10-20% centrality class. The full invariant mass is fitted with the combination of the residual background function (red line) plus a Breit-Wigner used to describe the  $\phi$ -meson peak (blue solid line).

The combined fit is reported for the 10-20% centrality class in Fig. 5.3 for  $0.6 < p_T < 6.0$  GeV/ $c$  where the final invariant mass fit is shown by the blue solid line. The final signal extraction of the  $\phi$ -meson yield as a function of the invariant mass is finally obtained after the subtraction of the second polynomial background approximation shown in the figures as the red dashed line. The amount of residual background decreases with increasing  $p_T$  and from the most central to more peripheral events where fewer kaon are produced.

The  $\phi$ -meson reconstruction has been performed in the centrality range between 10-60%, because for the 10% most central Pb-Pb collisions, the extraction of the signal over the large combinatorial background resulted in too large uncertainties.

### 5.2.4 Signal extraction

Subtraction of residual background finally gives the  $\phi$  spectrum as a function of invariant mass as plotted in Fig. 5.4 for the 10-20% centrality range for several  $p_T$  bins used in the analysis. The  $\phi$ -meson peak is then fitted again with a Breit-Wigner distribution (blue solid line).

The Breit-Wigner is a well known function used for resonance particles and it is defined as:

$$f(E) = \frac{k}{(E - \mu)^2 + (\frac{\Gamma}{2})^2}, \quad (5.12)$$

where  $\mu$  represent the mass of the resonance and  $\Gamma$  its decay width, a quantity inversely proportional to the lifetime  $\tau$  of a resonance. The factor  $k$  is a constant proportional to the raw yield in a given analysis sample.

To verify the  $\phi$ -meson reconstruction, the mass  $\mu$  and the decay width  $\Gamma$  are extracted from the invariant mass fit. Those parameters are reported for all the centrality classes used in this analysis as a function of the transverse momentum of the reconstructed  $\phi$ -meson in Fig. 5.5, together with the PDG values, represented by the dashed grey line.

## 5.2 $\phi$ -meson reconstruction

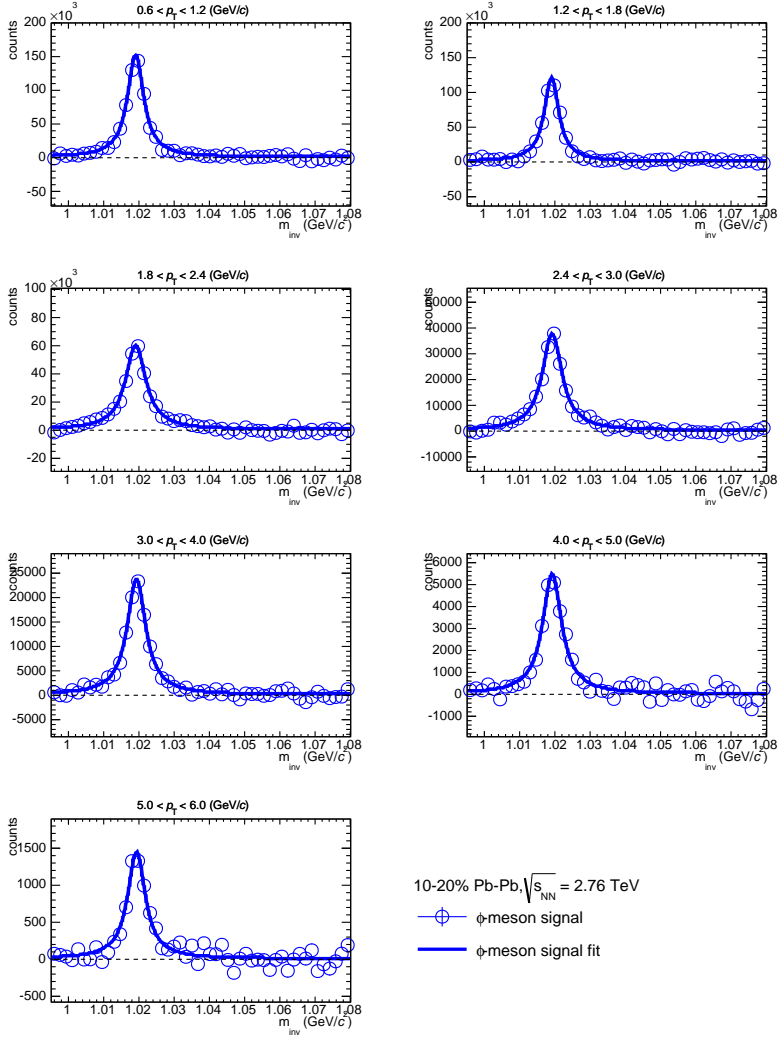


Figure 5.4:  $\phi$ -meson signal invariant mass distribution, after residual background subtraction, together with the final Breit-Wigner fit are shown for different  $p_T$  interval in the 10-20% centrality class.

## 5. Elliptic flow of $\phi$ -mesons

The statistical uncertainties on the mass and width are the statistical uncertainties of the fit parameters. In the left panel the reconstructed mass values are reported and they are observed to be slightly lower than the PDG value at very low  $p_T$  and become compatible at higher  $p_T$  for all the centrality classes. This bias on the reconstructed mass at low  $p_T$  is a detector effect [97] that could be corrected with the usage of a MC simulation in which this slight mass shift is well reproduced. For our elliptic flow analysis no effect is observed due to this mass shift, which will be discussed in the section dedicated to the systematic uncertainty estimation. The width of the  $\phi$  peak is found to be systematically larger than the expected PDG value. This is expected because the Breit-Wigner function takes into account the detector resolution that degrades the mass peak resolution, resulting in an overestimation of the decay width of the  $\phi$ -meson. This effect has been investigated using a Voigtian function to fit the  $\phi$ -meson peak.

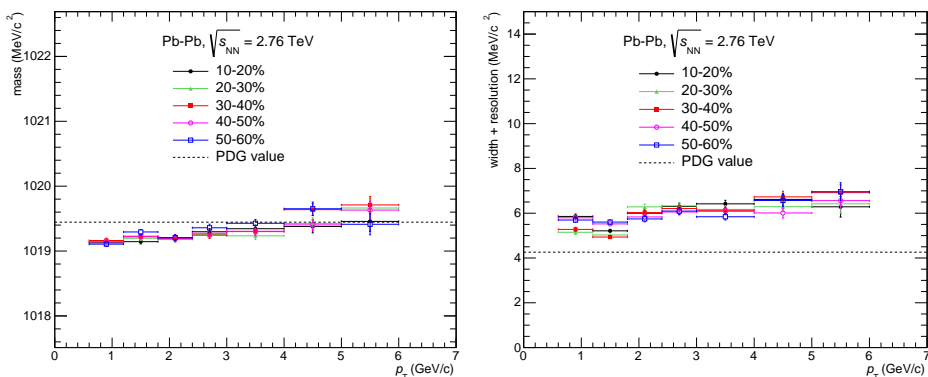


Figure 5.5: Measured  $\phi$ -meson mass (left panel) and width (right panel) as a function of  $p_T$  in Pb–Pb collisions for different centrality classes.

After the fit, the ratios of the  $\phi$ -meson and background invariant mass spectra over the total number of pairs as a function of the invariant mass, a necessary ingredient for the invariant mass fit method, are determined. The ratios and their fits are shown in Fig. 5.6, where the blue markers and line correspond to the ratio of background over total pairs and the corresponding

## 5.2 $\phi$ -meson reconstruction

fitting function, while the green markers and line correspond to the ratio of the  $\phi$ -meson signal over the total pairs and the corresponding fit.

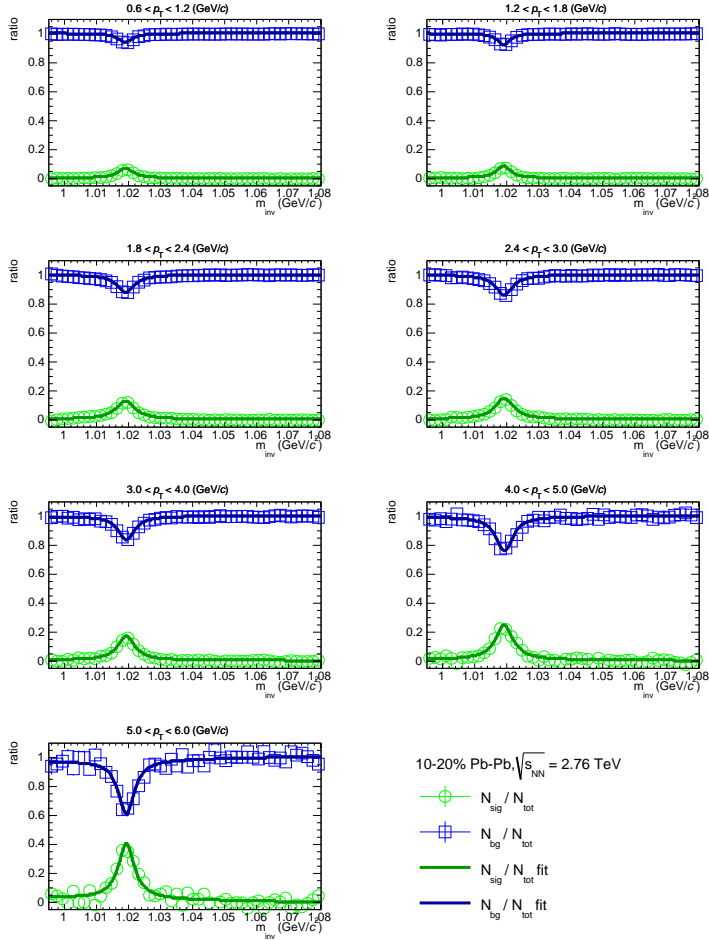


Figure 5.6: Ratios of the  $\phi$ -meson and background spectra on their fits for the different  $p_T$  bins in the 10-20% centrality interval. See text for more information.

## 5. Elliptic flow of $\phi$ -mesons

---

Both the distribution are fitted with the sum of a Breit-Wigner and a linear function. The mass and the decay width of the Breit-Wigner functions are fixed to the value extracted from the signal extraction fit. The  $\phi$ -meson signal over total signal ratio shows a clear  $p_T$  dependence: the higher the transverse momentum, the larger the contribution from  $\phi$ -mesons. The ratios are also showing a centrality dependence, at a given  $p_T$  bin for more peripheral collision a larger significance of the  $\phi$ -meson is observed.

### The Voigtian distribution

To account for limited detector resolution, the Breit-Wigner distribution is convoluted with a Gaussian distribution, where the  $\sigma$  of the Gaussian distribution approximates the detector resolution. The Voigtian distribution cannot be expressed in an analytic form, however a numerical evaluation can be performed in the following way:

$$V(E, \Gamma, \sigma, \mu) = \Re \left( \frac{w \left( \frac{1}{\sqrt{2}\sigma} [E - \mu] + \frac{1}{2\Gamma} \right)}{\sigma \sqrt{2\pi}} \right), \quad (5.13)$$

where  $w(x)$  is the complex error function (or Faddeeva function),

$$w(x) = e^{-x^2} \operatorname{erfc}(-ix) \quad (5.14)$$

with

$$\operatorname{erfc}(x) = \frac{2}{\sqrt{\pi}} \int_x^\infty e^{-t^2} dt. \quad (5.15)$$

The parameters  $\mu$  and  $\Gamma$  are the mass and the decay width of the  $\phi$ -meson, while  $\sigma$  is the width of the Gaussian distribution, a parameter that takes into account the detector resolution. A comparison between the fit parameters extracted previously with the Breit-Wigner function and the ones extracted from a Voigtian fit is shown for two different centrality ranges in Fig. 5.7. In the upper-left panel the mass of the  $\phi$ -meson is reported and no difference is observed in the mass value estimated from the two different

## 5.2 $\phi$ -meson reconstruction

fitting function, in the upper right the parameter related to the width of the peak (decay width and detector resolution) are plotted. When the Voigtian function is used the decay width extracted from the fit is observed to be compatible with the PDG value within the statistical errors. The additional parameter representing the detector resolution extracted from the fit is observed to slightly increase as a function of the transverse momentum from a value of  $\sim 0.0015$  GeV/ $c$  up to a value of  $\sim 0.002$  (GeV/ $c$ ).

Even if the Voigtian function reproduces the PDG value of the  $\phi$ -meson decay width, it is a less stable fit with respect to the Breit-Wigner, which has therefore been used as the default function. However the Voigtian fit was used for the systematic uncertainty estimation.

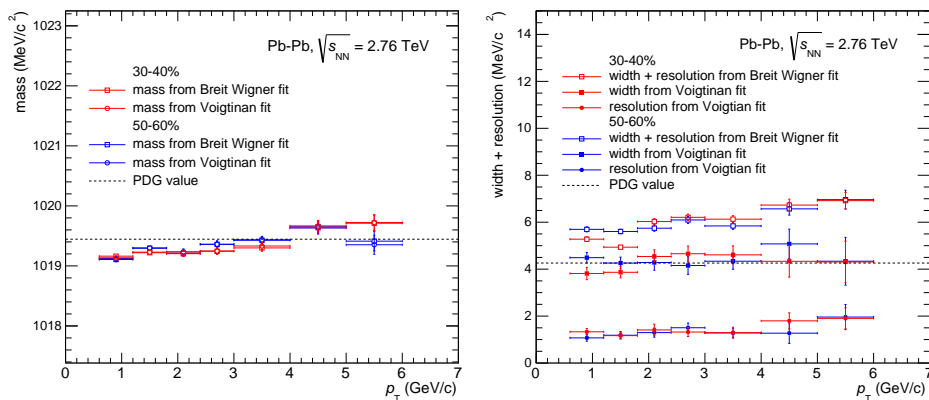


Figure 5.7: Comparison of the measured  $\phi$ -meson mass (left panel) and width (right panel) as a function of  $p_T$  using both Breit-Wigner and Voigtian functions. In the right panel the resolution parameter extracted from the Voigtian fit is reported as well. Measurements are reported as illustration for the 30-40% and 50-60% centrality classes for Pb-Pb collisions.

### 5.3 Invariant mass fit method and $v_2^\phi(p_T)$

Equation 5.4 shows the decomposition of  $v_2^{pair}(m_{inv})$  in terms of background and signal over the total pairs ratios, and it is then parameterized with the following fitting function:

$$v_2^{pair}(m_{inv}) = \left( \alpha + \beta m_{inv} + \frac{\xi}{(m_{inv} - \mu)^2 + (\frac{\Gamma}{2})^2} \right) v_2^\phi(p_T) \quad (5.16)$$

$$+ \left( \gamma + \delta m_{inv} + \frac{\varsigma}{(m_{inv} - \mu)^2 + (\frac{\Gamma}{2})^2} \right) (\epsilon + \zeta m_{inv} + \eta m_{inv}^2)$$

where most of the parameters are set to the values extracted by fitting the measured signal and background over total ratios. The background flow  $v_2^{bg}(m_{inv})$  is assumed to be a 2<sup>nd</sup>-order polynomial. The  $v_2^\phi(p_T)$  is the free parameter of the fitting function that we want to obtain.

The three sub-events scalar product method using the VZERO detectors (section 3.2.1) has been used for the  $v_2^{pair}(m_{inv})$  measurement. This method has the advantage of using a large eta gap ( $|\Delta\eta| > 0.9$ ) to suppress non-flow contributions. The measured  $v_2^{pair}(m_{inv})$  is reported in Fig. 5.8 for the 10-20% centrality class. In this figure one can see in the mass region, in which the  $\phi$ -meson mass peak is located, a depletion in the  $v_2^{pair}(m_{inv})$  distributions. The amplitude of this depletion represent the  $v_2^\phi$  in a particular  $p_T$  interval. In the figures also the fitting functions, from which the  $v_2^\phi(p_T)$  is extracted, are reported.

In Fig. 5.9 a complete picture of the centrality evolution of the  $p_T$  differential  $v_2^\phi$  measured with the three sub-event scalar product method using the VZERO detectors is shown. A clear centrality dependence of the elliptic flow coefficient of the  $\phi$ -meson is observed, consistent with the picture in which the final state anisotropy is driven by the geometry of the collision. The magnitude of  $v_2^\phi$  progressively increases from central to peripheral collisions up to the 30-40% centrality interval.

### 5.3 Invariant mass fit method and $v_2^\phi(p_T)$

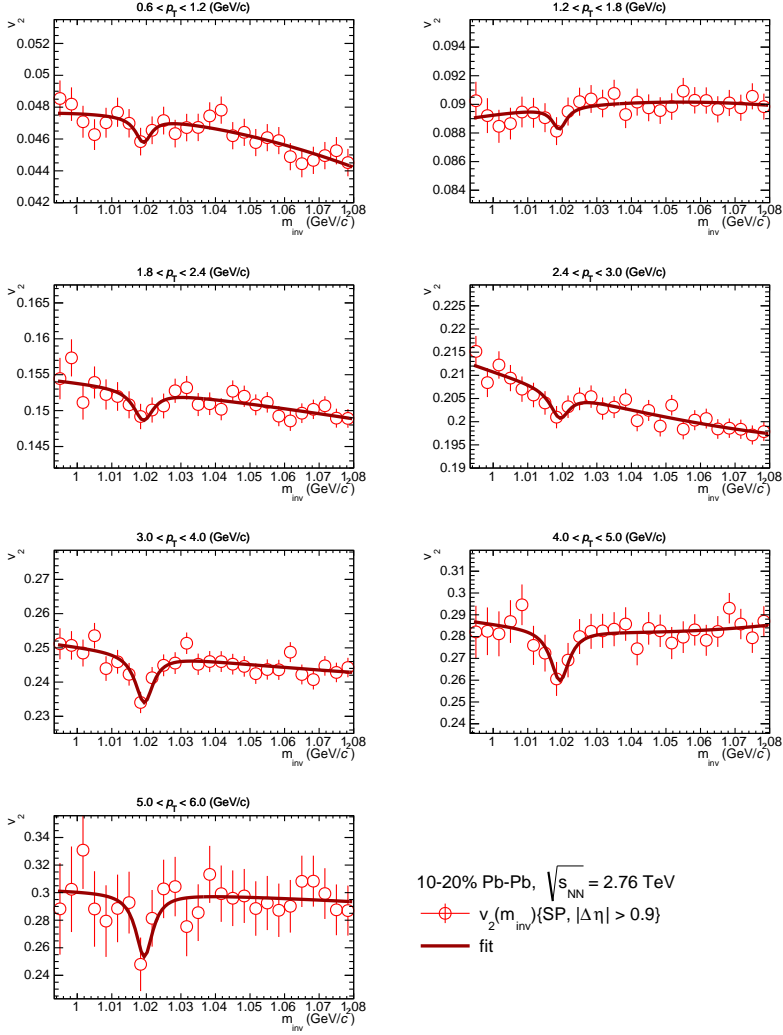


Figure 5.8: Measured  $v_2^{pairs}(m_{inv})$  using the scalar product method for different  $p_T$  bin in the 10-20% centrality class together with the fitting function from which the  $v_2^\phi(p_T)$  is extracted.

## 5. Elliptic flow of $\phi$ -mesons

For the 40-50% and 50-60% centrality classes, the magnitude of  $\phi$ -meson  $v_2$  does not change significantly within the systematic uncertainties compared to the previous centrality interval. This can be due to the combination of two effects, a larger initial spatial geometrical anisotropy combined with less interactions between the constituents in the system due to the smaller system size.

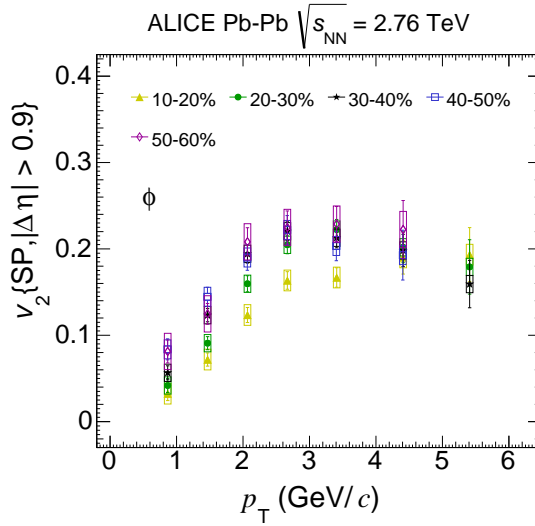


Figure 5.9: The  $p_T$ -differential  $v_2$  of the  $\phi$ -meson measured in different centralities of Pb-Pb collision at  $\sqrt{s_{NN}} = 2.76$  TeV.

### 5.4 Systematic studies on $\phi$ -meson $v_2$

In this section the evaluation of the different component of the systematic uncertainties for the elliptic flow of the  $\phi$ -meson are explained.

For each different component a systematic uncertainty, reported in the following as relative value, is estimated and the total systematic uncertainty

## 5.4 Systematic studies on $\phi$ -meson $v_2$

---

for the  $\phi$ -meson  $v_2$  is evaluated by adding them in quadrature. The systematic checks have been done for all the centrality classes and no centrality dependence has been observed.

**Track and identification cuts** One of the most important selections is on the  $DCA_{x,y}$  that allows to remove secondary kaons from our track sample. For the default analysis the  $p_T$  dependent cut reported in equation 5.6 has been used, however also a less stringent and  $p_T$  independent cut placed at 0.3 cm was used. No systematic difference has been observed between those two cuts. Also other tracking cuts, such as the number of TPC clusters and the  $\chi^2$  per TPC point have been varied, and also in this case no systematic difference has been observed. As for the kaon identification, the value of the Bayesian probability threshold  $P$  has been varied. It is seen that if the probably threshold is larger then 0.7, that despite the very high kaon purity achieved, the reconstruction efficiency for the kaons is too low, resulting in an elliptic flow of the  $\phi$ -meson with very large statistical uncertainties, in particular for the high  $p_T$  region. For this reason values larger the 0.6 have not been used for the systematic uncertainty estimation. The maximum variation observed and assigned as systematic uncertainty is in the range of 5-15%.

**Reference particle selection** The first step of the calibration of the VZEROA(C) detectors is the gain equalization. The default procedure consists of equalizing the signal in the eight detector rings (4 per side). A slightly different approach to calibrate the VZEROA(C) detectors, which is to equalize the signal in each ring separately, because the mean multiplicity in the rings could vary. An additional source of systematics is that in some runs the VZERO signals were saturated, and those runs were removed to investigate this effect. The uncertainties evaluated by those studies were observed to be small, resulting in a maximum variation of 5%.

**Signal and background extraction** An additional and important component of the systematic studies is the variation of the procedure used for the

combinatorial and residual background subtraction and for the  $\phi$ -meson signal extraction. Different techniques to estimate combinatorial background, like-sign with a geometrical mean ( $2\sqrt{n^{--}n^{++}}$ ) and event-mixing, have been used. The latter consists of building unlike-sign kaon pairs from different events. The background function used to describe the residual background and the  $v_2^{bg}(m_{inv})$  in the invariant mass fit method has been varied in both the fitting routine simultaneously with a  $3^{rd}$ -order polynomial. For the  $\phi$ -meson signal extraction, the systematic uncertainties were further investigated varying the fitting function for the signal extraction with the Voigtian function. Because of the bias in the measured mass of the  $\phi$  meson, as a systematic check the  $\phi$ -meson mass has been fixed to the PDG value in the analysis, and no systematic difference is observed for  $v_2^\phi(p_T)$ . Finally, also the fitting range used for the background and signal extraction, as well as for the fit of the  $v_2^{pair}(m_{inv})$ , has been varied. Due to the presence of a large combinatorial background, the systematic uncertainties are estimated to be 10% for more central events, while for more peripheral collisions a 5% systematic error has been assigned.

**Event selection** The event sample has been varied by changing the cut value on the position of the primary vertex (11, 9, 7 cm) along the beam axis ( $V_z$ ) and changing the centrality selection criteria from the signal amplitudes of the VZERO scintillator to the stand-alone TPC multiplicity. The resulting  $v_2$  is observed to be fully consistent with the default measurements for the whole transverse momentum region, and therefore no systematic uncertainties has been assigned for this.

## 5.5 Results and discussion

In the next part of this chapter the  $v_2^\phi(p_T)$  is compared with the elliptic flow measurements for identified mesons ( $\pi^\pm$ ,  $K^\pm$ ,  $K^0$ ) and baryons ( $p$ ,  $\Lambda$ ,  $\Xi^-$ ,  $\Omega^-$ , and their antiparticles) [82].

The characteristics mass ordering of the  $v_2(p_T)$ , the number of constituent quarks (NCQ) scaling, that was argued to work well at RHIC en-

## 5.5 Results and discussion

---

ergies [98, 99] and the comparison with theoretical model calculation are discussed in detail in the following sections.

### 5.5.1 Comparison with other particle species

Figure 5.10 shows the  $p_T$ -differential  $v_2$  for all identified particles measured in Pb–Pb collisions at  $\sqrt{s_{NN}} = 2.76$  TeV by ALICE. Each panel corresponds to a different event centrality class, illustrating how  $v_2(p_T)$  develops for different particle species within the same centrality interval. The panels are arranged such that the top left starts with the most central collisions and that we show more peripheral collisions when moving from left to right and from top to bottom. For the reconstruction of the decay particles the following decay channel were used:  $K^0 \rightarrow \pi^+ + \pi^-$ ,  $\Lambda \rightarrow p + \pi^-$ ,  $(\bar{\Lambda} \rightarrow \bar{p} + \pi^+)$ ,  $\Xi^- \rightarrow \Lambda + \pi^-$ ,  $(\bar{\Xi}^+ \rightarrow \bar{\Lambda} + \pi^+)$  and  $\Omega^- \rightarrow \Lambda + K^-$  ( $\bar{\Omega}^+ \rightarrow \bar{\Lambda} + K^+$ ). The error bars correspond to statistical uncertainties, while boxes indicate the systematic uncertainties on the measurements.

When comparing all particle species, a clear mass ordering is seen for all centrality classes in the low  $p_T$  region (i.e.  $p_T < 3$  GeV/ $c$ ) attributed to the interplay between elliptic and radial flow [100, 101]. Due to the radial expansion a mass dependent shift towards higher momenta occurs for all particles participating in the collective expansion. Particles are boosted to higher velocity, which for heavier particle means they will be measured at higher momenta than lighter particles. For higher values of  $p_T$  ( $p_T > 3$  GeV/ $c$ ), particles tend to group according to their type, i.e. mesons and baryons. The  $\phi$ -meson is of particular interest since its mass is close to that of  $p$  and  $\Lambda$  baryons. It provides an excellent test of both the observed mass ordering and the baryon-meson grouping at low and intermediate  $p_T$ , respectively.

The  $v_2$  of the  $\phi$ -meson for  $p_T < 3$  GeV/ $c$  follows the mass hierarchy. However, for the lowest  $p_T$  bin, there is an indication that the  $\phi$ -meson  $v_2$  is larger the proton  $v_2$ , indicating a possible breaking in the mass hierarchy. At higher  $p_T$  the elliptic flow of the  $\phi$ -meson appears to follow, within uncertainties, the band of baryons for central events. For peripheral collisions, the  $v_2$  values of the  $\phi$ -meson shift progressively to the band of mesons. This is consistent with the observation that the  $(p+\bar{p})/\phi$  ratio, calculated from

## 5. Elliptic flow of $\phi$ -mesons

the transverse momentum spectra, is almost constant as a function of  $p_T$  in central Pb–Pb events, while for peripheral collisions the ratio decreases with increasing  $p_T$ , as reported in [97].

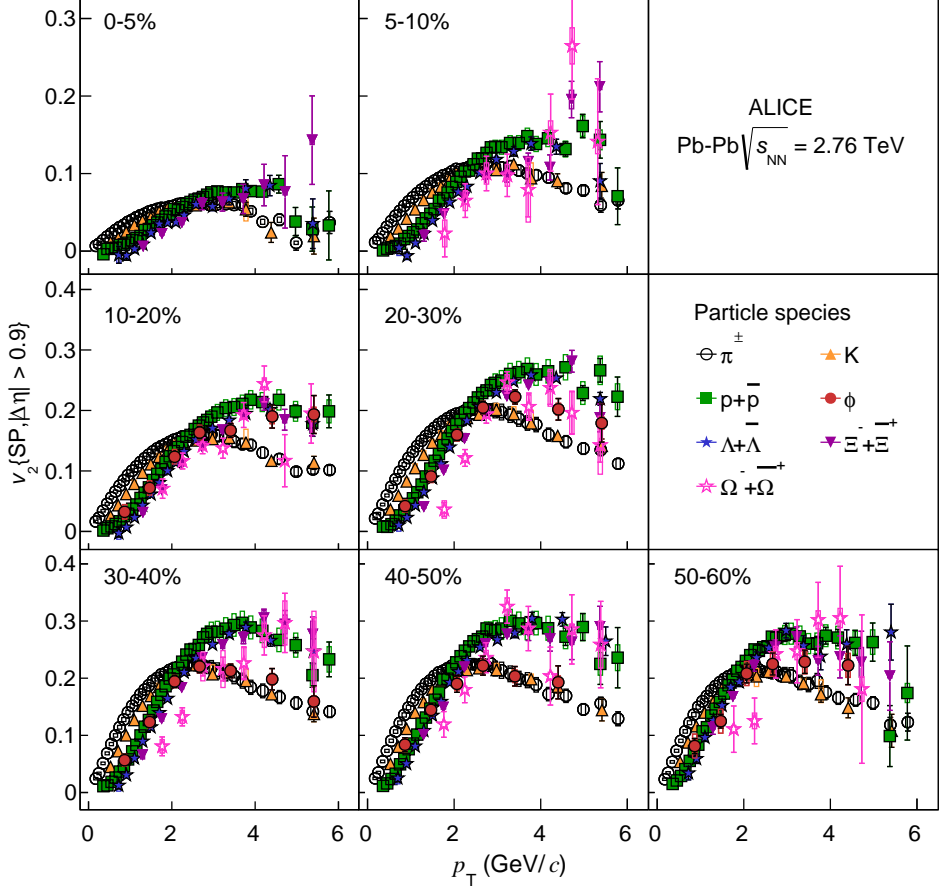


Figure 5.10: The  $p_T$ -differential  $v_2$  for different particle species grouped by centrality class of Pb-Pb collisions at  $\sqrt{s_{NN}} = 2.76$  TeV.

## 5.5 Results and discussion

---

### 5.5.2 The meson-baryon scaling at LHC

One of the experimental observations reported at RHIC is that at intermediate values of transverse momentum, the  $v_2$  depends on the number of constituent quarks i.e. baryons and mesons. It was also observed that if both  $v_2$  and  $p_T$  are scaled by the number of constituent quarks ( $n_q$ ), all the identified hadron species approximately follow a single function. The scaling was extended to the lower  $p_T$  region by plotting the elliptic flow as a function of the transverse kinetic energy defined as  $KE_T = m_T - m_0$ , where  $m_T = \sqrt{p_T^2 + m_0^2}$  is the transverse mass. Initially, this representation was observed to work well at RHIC energies [98, 99]. However, more precise measurements show deviations from this scaling for Au-Au collisions [102].

To test the scaling properties, the  $v_2/n_q$  is shown as a function of  $p_T/n_q$  in Fig. 5.11 for 10-20% (left panel) and 40-50% (right panel). In the intermediate transverse momentum region (i.e.  $3 < p_T < 6$  GeV/c or for  $p_T/n_q > 1$  GeV/c) the measurements at the LHC indicate that the scaling is only approximate. The magnitude of the observed deviations seems to be similar for all centrality intervals. To quantify the deviation, the  $v_2/n_q$  for  $p(\bar{p})$  as a function of  $p_T/n_q$  is fitted with a polynomial function and the ratio of  $(v_2/n_q)/(v_2/n_q)_{Fit-p}$  for each particle species is computed. The corresponding  $p_T/n_q$  dependence of this double ratio is presented in Fig. 5.12 for the 10-20% (left panel) and 40-50% (right panel) centrality intervals. Figure 5.12 shows that for  $p_T/n_q > 1$  GeV/c the data points exhibit deviations from the scaling at the level of  $\pm 20\%$  with respect to the reference ratio for all centrality intervals.

Figure 5.13 shows the  $(m_T - m_0)/n_q$  dependence of  $v_2/n_q$ . Once more the ratio with a parameterization of the proton measurements is computed for all the other particle species. In Fig. 5.14 the 10-20% and 40-50% centrality classes are shown in the left and right panel respectively. In this representation the data shows significant deviations for  $(m_T - m_0)/n_q < 0.5$  GeV/c<sup>2</sup>. For the intermediate region the scaling is approximate for all centrality intervals, while for higher  $p_T$  there are deviations at the level of  $\pm 20\%$  with respect to the reference ratio for all centrality intervals.

## 5. Elliptic flow of $\phi$ -mesons

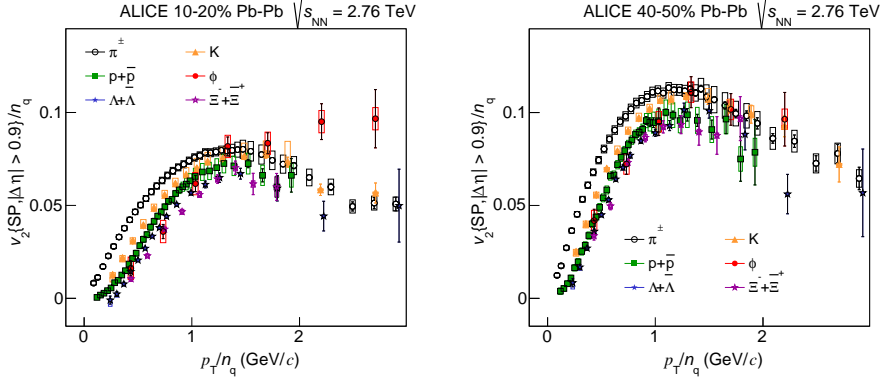


Figure 5.11: The  $p_T/n_q$  dependence of  $v_2/n_q$  for different hadron species for Pb–Pb collisions for the 10-20% (left) and 40-50% (right) centrality intervals at  $\sqrt{s_{NN}} = 2.76$  TeV.

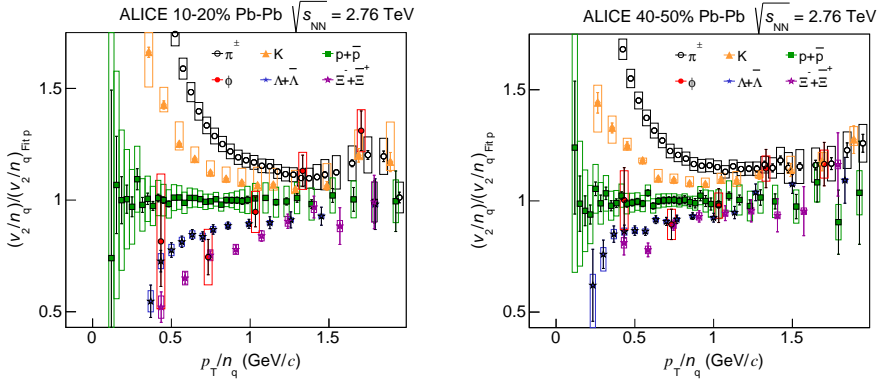


Figure 5.12: The  $p_T/n_q$  dependence of the double ratio of  $v_2/n_q$  for every particle species relative to a fit to  $v_2/n_q$  of  $p$  and  $\bar{p}$  (see text for details) 10-20% (left) and 40-50% (right) Pb–Pb collisions at  $\sqrt{s_{NN}} = 2.76$  TeV.

## 5.5 Results and discussion

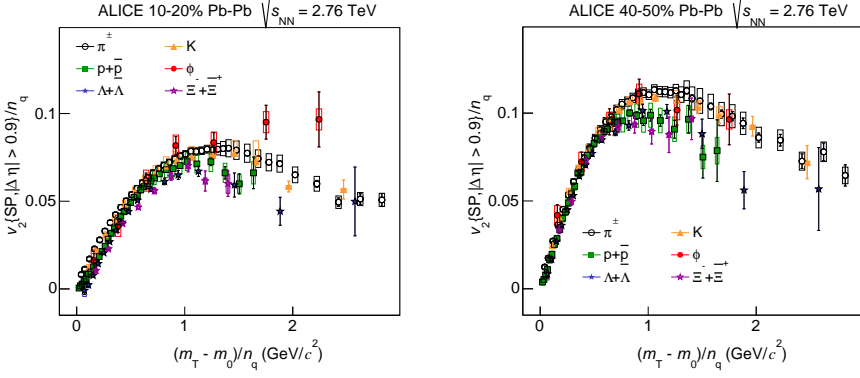


Figure 5.13: The  $(m_T - m_0)/n_q$  dependence of  $v_2/n_q$  for different hadron species for Pb–Pb collisions for the 10-20% (left) and 40-50% (right) centrality intervals at  $\sqrt{s_{NN}} = 2.76$  TeV.

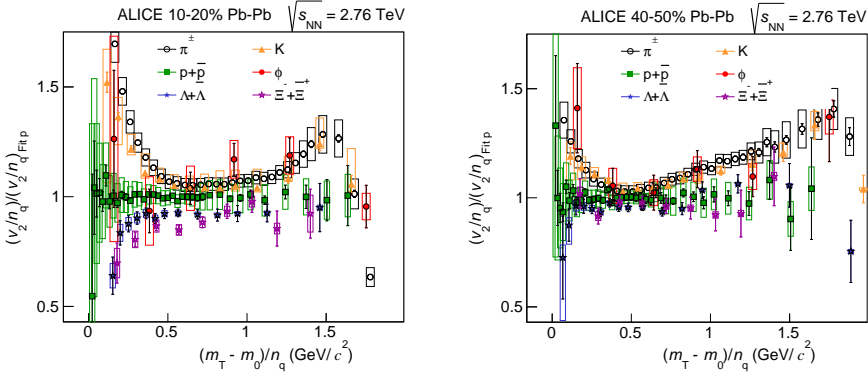


Figure 5.14: The  $(m_T - m_0)/n_q$  dependence of the double ratio of  $v_2/n_q$  for every particle species relative to a fit to  $v_2/n_q$  of  $p$  and  $\bar{p}$  (see text for details) 10-20% (left) and 40-50% (right) Pb–Pb collisions at  $\sqrt{s_{NN}} = 2.76$  TeV.

### 5.5.3 Comparison with hydrodynamical model

The measurements of the elliptic flow of identified hadron species at the LHC help testing the validity of some hydrodynamical models.

In this section the  $v_2$  measurements are compared with viscous hydrodynamical calculations with and without a contribution coming from a hadronic cascade afterburner, VISHNU [26] and VISH2+1 [25] respectively. In Fig. 5.15 and Fig. 5.16 the differential elliptic flow of pions, protons and  $\phi$ -mesons is compared for  $p_T < 2$  GeV/ $c$  with the VISH2+1 and VISHNU predictions respectively, for the 10-20% and 40-50% centrality classes.

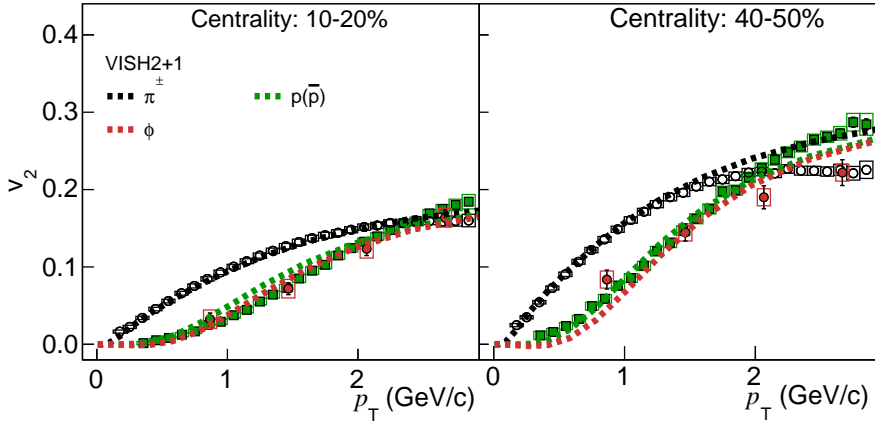


Figure 5.15: The  $p_T$ -differential  $v_2$  for pions, protons and  $\phi$ -mesons, in the 10-20%(left) and 40-50%(right) centrality classes, are compared to pure hydrodynamic model (VISH2+1).

The full hydrodynamic simulations based on VISH2+1 reasonably well describe the pions measurements for  $p_T < 2$  GeV/ $c$  at all collision centralities, while they fail to correctly reproduce the centrality dependence of the proton elliptic flow. For the most central collisions the  $v_2^p(p_T)$  is over-

## 5.5 Results and discussion

---

predicted at small transverse momentum, i.e. the radial flow pushing the elliptic flow to higher  $p_T$  is not strong enough in the model for the most central events. The agreement with the proton measurements gets better in more peripheral collision, indicating an incorrect centrality dependence of the balance between radial and elliptic flow in the VISH2+1 model. This discrepancy changes by using a hybrid model in which viscous hydrodynamics is combined with a hadronic cascade afterburner, however the modification of the  $v_2^p(p_T)$  is so large that VISHNU again fails to describe the protons under-predicting in this case the  $v_2$  measurements. The elliptic flow of pions is equally well described by both model predictions [103].

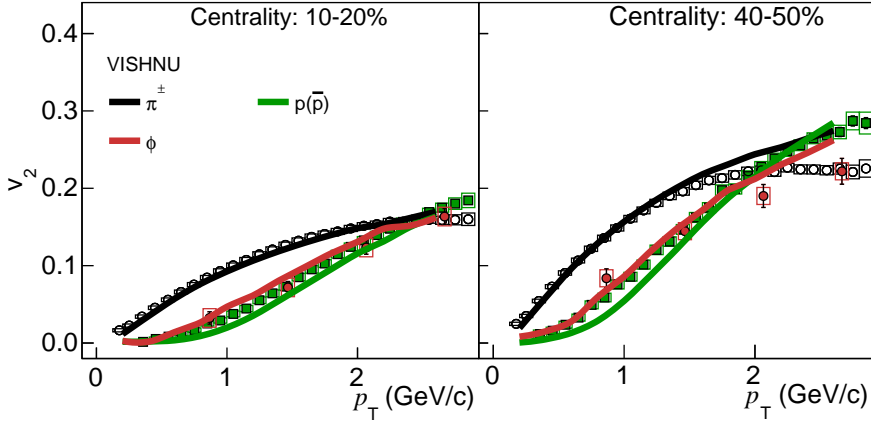


Figure 5.16: The  $p_T$ -differential  $v_2$  for pions, protons and  $\phi$ -mesons, in the 10-20%(left) and 40-50%(right) centrality classes, are compared to hydrodynamic calculation coupled to a hadronic cascade model (VISHNU).

## 5. Elliptic flow of $\phi$ -mesons

When including the  $\phi$  meson in the comparison it is seen that the characteristic mass ordering (observed in data and in VISH2+1) is not preserved anymore. Unfortunately, the uncertainties in the ALICE  $\phi$ -meson measurements are currently too large at low  $p_T$  to better constrain the possible hadronic contribution. Recently a similar observation has been made by the STAR experiment at lower energies [104].

The comparison of the  $\phi$ -meson  $v_2$  measurements with both model predictions is investigated in more detail in Fig. 5.17 and Fig. 5.18.

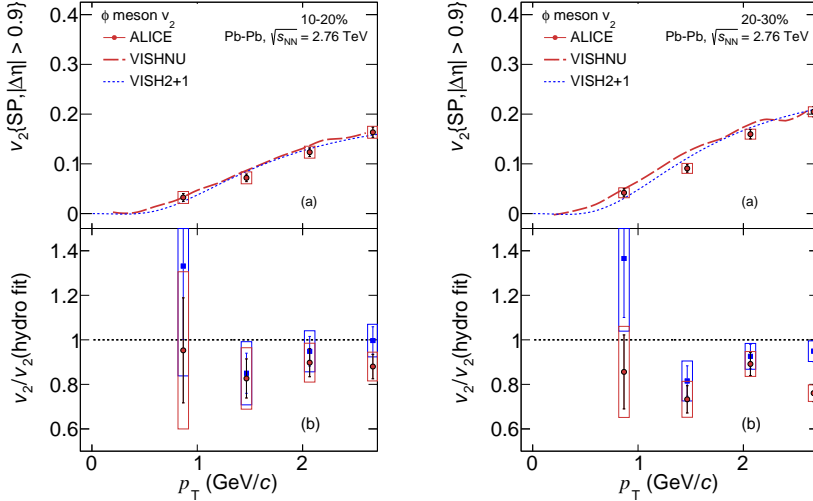


Figure 5.17:  $\phi$ -mesons  $v_2$ , in the 10-20%(left) and 20-30%(right) central-class, is compared in (a) panels to both hydrodynamic calculation VISH2+1 (blue line) and VISHNU (red line). In the lower (b) panels the ratios to the models are reported.

## 5.5 Results and discussion

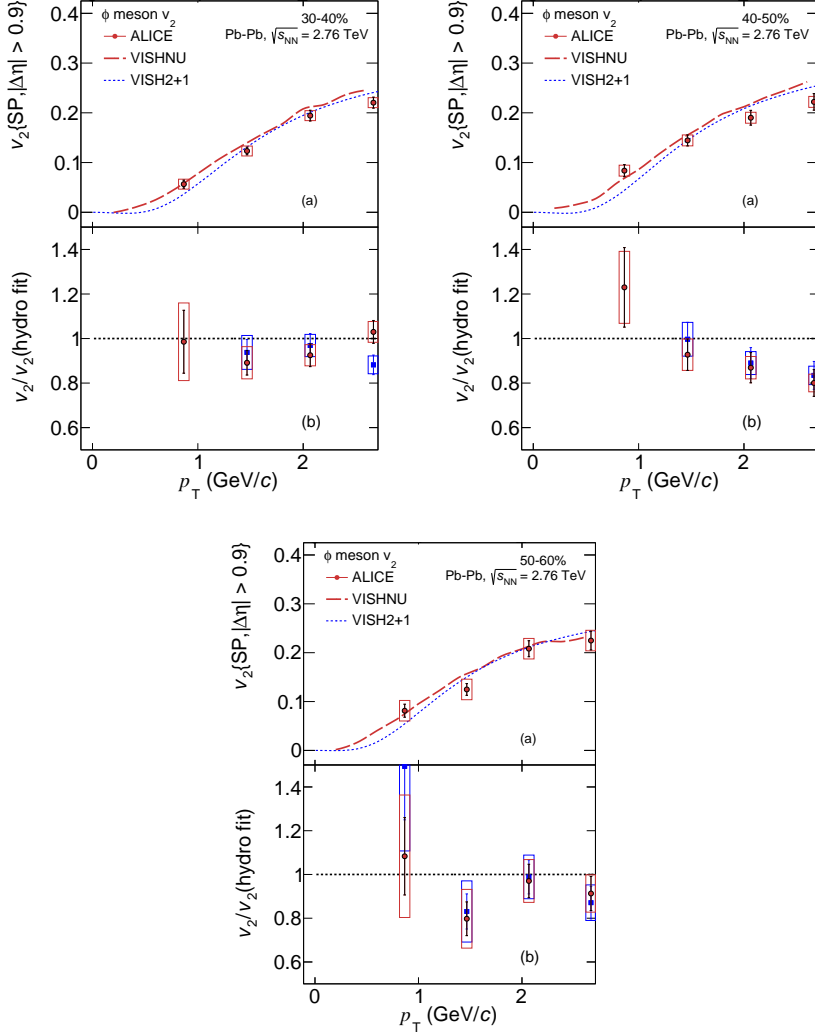


Figure 5.18:  $\phi$ -mesons  $v_2$ , in the 30-40%(upper left) and 40-50%(upper right) and 50-60%(middle low) centrality classes, is compared in (a) panels to both hydrodynamic calculation VISH2+1 (blue line) and VISHNU (red line). In the lower (b) panels the ratios to the models are reported.

## 5. Elliptic flow of $\phi$ -mesons

---

Those figures are organized as follow: in the upper panels, indicated with (a), a comparison with VISHNU (red dashed line) and VISH2+1 (blue dotted line) predictions are presented for all the centrality classes analyzed in this thesis. In the lower (b) panels of the same figures the ratios of the measurement to a fit of the model calculation as a function of the transverse momentum is shown; the colour of the ratios matches the colour of the model prediction. It is observed that VISHNU and VISH2+1 do not differs too much in predicting the  $\phi$ -meson  $v_2$  measurements and both systematically overestimate the measurements for  $p_T > 1$  GeV/ $c$ . For  $p_T < 1$  GeV/ $c$ , where the two models differ more, the large uncertainties of the  $\phi$ -meson  $v_2$  measurements do not currently allow for a stronger constraints on the theoretical model calculations.

---

---

## Chapter 6

# Elliptic flow of heavy-flavour decay electrons

---

---

Heavy quarks, i.e. charm or beauty, are unique probes of the properties of the hot and dense QCD medium, the Quark-Gluon Plasma (QGP). Heavy quarks are produced at the initial stage of the collision, almost exclusively via hard partonic scattering processes. Therefore, they are expected to experience the full evolution of the collision, interacting with the constituents of the QCD medium via both elastic and inelastic processes. At low  $p_T$ , the  $v_2$  coefficient is sensitive to the degree of thermalization of heavy quarks in the deconfined medium. At intermediate  $p_T$ , it is expected to be sensitive to the heavy-quark hadronization via fragmentation in the vacuum and recombination with other quarks from the medium [33]. At high  $p_T$  the measurement of  $v_2$  gives information on the path-length dependence of in-medium parton energy loss. Particles emitted in the direction of the reaction plane have, on average, a shorter in-medium path length than those emitted orthogonally, leading a priori to a larger energy loss in the latter case.

## 6. Elliptic flow of heavy-flavour decay electrons

---

The elliptic flow of electrons from heavy-flavour hadron decays,  $v_2^{e^\pm \leftarrow HF}$ , is obtained from the measurement of the inclusive electron elliptic flow,  $v_2^{e^\pm}$ , by subtracting the elliptic flow of electrons not originated from heavy-flavour hadron decays,  $v_2^{Background}$ , using the  $p_T$  spectra as weights.

The heavy-flavour decay electron  $v_2$  is extracted making use of the additive property of the  $v_2$  coefficient as shown in equation 6.1:

$$v_2^{e^\pm \leftarrow HF} = \frac{(1 + R_{SB})v_2^{e^\pm} - v_2^{Background}}{R_{SB}} \quad (6.1)$$

where  $R_{SB}$  is the signal over background electron ratio and  $(1 + R_{SB})$  is the ratio of the inclusive over background electron yield. The  $v_2^{e^\pm \leftarrow HF}$ , is measured at central rapidity in the 0-10%, 10-20% and 20-40% centrality classes in a  $p_T$  interval between 0.5 and 13 GeV/c in Pb-Pb collisions at  $\sqrt{s_{NN}} = 2.76$  TeV. In the 10-20% and 20-40% centrality interval the EMCal single shower trigger events are used to select electrons for  $p_T > 8$  GeV/c. In 0-10%, due to the large number of events in the 2011 data sample, and because the EMCal trigger cannot be used due to event plane calibration issues, the centrality MB trigger has been used up to  $p_T = 13$  GeV/c. The results are compared to models describing the interactions of heavy quarks and open heavy-flavour hadrons with the high-density medium formed in heavy-ion collisions.

In the next sections the ingredients necessary to measure the elliptic flow of electrons from heavy-flavour hadrons decay will be presented and discussed in detail.

### 6.1 Inclusive electron identification

Electron identification is performed using different strategies according to the transverse momentum region in which the electrons are identified. At low transverse momentum ( $0.5 < p_T < 3$  GeV/c) the electrons are identified using the ITS-TPC-TOF detectors while at higher  $p_T$  ( $3 < p_T < 13$  GeV/c) the TPC and EMCal are used. The EMCal measurements are reported from  $p_T > 1.5$  GeV/c in order to have an overlapping region in  $p_T$  to compare

## 6.1 Inclusive electron identification

---

the electron purity estimated with the two different identification strategies. The electron identification strategy switches at  $p_T = 3 \text{ GeV}/c$  because at high  $p_T$  the TPC-EMCal provides higher electron purity compared to the ITS-TOF-TPC strategy. In the following the two electron identification strategies are explained in detail and the electron purity is discussed.

**Track selection** Electron candidate tracks are required to fulfill several track selection cuts. The selection criteria of primary electron tracks is to have at least 100 reconstructed space points out of the maximum of 159 in the TPC. The average  $\chi^2$  of the track fit per TPC space point was required to be below 3.5. These selections reduce the contribution from short tracks, which are unlikely to originate from the primary vertex, to the analyzed sample. To further reduce the contamination from secondary tracks (i.e. particles originating either from weak decays or from the interaction of other particles with the material), only particles within a maximum distance of closest approach (DCA) to the primary vertex in both the  $xy$ -plane ( $\text{DCA}_{x,y} < 2.4 \text{ cm}$ ) and the  $z$  coordinate ( $\text{DCA}_z < 3.0 \text{ cm}$ ) were accepted. Electron candidates are selected at mid-rapidity  $|y| < 0.8$ , and in case of the EMCal detector the selection is limited by construction to  $|y| < 0.7$ . When the EMCal electron identification is employed, a geometrical matching of the EMCal cluster with the associated track is applied ( $|\Delta\eta| < 0.05$  and  $|\Delta\varphi| < 0.05$ ). A summary of the selection and identification electron requirements is listed in Table 6.1.

### 6.1.1 ITS–TOF–TPC

Electron identification cuts are applied on the so-called number of sigma ( $N\sigma$ ), which is defined as the deviation of the detector signal ( $dE/dx$  for the TPC/ITS and velocity for the TOF) from the expectation, assuming the electron mass, in terms of number of standard deviation  $\sigma$ .

Ideally, an  $N\sigma$  distribution should have a Gaussian shape centred around zero and a width of 1. Although the TPC calibration was already performed on the raw data, in the 2011 data sample it is found that the mean and  $\sigma$  of the TPC- $N\sigma$  distribution of electrons slightly varies with pseudo-rapidity

---

## 6. Elliptic flow of heavy-flavour decay electrons

---

and collision multiplicity. These variations are due to detector effects, like the variation of the occupancy with the event multiplicity or the run-by-run changing detector conditions. The correction factors were determined by a skewed gauss fit of the TPC- $N\sigma$  signal as a function of these variables. The mean and width parameters extracted from the gauss interpolations, are then fitted either with a straight line or with a trigonometric function respectively, that represent the corrections for the  $N\sigma$  distribution in the TPC. After the corrections the residual dependence of the TPC- $N\sigma$  is observed to be about  $\sim 10$  times smaller than the initial one. Nevertheless no significant difference is observed with and without corrections on the electron measurements reported in this work.

In Fig. 6.1 the performance plots for the TPC detector are shown for the 20-40% centrality class in Pb-Pb collision at  $\sqrt{s_{NN}} = 2.76$  TeV. In the top left panel the  $N\sigma$  distribution of the TPC after the quality track cuts is shown. In the low  $p_T$  region ( $p_T < 3$  GeV/c), where the kaon, proton and deuteron bands cross that of the electron in the TPC, the measured time-of-flight in the TOF and the energy loss in the ITS are used to reject the hadron contamination. The usage of both detectors is mandatory because their separation power among hadrons and electrons is more accurate in different momentum regions, see chapter 2 for more details. In the top right panel the TPC- $N\sigma$  distribution is shown after the TOF cut has been applied ( $|\text{TOF-}N\sigma| < 2$ ). However, kaons and protons in the low momentum region are not completely removed after the TOF- $N\sigma$  cut due to wrong associated hits in the TOF detector. This source of contamination is further suppressed applying a cut in the ITS- $N\sigma$ ; electrons are identified selecting tracks with  $|\text{ITS-}N\sigma| < 1$  for  $p_T < 1.5$  GeV/c, while for higher  $p_T$  the cut has been relaxed ( $|\text{ITS-}N\sigma| < 2$ ) since there the separation power in the ITS is lower. In the lower panel of Fig. 6.1 the  $N\sigma$  distribution of the TPC is shown after that the additional electron identification in the ITS has been applied.

The electron signal is extracted from the TPC detector selecting tracks that have a TPC- $N\sigma$  between -1 and 3 for  $p_T < 1.5$  GeV/c and between 0 and 3 for  $p_T \geq 1.5$  GeV/c due to the large pion contamination in the TPC detector.

## 6.1 Inclusive electron identification

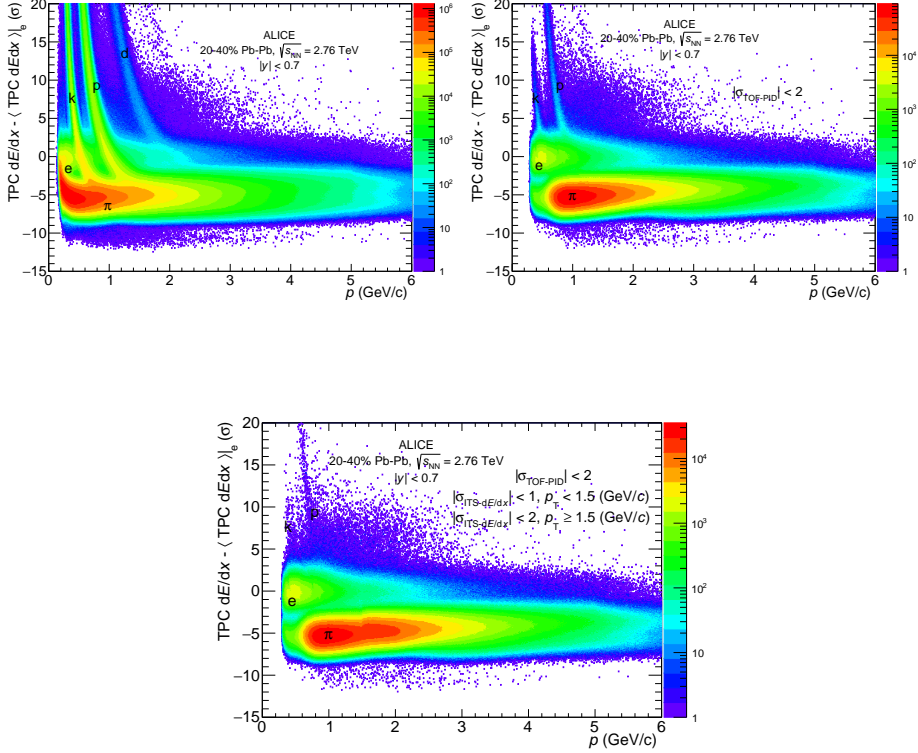


Figure 6.1: In the top right panel the TPC- $N\sigma$  distribution as a function of the momentum is shown after the single track cuts are applied. In the top right panel the TPC- $N\sigma$  is reported after the TOF- $N\sigma$  cut is applied. In the bottom panel the TPC- $N\sigma$  is shown after the additional ITS identification requirements have been applied.

In addition a minimum number of 5 cluster in the ITS (with at least two of them in the SPD layers) is applied. A hit in both the SPD layers is required in order to suppress the contribution of electrons coming from  $\gamma$  conversions in the material after the first SPD layer.

## 6. Elliptic flow of heavy-flavour decay electrons

### 6.1.2 TPC–EMCal

In the transverse momentum interval between  $3 < p_T < 13$  GeV/ $c$ , the electron identification is based on the measurement of the  $E/p$  ratio, where  $E$  is the energy of the EMCal cluster that matched the prolongation of the track with momentum  $p$  reconstructed in the TPC and ITS detectors. Electrons deposit their total energy in the EMCal and due to their small mass the  $E/p$  ratio should be close to unity, allowing for a further hadron rejection. Hadron contamination is removed selecting the electron signal in the TPC- $N\sigma$  between -1 and 3. The electron band can be observed in the  $E/p$  distribution as a function of  $p_T$  for semi-central events in Fig. 6.2. In the left panel the  $E/p$  distribution is reported for the MB centrality events, while in the right panel the  $E/p$  distribution is reported for EMCal Ssh trigger events. In the case of an EMCal trigger an enhancement of the electron sample for  $p_T > 7$  GeV/ $c$  (trigger threshold) with respect to the MB case is observed.

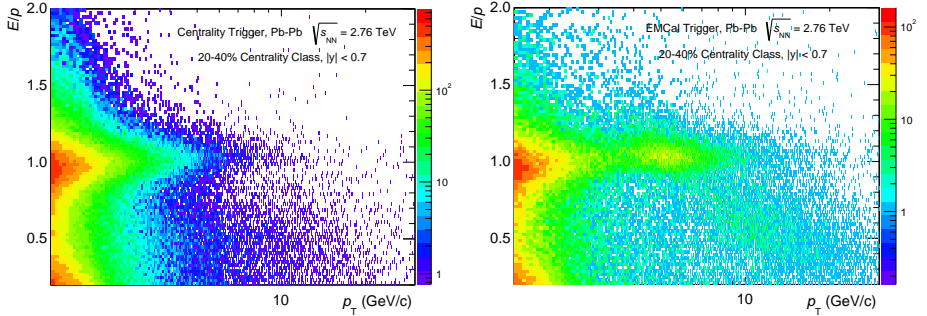


Figure 6.2:  $E/p$  for electrons and hadrons as a function of the transverse momentum after that the TPC- $N\sigma$  and shower shape cuts have been applied. In the left panel the  $E/p$  is measured in MB events for the 20-40% centrality class. In the right panel the same measurements are reported for the EMCal trigger shower trigger events, in which the electron enhancement is observed above the trigger threshold ( $p_T > 7$  GeV/ $c$ ).

In order to remove additional hadron contamination an other selection

## 6.1 Inclusive electron identification

---

has been applied on the electron candidates. This selection is based on the different shape of the shower between electrons and hadrons in EMCal detector. Basically it consists of cutting on the dimension of the short (M20) and long (M02) axis of the transversal projection of the shower and on its dispersion, a quantity proportional to the cluster width. On the latter quantity we applied a loose cut since M20 and M02 already allow to remove most of the hadron contamination.

Different cuts on the TPC- $N\sigma$  and on the shower shape have been tested in order to remove as much contamination as possible without suppressing too much the electron signal. The optimal set of cuts was chosen looking at the electron purity as a function of  $p_T$  for the different sets of cuts. In Fig. 6.3 the  $E/p$  distributions are reported for different electron identification cut values in the 20-40% centrality interval.

The black markers represent the electron candidates selected applying a TPC- $N\sigma$  cut between -1 and 3 without the additional requirements on the shower shape. The blue markers represent the electron candidates selected using again the same TPC- $N\sigma$  selection together with the shower shape cuts. The shower shape cut values are listed in Table 6.1. The red markers are the electron candidates selected using a looser TPC  $N\sigma$  cut ( $-2 < N\sigma < 3$ ) together with the shower shape requirements. Since this last  $N\sigma$  cut clearly leaves more hadron contamination in the electron sample the optimum value selected for the TPC- $N\sigma$  is  $-1 < \text{TPC-}N\sigma < 3$ . The electron signal is extracted from the EMCal detector selecting tracks that have a  $E/p$  between 0.8 and 1.2. Only 3 cluster in the ITS detector are required for the electron track selection, with at least one of the hits in one of the two SPD layers. The looser requirement on the number of hits in the SPD, increases the electron reconstruction and acceptance efficiency, which is already limited by the limited  $\varphi$  and  $\eta$  acceptance of the EMCal detector. On the other hand it results in a larger amount of conversion electrons and, consequently, in a smaller signal-to-background ratio for electrons from heavy-flavour hadron decays with respect to the ITS-TOF-TPC in the same transverse momentum interval. Because above 3 GeV/ $c$ , heavy-flavour decay electrons are already dominating the inclusive electrons we use at high  $p_T$  looser ITS cuts.

## 6. Elliptic flow of heavy-flavour decay electrons

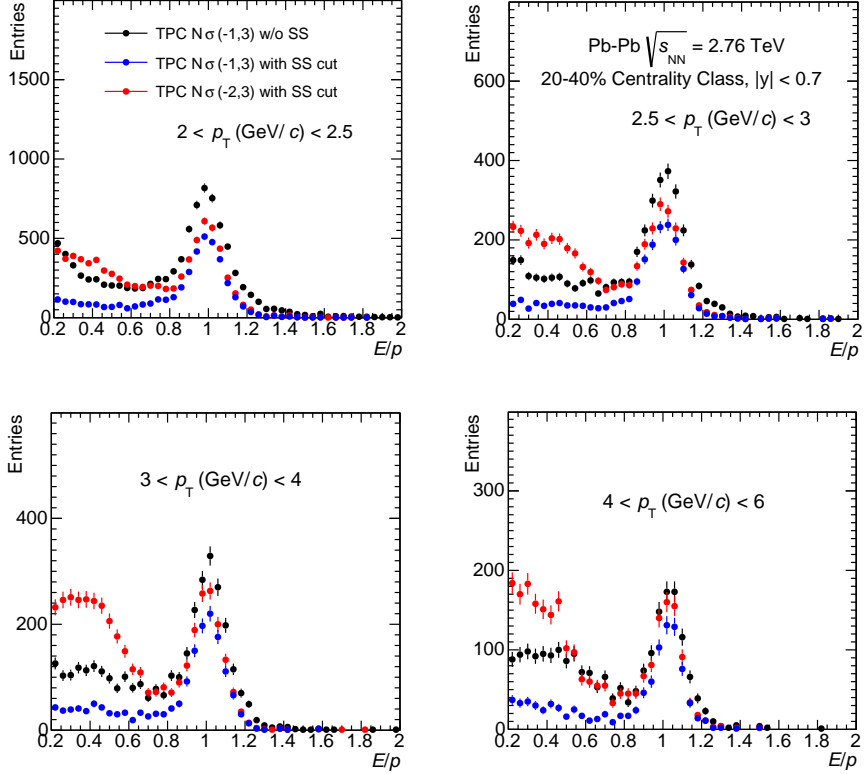


Figure 6.3:  $E/p$  distributions for different electron  $p_T$  bins for different identification cuts. See text for more details.

### 6.1.3 Inclusive electron purity

Since the elliptic flow of the inclusive electrons is computed even-by-event, it is important to check how large the residual hadron contamination included in the electron sample is after the identification procedure has been applied. Systematic effects introduced in the inclusive electron  $v_2$  by the hadron contamination have been studied in detail and are reported in section 6.1.5.

## 6.1 Inclusive electron identification

---

For low  $p_T$  the residual hadron contamination is estimated by fitting the measured TPC signal distributions with functions which model both the background and signal contributions. The fitting functions used to parameterize the TPC- $N\sigma$  distributions for the different hadron species are convolutions of Landau and exponential functions. In the left panel of Fig. 6.4 an example of the fit result is reported. The magenta line represent the parameterization of the  $\pi^\pm$  contribution, in blue the one for the electrons and in red the residual contamination from kaons and protons.

The electron purity is estimated integrating the different fitting functions shown in the equation below:

$$Purity = \frac{\int_{x_{min}}^{x_{max}} f_{elec}(x) dx}{\int_{x_{min}}^{x_{max}} f_{\pi}(x) + f_{p/k}(x) + f_{elec}(x) dx} \quad (6.2)$$

where  $x_{min}$  and  $x_{max}$  are the lower and upper limit of the TPC  $N\sigma$  used for the electron identification.

Hadron contamination in the EMCal case is estimated by looking at the  $E/p$  distribution of identified pions (TPC- $N\sigma < 4$  under the electron mass hypothesis), selected with the other electron criteria. The  $E/p$  distributions of the hadrons are scaled to the  $E/p$  distributions of the electron candidates for each  $p_T$  bin to the region of low  $E/p$  values. In the right panel of Fig. 6.4 a very good agreement between the  $E/p$  distributions for the electrons (black markers) and for the hadrons (magenta markers) for the region outside the electron peak is observed. The electron purity is estimated in this case integrating the  $E/p$  distributions according to the equation below:

$$Purity = \frac{\int_{x_{min}}^{x_{max}} f_{elec}(x) dx}{\int_{x_{min}}^{x_{max}} f_{had}(x) + f_{elec}(x) dx} \quad (6.3)$$

where  $x_{min}$  and  $x_{max}$  are the lower and upper  $E/p$  cut values.

In Fig. 6.5 the inclusive electron purity estimated in the 0-10% and 20-40% centrality intervals is plotted as a function of the transverse momentum up to  $p_T = 8$  GeV/ $c$  using only the centrality trigger. The black markers

## 6. Elliptic flow of heavy-flavour decay electrons

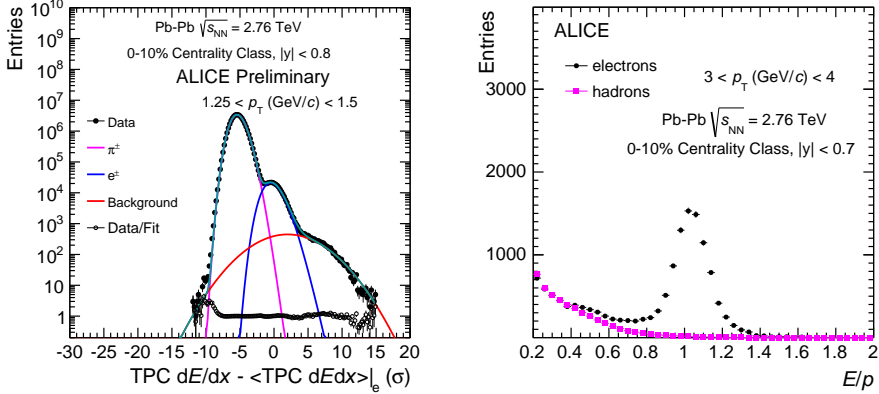


Figure 6.4: Left Panel: TPC  $N\sigma$  distribution for the electron with  $p_T$  between 1.25 and 1.5 GeV/c. The fitting functions used to parameterize the different particle species are reported as well. Right Panel:  $E/p$  for electron candidates (black markers) and hadrons (magenta markers) selected with a TPC- $N\sigma < 4$  under the electron mass hypothesis.

represent the purity of the electron sample determined for the ITS-TOF-TPC identification strategy, while with red markers the purity for the TPC-EMCal case is plotted.

For the ITS-TOF-TPC identification strategy the contamination is estimated to be less than 5% for  $p_T < 3$  GeV/c. At intermediate  $p_T$  ( $p_T > 3$  GeV/c) due to the relativistic rise of the  $dE/dx$  in the TPC, where the  $dE/dx$  bands for the different particle start to overlap, the measured hadron contamination start to be significant reaching a value of about 20%. For  $p_T$  between  $3 < p_T < 8$  GeV/c the hadron contamination estimated using the TPC-EMCal detectors is still lower than 5% and smaller than the one provided by the ITS-TOF-TPC analysis. For this reason the electron identification strategy used for the final heavy-flavour decay electrons measurements switches at  $p_T = 3$  GeV/c. As a further cross check on the electron identification purity at low  $p_T$ , the electron identification in the ITS

## 6.1 Inclusive electron identification

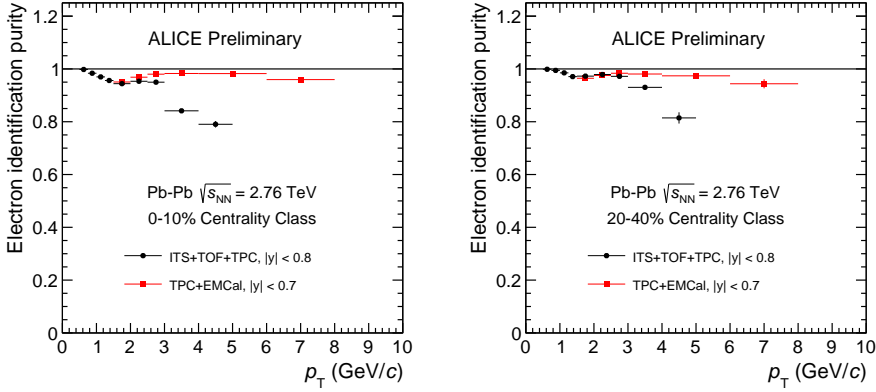


Figure 6.5: Inclusive electron purity as a function of the electron  $p_T$  in the 0-10% (left panel) and in the 20-40% (right panel) centrality classes. The ITS-TOF-TPC identification strategy is reported with black markers, while the TPC-EMCal strategy is reported with red markers.

detector has been totally removed for the  $p_T$  region between 1.5–3 GeV/c. The purity, for this case, is observed to decrease to about 4% because of a higher pion contamination, which shows that the ITS cut is necessary also in this transverse momentum region.

For both the electron identification strategies adopted, the residual hadron contamination in the inclusive electron sample does not exceed 5% in the full transverse momentum region and does not show any important centrality, event plane and  $\eta$  dependence, allowing for an even-by-event elliptic flow analysis.

### High $p_T$ electrons and EMCal trigger

At high transverse momentum ( $p_T > 8$  GeV/c) the inclusive electron identification is performed with the TPC-EMCal strategy. In Fig. 6.6 the  $E/p$  distribution for electrons (black markers) and hadrons (magenta markers) is

## 6. Elliptic flow of heavy-flavour decay electrons

shown for the  $p_T$  bins between 8-10 and 10-13 GeV/ $c$  for the EMCal single shower trigger in the 20-40% centrality interval. At high  $p_T$  hadrons start to deposit more energy in the calorimeter resulting in a  $E/p$  closer to unity. Despite the strong TPC- $N\sigma$  and shower shape cuts, the contamination is estimated to be significant in this  $p_T$  region, reaching about  $\sim 20\%$  ( $\sim 30\%$ ) for  $8 < p_T < 10$  GeV/ $c$  ( $10 < p_T < 13$  GeV/ $c$ ) in both the EMCal trigger data (10-20% and 20-40% centrality intervals) and in the centrality trigger (0-10% centrality class).

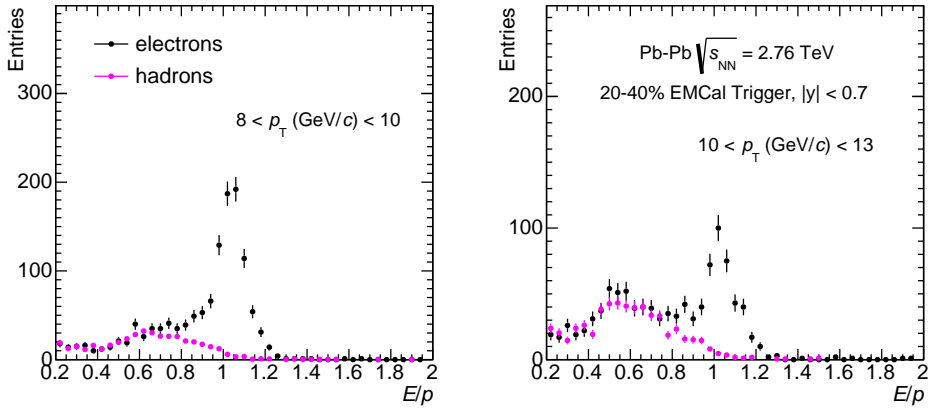


Figure 6.6:  $E/p$  for electron candidates (black markers) and hadrons (magenta markers) at high transverse momentum for the 20-40% centrality interval for the EMCal single shower trigger events.

Because of the higher hadron contamination in the electron sample, the  $v_2$  coefficient cannot be measured event-by-event. The even plane method is therefore used calculating the in and out plane ratio, equation 3.9, a technique that allows to remove the residual contamination from the  $E/p$  distribution before the extraction of  $v_2$ . In this  $p_T$  interval the elliptic flow is not measured with the scalar product because this method does not allow to statistically subtract the hadron contamination.

As an additional check on the triggered electron spectra, the relative

## 6.1 Inclusive electron identification

EMCal single shower trigger efficiency has been calculated in the 10-20% and 20-40% centrality intervals dividing the raw electron yield in the EMCal trigger per event to the one measured in the centrality trigger. The trigger efficiency, reported in Fig. 6.7, is flat above the trigger threshold ( $p_T \sim 7$  GeV/c) for the two centrality classes used in the analysis, confirming that no bias in the electron spectra at high transverse momentum is observed, and allowing for an elliptic flow measurement within the EMCal trigger sample. A fit with a constant is performed above threshold in order to extract the averaged trigger efficiency. The flatness of the relative trigger efficiency has also been checked in the different event plane directions, and also in this more differential case no trigger bias has been observed above threshold.

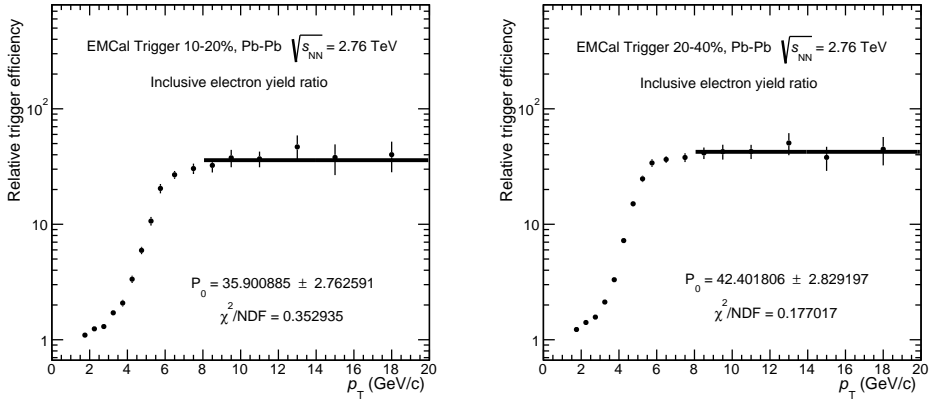


Figure 6.7: Ratio of electron yield in EMCal trigger to MB centrality trigger as a function of  $p_T$  in 10-20% (left panel) and 20-40% (right panel) centrality intervals.

## 6. Elliptic flow of heavy-flavour decay electrons

Detector	Type	Requirement
	Min TPC clusters	100
	Min TPC clusters for $dE/dx$	90
	Min ratio of TPC clusters	0.6
	Min ITS clusters	5 ( $p_T \leq 3$ GeV/c)
		3 ( $p_T > 3$ GeV/c)
	Max $\chi^2$ per TPC cluster	3.5
	Require TPC refit	yes
	Require ITS refit	yes
	Require hits in the SPD layer	2 ( $p_T \leq 3$ GeV/c)
		1 ( $p_T > 3$ GeV/c)
	Accept kink daughters	no
	DCA <sub><i>x,y</i></sub>	$\leq 2.4$ cm
	DCA <sub><i>z</i></sub>	$\leq 3.2$ cm
ITS-TOF-TPC		
	$p_T$ (GeV/c)	(0.5, 3.0)
	$ \eta $	$> 0.8$
	N $\sigma$ ITS	(-1;1) $p_T < 1.5$ GeV/c
		(-2;2) $p_T \geq 1.5$ GeV/c
	N $\sigma$ TOF	(-2;2)
	N $\sigma$ TPC	(-1;3) $p_T < 1.5$ GeV/c
		(0;3) $p_T \geq 1.5$ GeV/c
TPC-EMCal		
	$p_T$ (GeV/c)	(3, 13)
	$ \eta $	$> 0.7$
	N $\sigma$ TPC	(-1;3)
	$E/p$	(0.8;1.2)
	M20	(0.03,0.3) (short axis)
	M02	(0.03,0.5) (long axis)
	Dispersion	$< 1$

Table 6.1: Track selection and identification cuts for electron candidates.

## 6.1 Inclusive electron identification

### 6.1.4 Inclusive electron $v_2$

The elliptic flow of inclusive electrons ( $v_2^{e^\pm}$ ) is measured in the centrality intervals 0-10%, 10-20% and 20-40% as a function of the transverse momentum. Figure 6.8 shows the  $p_T$ -differential elliptic flow of inclusive electrons ( $v_2^{e^\pm}$ ) measured with the event plane (black markers) and scalar product (red markers) methods in the 0-10% (left), 10-20% (middle) and 20-40% (right) centrality classes in Pb-Pb collisions at  $\sqrt{s_{NN}} = 2.76$  TeV. In this analysis the event plane is reconstructed with the VZERO detectors and a three sub-events resolution method has been used (section 3.1.1). While for the scalar product, the  $v_2$  measurements have been carried out combining results from two symmetric TPC sub-events as in equation 3.12. The scalar product and the event plane give consistent results at low  $p_T$ . At higher  $p_T$  the event plane results are slightly lower because of the larger  $\eta$  gap imposed between the different sub-events, indicating a possible stronger suppression of the non-flow contributions in the higher  $p_T$  region.

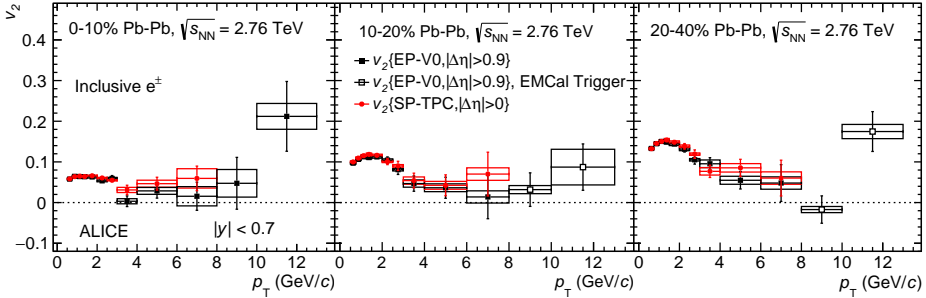


Figure 6.8: Inclusive electrons  $v_2$  as a function of  $p_T$  measured with the event plane (black marker) and scalar product (red markers) methods in the 0-10% (left), 10-20% (middle) and 20-40% (right) centrality classes in Pb-Pb collisions  $\sqrt{s_{NN}} = 2.76$  TeV.

However the measurements obtained with different  $\eta$  gaps agree within the statistical uncertainties. Therefore, the expected bias due to non-flow correlations is within the statistical precision of the measurement. Also

---

## 6. Elliptic flow of heavy-flavour decay electrons

---

possible effects due to the possible ambiguity in the event plane method with respect to the scalar product method are not observed [77] in this analysis.

For both methods the values of  $v_2^{e^\pm}$  slightly increase from central to semi-central collisions and this effect is more pronounced in the intermediate  $p_T$  region  $2 < p_T < 4$  GeV/ $c$ .

The inclusive electron  $v_2$  is not measured with the scalar product method for the EMCal single shower trigger data because of the large hadron contamination estimated at high transverse momentum. For this reason the scalar product method has been used up to  $p_T = 8$  GeV/ $c$ , where the inclusive electron purity has been estimated to be larger than 95%.

### 6.1.5 Systematic uncertainties

Several sources of systematic uncertainty affecting the inclusive electron elliptic flow measurement are considered. In the following paragraphs these are summarized. The contributions estimated from the different sources are summed in quadrature in order to estimate the total systematic uncertainty on the elliptic flow of the inclusive electrons. A summary of the systematic uncertainties for the different  $p_T$  bins is presented in Table 6.1.5.

**Event plane resolution** One of the main ingredients used in an event plane flow analysis is the resolution parameter  $R_2$ . Two different sources of systematic error are considered from the estimation of the three sub-events resolution. The first uncertainty comes from the variation of the definition of the TPC sub-events in the determination of the event plane resolution. The standard sub event selection consists in reconstructing the event plane using tracks in the positive ( $0 < \eta < 0.8$ ) and negative ( $-0.8 < \eta < 0$ ) pseudo-rapidity regions of the TPC. As a systematic check we reduced the  $\eta$  regions to  $0.2 < \eta < 0.8$  and  $-0.8 < \eta < -0.2$ . A maximum of 2% difference was observed in most central collision, while in the more peripheral collisions the difference has been observed to be less than 1%. The uncertainty due to the centrality dependence of the event plane resolution is estimated from the difference between the two ways to define the average resolution in the

## 6.1 Inclusive electron identification

---

centrality classes used for the analysis. Starting from the resolutions in 5% centrality intervals a plain arithmetic average and an average weighted with the inclusive electron yield measured in the same 5% wide centrality classes has been calculated. The difference between these averages is about 2.7% in the most central events, where the resolution strongly depend on the centrality, and 1% for semi central events. Those two systematic contributions are not considered in case of the scalar product method.

**Hadron contamination** Since the elliptic flow coefficient is measured event-by-event, the measurements could be affected by hadron contamination. Using the additive properties of  $v_2$ , one way to estimate the possible contribution of the hadron contamination on the inclusive electron  $v_2$  measurements is to use the estimated purity of the electron sample and subtract the  $v_2$  of the hadron contamination according to equation 6.4:

$$v_2^{incl} = P \cdot v_2^{elec} - (1 - P) \cdot v_2^{cont} \quad (6.4)$$

where  $v_2^{incl}$  is what we directly measure,  $v_2^{cont}$  is the elliptic flow of the hadron contamination,  $P$  is the purity of our electron sample, and  $v_2^{elec}$  is what we want to obtain after the correction is applied. This procedure assumes a good knowledge of the separate hadron sources contaminating the electron sample. In this study the contamination is found to be composed mainly of charged pions, dominantly at high  $p_T$  where the purity decreases, and the  $v_2^{cont}$  is therefore taken as  $v_2^{pions}$  [79, 82]. Another check performed is statistically removing the hadron contribution from the inclusive electron sample before the extraction of the  $v_2$  coefficient. This check is only possible with the event plane method using once more equation 3.9. With this method the  $v_2$  coefficient is extracted using the number of electrons measured in and out of plane, allowing for statistically removing the hadron contamination via the fits of the TPC- $N\sigma$  and using the estimated  $E/p$  distribution of hadrons reported in the purity section. From both tests the systematic uncertainty introduced by the hadron contamination is estimated to be of the order of 1-2% at low  $p_T$  and slightly increasing with  $p_T$  up to 5%. This component is not considered for the EMCal trigger

---

## 6. Elliptic flow of heavy-flavour decay electrons

---

measurements, since there the contamination contribution is subtracted.

**Electron identification cut variation** One of the main contribution to the systematic uncertainties of the inclusive electron  $v_2$  is the variation of the electron selection and identification cuts. In order to have a precise estimation of the systematic uncertainty, and to avoid as much as possible statistical fluctuations, an r.m.s approach has been used in this case. Several electron selection and identification cuts are systematically varied around the default value used in the analysis. Distributions of the absolute difference between the  $v_2$  measured using the default cuts and the one obtained varying the selection criteria have been made. From those distributions, which have a Gaussian shape, the mean and the r.m.s parameter were extracted. Since the mean has been found to be compatible with zero as a function of the transverse momentum, the r.m.s value has been used as the absolute systematic uncertainty on the inclusive electron  $v_2$  measurements. This systematic uncertainty is estimated to be of the order to 1-2% for the low  $p_T$  analysis, while at high  $p_T$  this component was the dominant one leading to a variation of about 30% in the highest  $p_T$  bins. No centrality dependence is observed for the systematic uncertainty estimated from the electron cut variation for both the identification strategies.

**Magnetic field and  $\eta$  dependence** During the 2011 data period, the polarization of the magnet field (B) was changed during the data taking. A systematic uncertainty is studied by comparing the inclusive electron elliptic flow measured from the two event samples separately and a contribution of 1% is assigned to the  $v_2$  measurements. A related stability check on the magnetic field consists of the measurement of  $v_2$  in the two symmetric pseudorapidity regions, using electrons only coming from the positive/negative  $\eta$  region of the TPC and the results have been found to be compatible within the statistical uncertainties.

## 6.1 Inclusive electron identification

**Trigger effect** A possible bias in the analysis performed with the events triggered by the EMCal has been studied and is reported in section 4.4 for unidentified charged particles. According to a toy MC model calculation, above the trigger threshold no bias is expected. Nevertheless an additional systematic uncertainty, listed in Table 6.3, has been estimated in the 10-20% and 20-40% centrality classes looking at the differences observed between the  $v_2$  of charged hadrons measured with full azimuthal coverage in the centrality trigger events and in the single-shower trigger events inside the azimuthal coverage of the EMCal detector.

0-10% (10-20% – 20-40%) centrality class				
$p_T$ (GeV/c):	0.5-3.0	3-4	4-8	8-13
B field dependence	1%	1%	1%	1%
hadron contamination	1%	3%	5%	0%
averaged $R_2$	2.7%(1%)	2.7%(1%)	2.7%(1%)	2.7%(1%)
sub-event definition	2%(1%)	2%(1%)	2%(1%)	2%(1%)
electron identification $\rightarrow$ extracted from the r.m.s of $v_2 - v_2^{varied}$				

Table 6.2: Systematics uncertainties assigned to the inclusive electron  $v_2$  in Pb-Pb collisions at  $\sqrt{s_{NN}} = 2.76$  TeV.

$p_T$ (GeV/c):	8-10	10-13
10-20% centrality	15%	20%
20-40% centrality	1%	2%

Table 6.3: Additional systematic uncertainties for inclusive electron  $v_2$  measured with the EMCal trigger data.

## 6.2 Photonic electron background

To extract the heavy-flavour signal, the background contributions have to be subtracted from the inclusive electron  $v_2$ . The other ingredients necessary to extract the heavy-flavour decay electron  $v_2$  are the inclusive-over-background ratio ( $1 + R_{SB}$ ) and the electron background elliptic flow.

The inclusive electron sample consists mainly of three components:

1. Electrons from heavy-flavour hadron decays and dielectron decays of heavy quarkonia ( $J/\psi$ ,  $\Upsilon$ ).
2. Photonic background<sup>1</sup> from Dalitz decays of light neutral mesons and  $\gamma$  conversions as well as from real and virtual direct photons from hard scattering processes.
3. Non-photonic background from  $K \rightarrow e\pi\nu$  ( $K_{e3}$ ), and dielectron decays of light vector mesons.

The contribution of  $J/\psi$ , relevant for  $p_T > 3$  GeV/ $c$  is not subtracted in this analysis. The  $K_{e3}$  and  $\Upsilon$  are not expected to be relevant in the  $p_T$  range considered. The relative contribution from  $K_{e3}$  decays to the inclusive electron background at  $p_T = 0.5$  GeV/ $c$  was not more than 0.5% and it decreases with  $p_T$  [105]. The remaining background is mainly coming from photonic background. Two different strategies are used to measure the electrons coming from the different background sources. The background decay electron  $v_2$  and  $p_T$  spectra are measured with the invariant mass method [106]. The background electron  $v_2$  is measured up to  $p_T = 1.5$  GeV/ $c$  and at higher  $p_T$ , where the measurements of the background sources starts to be limited by statistics, a cocktail has been used [105].

### 6.2.1 Invariant mass method

Electrons from photon conversions and Dalitz decays always come as an electron and positron pair with a very small invariant mass value. This is

---

<sup>1</sup>In this analysis "photonic" refers to the  $\gamma$  conversion and neutral Dalitz decay contributions

## 6.2 Photonic electron background

---

used to select electrons from photonic sources, this mass correlation does not hold for heavy-flavour decay electrons.

Part of the photonic electron background,  $N^{Reco-Background}$ , is reconstructed statistically by pairing electrons with opposite charge (unlike-sign) in the same event and calculating the invariant mass for each pair and subtracting the combinatorial background using the like-sign invariant mass spectrum as in equation 6.5.

$$N^{Reco-Background} = N^{ULS} - N^{LS} \quad (6.5)$$

An example of the invariant mass distribution calculated for the low ( $1 < p_T < 1.25 \text{ GeV}/c$ ) and high  $p_T$  ( $3 < p_T < 4 \text{ GeV}/c$ ) electron identification strategy is plotted in the left and right panel of Fig. 6.9 respectively. The black markers represent the unlike-sign (ULS) distribution, in which the photonic peak at low mass is observed. The red open markers show the like-sign (LS) pair distribution. For both the electron identification strategies one observes a good description of the combinatorial background by the LS pair distribution.

Unlike-sign background electrons are selected if the created pair fulfills the requirement on the invariant mass. For low  $p_T$  an invariant mass cut is placed at  $70 \text{ MeV}/c^2$ , while at higher transverse momentum the mass cut is placed at  $140 \text{ MeV}/c^2$ . The same mass cut is required for LS pairs in order to evaluate the combinatorial background in the same invariant mass window. The difference in the invariant mass cut, used for the two different identification strategies, is because of a bias in the Monte Carlo (MC) production related to the embedded  $\pi^0$  sample. Further details on that are given later in the text.

The total number of background electrons is given by equation 6.6 where the  $N^{notReco-Background}$  is the number of photonic electrons that are not reconstructed in this analysis with the invariant mass technique. This can be estimated computing and applying a reconstruction efficiency correction,  $\epsilon^{Background}$ , on the number of  $N^{Reco-Background}$  as in equation 6.7

$$N^{all-Background} = N^{Reco-Background} + N^{notReco-Background} \quad (6.6)$$

## 6. Elliptic flow of heavy-flavour decay electrons

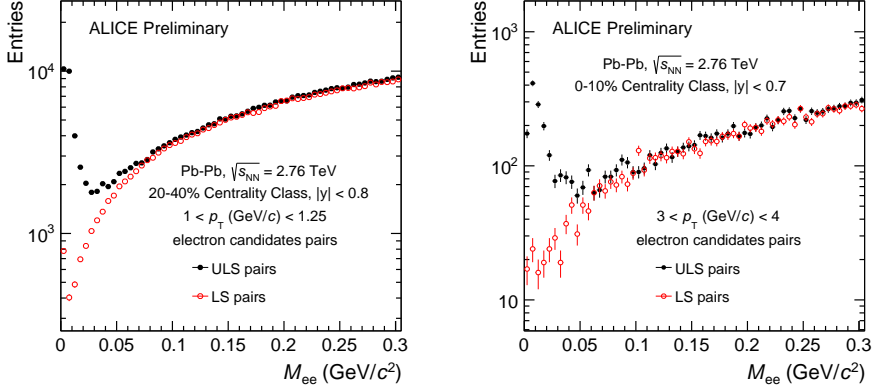


Figure 6.9: Invariant mass distributions of unlike-sign (black full markers) and like-sign (red open markers) pairs for the ITS-TOF-TPC electron identification (left panel) and for the TPC-EMCal strategy are reported.

$$N^{notReco-Background} = \left( \frac{1}{\epsilon_{Background}} - 1 \right) N^{Reco-Background} \quad (6.7)$$

The  $N^{all-Background}$  can be calculated from previous equations as reported in equation 6.8:

$$N^{all-Background} = \frac{(N^{ULS} - N^{LS})}{\epsilon_{Background}} \quad (6.8)$$

The photonic electron reconstruction efficiencies are evaluated from MC simulations and are explained in details in the next section. In order to find the partner electron with high tagging efficiency, loose electron identification cuts are applied on the associated candidate used to reconstruct the pairs. A summary of the selection cuts applied in the associated electrons and on the pairs is listed in Table: 6.4

## 6.2 Photonic electron background

associated electron	Type	Requirement
	$p_T \text{ min (GeV}/c)$	0.0 (ITS-TOF-TPC), 0.3 (TPC-EMCal)
	$ \eta $	$> 0.9$
	Min TPC clusters	80
	Require TPC refit	yes
	Require ITS refit	yes
	Accept kink daughters	no
	$DCA_{x,y}$	$\leq 2.4 \text{ cm}$
	$DCA_z$	$\leq 3.2 \text{ cm}$
	TPC- $N\sigma$	(-3;3)
pair	Type	Requirement
	Invariant mass ( $\text{MeV}/c^2$ )	70 (ITS-TOF-TPC) 140 (TPC-EMCal)

Table 6.4: Track cuts for associated electron and for pair selection.

### 6.2.2 Photonic electron reconstruction efficiency

Due to detector acceptance and tracking inefficiencies, for reconstructing the partner electrons, not all the photonic electrons are identified using the invariant mass technique. This effect is taken into account correcting the photonic electron yield for the reconstruction efficiency computed in Monte Carlo (MC) simulations.

The light meson cross-section in MC generators can give the wrong reconstruction efficiency if the shape of the  $p_T$ -differential distribution is different from the real distribution. The  $p_T$  shape of the pure HIJING spectra is observed to be slightly different from the measured ones and a correction for this difference has to be applied.

Furthermore, in the MC production used in this analysis a sample of  $\pi^0$  and  $\eta$  mesons are embedded in order to increase the statistics of electrons from  $\pi^0$ ,  $\eta$  and  $\gamma$  used to compute the photonic reconstruction efficiency.

## 6. Elliptic flow of heavy-flavour decay electrons

---

The neutral mesons enhanced in the sample are forced to decay in the Dalitz channel or in double  $\gamma$  decay. The enhanced sample is generated with a flat  $p_T$  distribution in the pseudo-rapidity region ( $|\eta| < 1.2$ ), introducing an other bias in the  $p_T$  distribution of the MC productions.

The  $p_T$  distribution of the HIJING generator, of the embedded sample in the MC together with the parameterization used in the cocktail simulation are shown for the  $\pi^0$  and  $\eta$  meson in the left and right panel of Fig. 6.10 respectively. The cocktail parameterizations are obtained using  $m_T$  scaling starting from a fit of fully corrected charged/neutral pion spectra. A weighting procedure has been used to correct for the shape of the MC electrons  $p_T$  spectra used in the computation of the reconstruction efficiency.

**Weighting procedure:** The default weights are evaluated using the  $p_T$  spectra parameterization used in the cocktail simulation. Weight distributions as a function of the meson  $p_T$  are defined dividing the cocktail parameterizations for the  $p_T$  spectra of the MC sample. The weight distributions are fitted with a Hagedron function, defined as:

$$A/\exp(-Bp_T - Cp_T^2) + (p_T/D)^E, \quad (6.9)$$

where A, B, C, D and E are parameters of the fitting function. These functions represent the  $p_T$  dependent weights that have to be applied to the electron  $p_T$  spectra in the MC in order to restore their proper  $p_T$  shape. For  $p_T < 3$  GeV/c the MC statistic available of  $\pi^0$  and  $\eta$  generated with HIJING allows to avoid the embedded sample in the computation of the photonic reconstruction efficiency. At higher  $p_T$  the pure HIJING sample has too few entries and the enhanced sample is necessary for a stable computation of the photonic reconstruction efficiency.

A mistake has been found for the embedded  $\pi^0$  sample in the MC productions used, which is why the embedded sample is rejected at low  $p_T$ . The invariant mass distribution of true electron-positron pairs coming from the  $\pi^0$  Dalitz decay was not generated with the correct shape. The invariant mass distribution of electron-positron pairs coming from  $\pi^0$  Dalitz decay is expected to be described by a Kroll-Wada function [107]. In the embedded

## 6.2 Photonic electron background

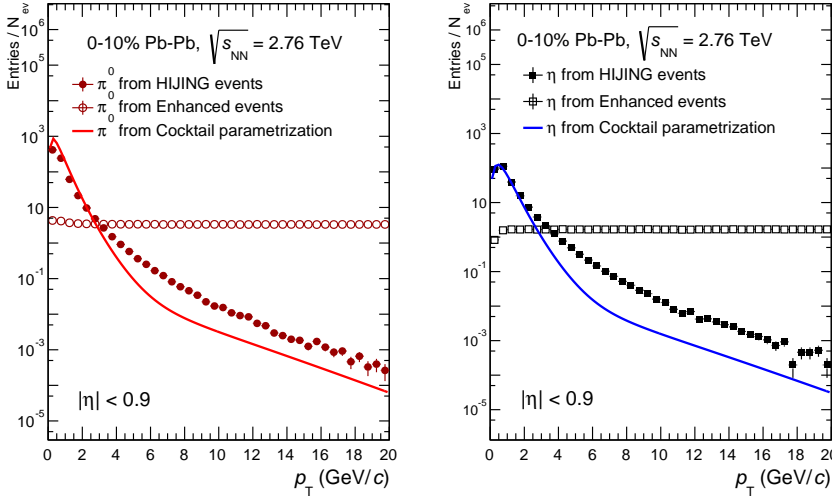


Figure 6.10:  $\pi^0$  (left) and  $\eta$  (right) transverse momentum distributions from HIJING MC event generator (full markers) and the enhanced sample (open markers). They are reported together with the cocktail parameterizations (lines) for the 10% most central collisions.

MC sample it has a flat distribution smoothly ending at the  $\pi^0$  mass value. This difference has a strong effect on the tagging efficiency when varying the invariant mass cut applied on pairs. In case of a tight invariant mass cut it results in a very low tagging efficiency, which leads to over-correcting the raw  $p_T$  spectra measured from the data. This issue has been avoided in the TPC-EMCal analysis applying a looser cut on the invariant mass of  $140 \text{ MeV}/c^2$ , selecting in this way all the electron coming from  $\pi^0$  dalitz in the MC production used to compute the photonic tagging efficiency, and removing from the latter any dependency on the  $\pi^0$  invariant mass. For the low  $p_T$  analysis it was enough to reject all the events in the MC not belonging to the HIJING generator.

A Monte Carlo closure test has been performed to confirm that the strat-

## 6. Elliptic flow of heavy-flavour decay electrons

---

egy of placing the mass cut at  $140 \text{ MeV}/c^2$  would remove any bias coming from the enhanced  $\pi^0$  sample. The tagging efficiencies have been computed using a pure HIJING sample without applying any weight and using the enhanced sample only applying HIJING spectra as weights. When applying a mass cut of  $70 \text{ MeV}/c^2$  the MC closure test failed and the efficiency computed from the enhanced sample did not match the pure HIJING one even after the weights were applied. For a mass cut placed at  $140 \text{ MeV}/c^2$  the MC closure was successful and the tagging efficiency after the HIJING weights was restored. Where the ITS-TOF-TPC identification strategy is used, a mass cut of  $140 \text{ MeV}/c^2$  is not used because for the first  $p_T$  bins ( $0.5 < p_T < 0.75 \text{ GeV}/c$ ) in the most central events the LS pair distribution has been observed not to perfectly describe the combinatorial background at very high mass, giving a slight over-estimation of the photonic background electrons.

The photonic electron reconstruction efficiencies (tagging efficiency) used to correct the raw yield of the background electrons are reported in Fig. 6.11 for the 0-10% centrality class, in the left and in the right panel the efficiencies for the low and high  $p_T$  electron identification strategy are shown respectively. The averaged efficiency of electrons coming from  $\pi^0$ ,  $\eta$  and  $\gamma$  are plotted with full blue markers, and the efficiency increases with increasing  $p_T$ , reaching a value of  $\sim 70\%$  in the high transverse momentum region for both the identification strategies. When comparing the efficiencies of the different electron sources it is observed that the electrons coming from a  $\eta$  dalitz decay (green markers) have a lower efficiency because of their larger mass window with respect to the  $\pi^0$  (red markers) and  $\gamma$  (purple markers). A peculiar observation is that the electrons from  $\gamma$  conversion show an efficiency systematically lower than the  $\pi^0$  for both the identification strategies. This systematic effect is introduced by the contribution of electrons coming from  $\gamma$  conversions far away from the primary vertex, that have a poorer  $p_T$  and azimuthal angle resolution, leading to a lower reconstruction efficiency. This effect has been investigated (not only for the efficiency calculation) and additional details are reported in section 6.2.6.

## 6.2 Photonic electron background

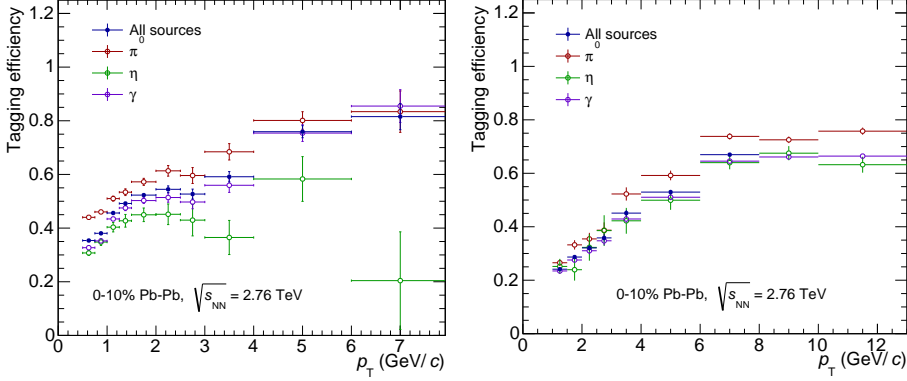


Figure 6.11: Reconstruction efficiency of photonic electrons computed using the invariant mass method for the two different inclusive electron identification strategy. Left panel for the ITS-TOF-TPC and right for the TPC-EMCal. Left panel for the ITS-TOF-TPC and right for the TPC-EMCal. The efficiencies for electrons coming from different sources ( $\pi^0$ ,  $\eta$  and  $\gamma$ ) are reported with different colours.

### 6.2.3 $(1 + R_{SB})$ and systematic uncertainties

The inclusive over background ratio  $(1 + R_{SB})$  is calculated dividing the inclusive electron yield by the background electrons corrected for the tagging efficiency as reported in equation 6.10

$$(1 + R_{SB}) = \frac{N^{e^\pm}}{N^{all-Background}} \quad (6.10)$$

The inclusive over background ratio measured with the invariant mass method is shown in Fig. 6.12 for the 0-10% (left), 10-20% (middle) and 20-40% (right) centrality intervals in Pb-Pb collisions at  $\sqrt{s_{NN}} = 2.76$  TeV. The black full markers represent the centrality trigger measurements, while in the 10-20% and 20-40% centrality classes the EMCal trigger results are reported with open black markers.

The  $(1 + R_{SB})$  increases with transverse momentum for all the centrality

## 6. Elliptic flow of heavy-flavour decay electrons

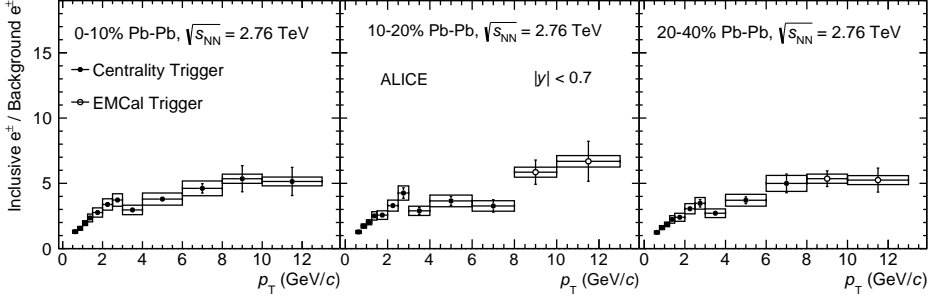


Figure 6.12: Inclusive over background ratio in the 0-10% (left), 10-20% (middle) and 20-40% (right) measured with the invariant mass method in the  $p_T$  interval between 0.5 and 13 GeV/c in Pb-Pb collisions at  $\sqrt{s_{NN}} = 2.76$  TeV. In the 10-20% and 20-40% centrality classes the EMCal trigger measurements are reported with open markers.

classes, indicating that at high  $p_T$  ( $p_T \sim 2.5$ -3 GeV/c) the heavy-flavour decay electrons become the dominant source of the inclusive sample. It then saturates around  $p_T \sim 6$  GeV/c, where the ratio between heavy-flavour decay electrons and the electron background starts to be constant. The small deviation observed in all the centrality classes at  $p_T = 3$  GeV/c is introduced by the different number of hits required in the SPD layers for each track between the two different electron identification strategies. For  $p_T < 3$  GeV/c a hit in both the pixel layers is required, resulting in an increase of the inclusive over background ratio, because many electrons coming from  $\gamma$  conversions in the first layer are rejected by this track cut. For the EMCal a looser requirement has been applied in order to increase the electron reconstruction efficiency and acceptance, already limited by the limited  $\varphi$  and  $\eta$  acceptance of the EMCal detector, and to decrease the azimuthal anisotropy for the electrons caused by SPD dead zones. At high  $p_T$  this is observed to be a safe choice because the inclusive over background ratio is already dominated by the heavy-flavour decay electrons contribution, while at lower  $p_T$  in order to suppress the huge photonic background electron contribution a stronger ITS requirement has to be used.

## 6.2 Photonic electron background

---

Several sources of systematic uncertainty are considered for the stability of the background electron reconstruction procedure. These include the changes in the  $(1 + R_{SB})$  due to the variations of the selection criteria applied on the partner electrons used to build the pairs and on the pair itself. The maximum variation among the different criteria is taken as a systematic uncertainty.

At low transverse momentum one of the dominant sources is the cut placed on the minimum  $p_T$  applied on the partner electron. This effect is estimated to be about 6% and is understood to be related to the large number of electrons coming from  $\gamma$  conversions in the detector material far away from the primary vertex. These electrons, mainly populating the low transverse momentum region, due to fake assigned clusters, have a poor  $p_T$  and azimuthal angle resolution. At high transverse momentum no systematics have been observed due to this cut.

The uncertainty coming from the Monte Carlo is estimated looking at the maximum variation between the default  $(1 + R_{SB})$  and the one obtained correcting the spectra using the HIJING efficiency without weights. At high  $p_T$ , where the enhanced sample of neutral mesons is used, the uncertainty has been estimated applying HIJING spectra as weights instead of the cocktail spectra, always applying a mass cut of  $140 \text{ MeV}/c^2$ . At very low  $p_T$  ( $0.5\text{-}1.25 \text{ GeV}/c$ ) the systematic uncertainty is estimated to be about 5%, while for the intermediate  $p_T$  region the uncertainty reaches about 10%, decreasing again to 5% at higher  $p_T$ , where the background electron contribution becomes less important and the efficiency saturates.

The invariant mass cut is found to be the dominant source for the EMCAL analysis. This is related to the invariant mass of the  $\pi^0$  Dalitz decay discovered in the embedded sample of the MC productions. This leads to a large loss of electrons coming from  $\pi^0$  Dalitz decay when a tight mass cut is applied in the MC, resulting in an overcorrection of the background electron  $p_T$  spectra. For the EMCAL analysis a 10% systematic uncertainty is assigned due to variation of the  $(1 + R_{SB})$  estimated by varying the invariant mass cut. At low  $p_T$ , where the embedded sample is rejected, the systematic uncertainty introduced by the mass cut is estimated to be around 3%. A summary of the systematic uncertainties assigned to the

## 6. Elliptic flow of heavy-flavour decay electrons

inclusive-over-background ratio is shown in Table:6.5.

$p_T$ (GeV/c):	0.5-1.25	1.25-3	3-8	8-13
Invariant mass	3%	3%	10%	5%
TPC cluster on partner	2%	2%	5%	5%
$p_T$ cut on partner	6%	6%	—	—
MC efficiency reconstruction	5%	10%	5%	2%

Table 6.5: Systematics uncertainties assigned to the  $(1 + R_{SB})$  in central and semi-central Pb-Pb collisions at  $\sqrt{s_{NN}} = 2.76$  TeV.

### 6.2.4 Background $v_2$

The photonic background electron  $v_2$  is measured with the invariant mass method at low transverse momentum, for  $p_T < 1.5$  GeV/c. At higher  $p_T$ , where the measurements of the background sources starts to be limited by statistics, a cocktail method has been used.

For this measurement, only the event plane method has been used, because it is the only method that allows to measure the  $v_2$  directly extracting statistically the raw yield of the reconstructed background electrons ( $N^{ULS} - N^{LS}$ ) in different regions  $\Delta\varphi = \varphi - \Psi_2$  as reported in section 3.1. The  $dN/d\Delta\varphi$  method is used to measure the background electron  $v_2$ . The number of electrons that create pairs that satisfy the requirement on the invariant mass are flagged as unlike-sign and/or like-sign electrons and counted in each  $p_T$  and  $\Delta\varphi$  bins. In this case the contamination contribution is statistically subtracted fitting the TPC signal and estimating the raw yield in different event plane regions. For a fixed  $p_T$  bin the number of reconstructed photonic electrons as a function of  $\Delta\varphi$  is fitted with equation 3.6, where  $v_2^{obs}$  is a fit parameter and it is corrected with the three sub-event resolution in order to obtain the elliptic flow of the photonic electrons. An example, for the 20-40% centrality interval, of the reconstructed raw yield of background electrons extracted as a function of  $\Delta\varphi$  is reported in the left and right panel of Fig. 6.13, together with the fit function. Also the

## 6.2 Photonic electron background

in- and out-of-plane ratio technique has been tested as a cross check for the stability of the fit employed in the  $\Delta\varphi$  method and no systematic effect has been observed in the background measurements.

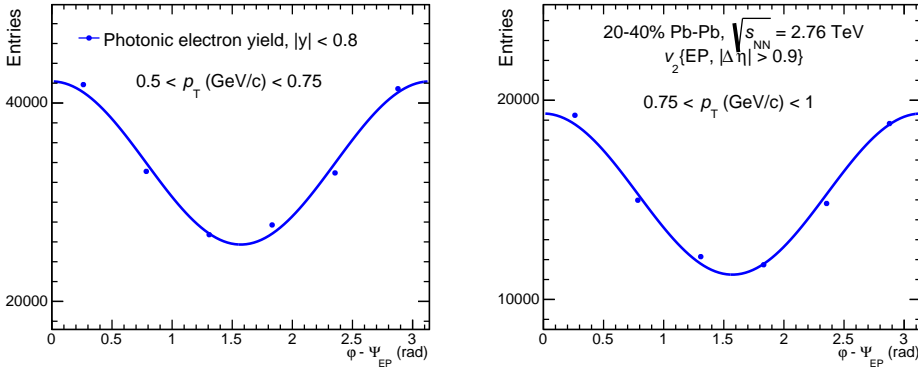


Figure 6.13:  $dN/d\varphi$  distributions of inclusive electrons in different the  $p_T$  ranges  $0.5 < p_T < 0.75$  GeV/ $c$  (left) and  $0.75 < p_T < 1$  GeV/ $c$  (left) in 20-40% centrality interval in Pb-Pb collisions at  $\sqrt{s_{NN}} = 2.76$  TeV.

The  $v_2$  measurements of the photonic electrons as a function of  $p_T$  are shown in Fig. 6.14 with the dark magenta symbols. In the same figure the cocktail results are plotted with azure symbols which will be discussed in the next section.

The same systematic studies performed on particle identification, selection of the partner electron and on the mass pair requirements performed for the  $p_T$  spectra are also done for the elliptic flow measurements. The uncertainties are estimated to be 20% in most central collisions and 10% for the 10-20% and 20-40% centrality classes. The systematics from the event plane resolution parameter and from the magnetic field dependence are estimated using the same procedure as for the inclusive electron  $v_2$  and are estimated to be of the same size. An additional component is estimated looking at the discrepancy with respect to the background  $v_2$  measured with the cocktail simulation. This component is estimated considering the full

---

## 6. Elliptic flow of heavy-flavour decay electrons

---

difference observed between the two methods used to calculate the electron background  $v_2$  at low transverse momentum. Also in this case the final systematic error is obtained summing in quadrature the estimates of the different sources.

### 6.2.5 Cocktail simulation method

The background electron  $v_2$  can be estimated using the so-called cocktail method. A cocktail of electron spectra from background sources is calculated using a Monte Carlo event generator of hadron decays and then subtracted from the inclusive electron  $v_2$ . This method requires that the momentum and elliptic flow distributions of the relevant background sources are well known.

The following electron background sources are included in the cocktail simulation:

- Semileptonic decays of  $\pi^0$ ,  $\eta$ ,  $\omega$ ,  $\eta'$ ,  $\phi$
- Leptonic decays of  $\eta$ ,  $\rho^0$ ,  $\omega$ ,  $\eta'$ ,  $\phi$
- Conversion of decay photons from  $\pi^0$ ,  $\eta$ ,  $\rho^0$ ,  $\omega$ ,  $\eta'$
- Real and virtual conversion of prompt and thermal photons

For a consistent treatment with the invariant mass method the contributions from  $K$ ,  $J/\psi$  and  $\Upsilon$  decays to the inclusive electron spectrum are not included in the background cocktail. The  $K$  and  $\Upsilon$  are not expected to be relevant in the  $p_T$  range considered [105].

The  $\pi^0$  plays an important role in the cocktail. The  $p_T$  and  $v_2$  spectra of all particles included in the cocktail are  $m_T$  and  $KE_T$  scaled based on the  $\pi^0$  spectra. In addition the  $\pi^0$  is the dominant electron source contributing via the Dalitz decay of neutral pions ( $\pi^0 \rightarrow e^+e^-\gamma$ ) and via conversion of photons from the decay of  $\pi^0 \rightarrow \gamma\gamma$  in material.

In principle, the parameterization of  $\pi^0$  momentum and  $v_2$  distributions should be based on measured  $\pi^0$  spectra. In ALICE two measurements of the  $\pi^0$   $p_T$  spectrum have been performed. One measuring the

## 6.2 Photonic electron background

---

photon showers inside the Photon Spectrometer (PHOS), and the other by reconstructing the photon conversions in the detector material of the Inner Tracking System (ITS) and the Time Projection Chamber (TPC). Recently the results of both analyses were combined and published [108]. However, because of the much smaller statistical errors of the combined charged pion spectra [109] and the fact that both neutral pion and charged pion spectra are consistent, the average of the charged pion spectra was used for the parameterization, *i.e.*  $\pi^0 = (\pi^+ + \pi^-)/2$ . The difference of the  $\pi^0$  and the  $\pi^\pm$  spectra is considered in the estimation of the systematic uncertainties. For the charged pion elliptic flow there are published ALICE measurements for different transverse momentum regions. At low  $p_T$  ( $p_T < 6$  GeV/c) the scalar product measurements [82] have been used while at higher  $p_T$  ( $3 < p_T < 16$  GeV/c) the event plane results [79] were taken. A parameterization of the pion  $v_2$  distributions up to  $p_T = 16$  GeV/c was used to have a large enough momentum region for this analysis. At  $p_T \sim 13$  GeV/c, only about 10% of the electrons from  $\pi^0$  Dalitz decays is estimated to come from a  $\pi^0$  with  $p_T > 16$  GeV/c, where the elliptic flow of  $\pi^\pm$  is not yet measured in ALICE. To estimate the elliptic flow of electrons from Dalitz decay of  $\pi^0$ , PYTHIA [110] has been used as decay generator. The treatment of electrons from photon conversions in the detector material is done by GEANT4 [111]. It has been implemented in the fast simulation by forcing all decay photons to create electron pairs immediately after creation, skipping the material budget calculation. The result of this method is compared to a low statistic simulation including the material budget, and was found to be consistent.

The contributions of prompt and direct photons have been calculated using the ALICE preliminary measurements [112]. The 0-40 % centrality measurement has been scaled according to the relative scaling factor based on the charged pion spectra at the same centrality classes. The contributions of the different background electron sources are summed according to their relative weights using the additive property of  $v_2$ .

The background  $v_2$  as a function of the measured  $p_T$  from the cocktail simulation ( $0.5 < p_T$  (GeV/c)  $< 13$ ) is shown in Fig. 6.14 together with the invariant mass method results ( $0.5 < p_T$  (GeV/c)  $< 1.5$ ). The elliptic

## 6. Elliptic flow of heavy-flavour decay electrons

flow results measured with the different methods are observed to be in good agreement within the systematic uncertainties in all the three centrality classes analyzed.

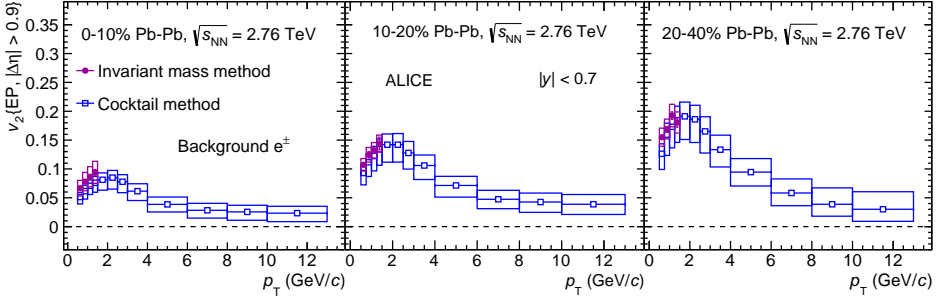


Figure 6.14: Background electron  $v_2$  as a function of  $p_T$  measured with the invariant mass method (dark magenta markers) and with the cocktail simulation (azure markers) in the 0-10% (left), 10-20% (middle) and 20-40% (right) centrality classes in Pb-Pb collisions  $\sqrt{s_{NN}} = 2.76$  TeV

The total systematic errors due to the uncertainties in the cocktail is estimated adding in quadrature the contribution coming from several sources, namely:

- quality of the fits of the spectra
- systematic errors of the  $v_2$  spectra and  $p_T$  of the  $\pi^\pm$
- systematic errors of the  $KE_T$  and  $m_T$  scaling for the higher mass mesons
- $\pi^0$   $p_T$  spectra approximation by the  $\pi^\pm$  spectra

The first one is the dominant one and it is evaluated by parameterizing the data using the upper and lower ends of their statistical and systematic uncertainties added in quadrature. The estimated systematic uncertainty is observed to increase with  $p_T$  reaching a maximum value of 40% at  $p_T \sim$

## 6.2 Photonic electron background

---

12 GeV/ $c$ . The uncertainty on the  $KE_T$  scaling assumption is estimated by comparing the  $v_2$  kaon spectra obtained by  $KE_T$  scaling to the ones measured by the ALICE Collaboration [82]. The resulting systematic uncertainty stays below 10% in all centrality classes. Because of their similar mass it is expected that the flow of  $\eta$  and kaons are comparable and thus these numbers are taken directly for the  $\eta$   $KE_T$  scaling uncertainty. For the other heavier mesons the  $KE_T$  scaling does not work so well [82], however these other particles have an extremely low weight in the cocktail, and thus these uncertainties are considered as higher order uncertainties, which can safely be ignored. In addition to the sources of systematics listed above, two others have been studied. First, reconstructed electron candidates have a limited  $p_T$  resolution. In particular Bremsstrahlung in the detector material shifts their reconstructed  $p_T$  towards lower values. Secondly, hits in the SPD can be incorrectly associated to a track with a probability decreasing with  $p_T$ . Both effects have been evaluated in the cocktail and no significant change of the background  $v_2$  has been found. More details are on these two systematic contributions are reported in the next section.

### 6.2.6 Late photon conversions

During the track refitting to the primary vertex, the tracking associates new ITS clusters to a track candidate, and the track parameters are more refined. In this procedure if the associated cluster did not belong to that track itself, tracks produced far away from the collision point have non-zero probability to be tracked back to the reconstructed primary vertex, thus being reconstructed as primary.

For this analysis the only contributions due to the fake cluster assignment are the electrons from  $\gamma$  conversions, because they are produced everywhere in the detector and can be reconstructed as primary tracks. Almost all the electrons coming from  $\pi^0$  and  $\eta$  Dalitz decays are produced and reconstructed very close to the primary vertex (within 1 cm). This effect is very surprising since a hit in both the SPD layers is required, a constraint that should completely remove all electrons from conversions after the first layer in the SPD. The effect is observed to be well reproduced in the MC

## 6. Elliptic flow of heavy-flavour decay electrons

---

simulations, where it is possible to discriminate between electrons from  $\gamma$  conversions that are sharing clusters in the ITS detector and are produced at large radii.

Electrons from late conversions have a poor momentum resolution as well as a systematic shift ( $\sim 5\%$ ) in  $p_T$  and azimuthal angle. The effect is more pronounced in the low transverse momentum region. The momentum shift and poor resolution are responsible of the unexpected peak structure observed in the LS pair distribution (Fig. 6.9) for small invariant mass values. The LS peak is observed to be more significant at low  $p_T$  and the structure starts to disappear at higher momenta. The peak structure is observed in all the centrality classes and it is more significant in most central events where the track density in the ITS is higher, increasing the probability of cluster sharing. The LS peak structure is also reproduced in the MC, and it is seen only for pairs in which at least one track is sharing cluster in the ITS layers. As for true ULS pairs, a systematic shift to higher mass values of the mean of the photonic peak has been observed for pairs produced at large radii; which is the reason why conversion electrons display a lower invariant mass reconstruction efficiency with respect to electrons coming from  $\pi^0$  Dalitz decay.

The number of shared clusters in the ITS and the  $\tilde{\chi}^2$  in the ITS normalized to the number of cluster in the detector itself have been tested in order to suppress the fraction of electrons coming from conversions at large radii. These variables show a strong dependence on the production radius of the electron. Tracks produced at large radii show a broad  $\tilde{\chi}^2$  distribution (almost flat) extending up to large  $\tilde{\chi}^2$  values. Tracks produced close to the primary vertex show a steep distribution peaked at small  $\tilde{\chi}^2$ . The effectiveness of those cuts in suppressing electrons produced by  $\gamma$  conversions at large radii is investigated looking at the fraction of electrons produced with a  $R > 5$  cm. Those distribution are reported in the left and right panel of Fig. 6.15 for the 0-10% and 20-40% centrality classes respectively.

Without the introduced ITS cut variables (black markers) the fraction of electrons coming from conversion at large  $R$  is  $\sim 70\%$  ( $\sim 60\%$ ) at low transverse momentum, while at higher  $p_T$  the contribution decreases down to  $\sim 20\%$  ( $\sim 10\%$ ) in the 0-10% (20-40%) centrality interval. Stronger se-

## 6.2 Photonic electron background

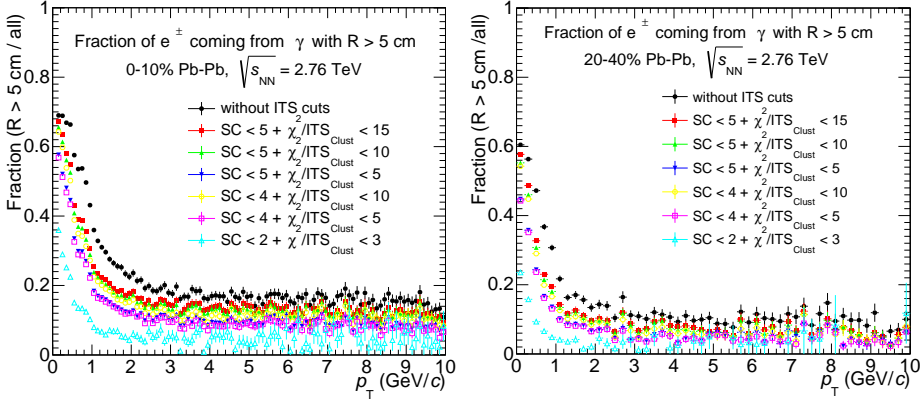


Figure 6.15: Fraction of electron for  $R > 5$  cm for different combination of the additional ITS cuts (the number of shared cluster and the  $\chi^2$  in the ITS) in 0-10% (left) and in 20-40% (right).

lections reduce the fraction of selected electrons at large radii, nevertheless even with the very strong cuts applied, the electrons from late conversions are not totally removed at low  $p_T$ .

The effect of the cuts is also investigated looking at the electron conversion radius distribution. In the right panel of Fig. 6.16 the number of electrons ( $p_T$ -integrated) as a function of their conversion radius is reported for different sets of ITS cuts. The figure shows the 10% most central events, where the track density effect is higher. Applying stronger ITS cuts the number of electrons from conversions is strongly suppressed at large radii, while for small  $R$  the cuts are less effective.

In the right panel of Fig. 6.16 the effect on all electrons, including the one from  $\pi^0$  and  $\eta$  Dalitz decays, is shown. The electrons coming from Dalitz decays populate the region at very small  $R$ , and they are almost not affected by the ITS cuts. It confirms that the electrons coming from heavy-flavour, which are primary tracks, should almost not be affected by those additional ITS requirements. Also the peak structure in the like-sign invariant mass distribution is observed to disappear when stronger and stronger cuts are

## 6. Elliptic flow of heavy-flavour decay electrons

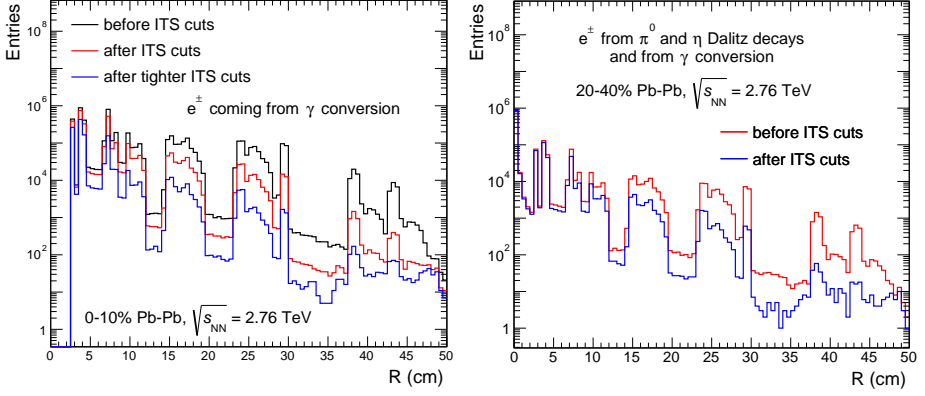


Figure 6.16: Distribution of the number of electron as a function of their production radius. In the right panel the distributions are reported only for conversion electrons for different combinations of the additional ITS cuts in 0-10% centrality class. In the left panel the distribution is reported also including electrons from  $\pi^0$  and  $\eta$  Dalitz decays.

applied.

The additional ITS cuts have been studied also for the elliptic flow coefficient of the inclusive and background electrons. The  $v_2$  in both cases has been observed to decreases for  $p_T < 1.5$  GeV/c, a  $\sim 20\%$  difference is observed in most central collisions and a  $\sim 10\%$  difference in peripheral. Above  $p_T \sim 1.5$  GeV/c the contribution is observed to be negligible. On the inclusive over background ratio no difference has been observed. However, a slight increase at low  $p_T$  in the efficiency of the electrons from conversions has been observed when the new ITS cuts are used.

A possible bias has been investigated for the cocktail simulation as well. Since the cocktail uses only the mother particle spectra and does not include detector effects, the resolution effects are not considered. A consistent treatment of the resolution has been studied by degrading the resolution in the cocktail simulation according to response matrixes for the  $p_T$  and azimuthal angle extracted from the MC productions with a full simulation of

### 6.3 Heavy-flavour decay electrons measurements

---

the ALICE apparatus. Those matrixes are used to smear the  $p_T$  and azimuthal angle in the cocktail in order to simulate electrons produced from conversions at large radii. This has been implemented into the cocktail by decreasing the resolution artificially increasing the conversion electrons with the estimated fraction shown in Fig. 6.15 before the extraction of the cocktail measurements. No significant effect has been observed in the cocktail simulation.

Since the same discrepancy is observed at inclusive and at background electron  $v_2$  level when the additional ITS cuts are applied, the effect on the heavy-flavour decay electrons  $v_2$  is negligible due to the subtraction procedure. The additional ITS cuts are not applied for the default results and no systematic uncertainties have been assigned to the heavy-flavour decay electrons measurements in all the centrality classes.

### 6.3 Heavy-flavour decay electrons measurements

In Fig. 6.17 the elliptic flow of electrons from heavy-flavour hadron decays,  $v_2^{e \leftarrow HF}$ , is plotted as a function of the transverse momentum ( $0.5 < p_T < 13$  GeV/c) for most central 0-10% (left panel), mid-peripheral 10-20% (middle panel) and semi-peripheral 20-40% (right panel) Pb-Pb collisions at  $\sqrt{s_{NN}} = 2.76$  TeV. The  $v_2$  coefficient is extracted using the three sub-event plane methods with  $\Delta\eta > 0.9$ .

The results extend the heavy-flavour  $v_2$  measurements already performed by the ALICE Collaboration towards lower transverse momentum. The prompt D meson  $v_2$  [37] and heavy-flavour decay muon  $v_2$  [38] are measured in the  $p_T$  interval 2–16 GeV/c and 3–10 GeV/c, respectively. Moreover charm hadron decays are expected to mainly contribute to the heavy-flavour decay electron sample at low  $p_T$  ( $p_T \leq 3$  GeV/c), whereas at higher  $p_T$  the contribution from beauty hadron decays should start to dominate. Therefore the measurement of heavy-flavour decay electron  $v_2$  provides further inputs on the beauty and charm elliptic flow at mid rapidity to theoretical calculations which aim at describing the heavy-quark interactions with the medium. At low  $p_T$  the systematic uncertainties are large due to the small

## 6. Elliptic flow of heavy-flavour decay electrons

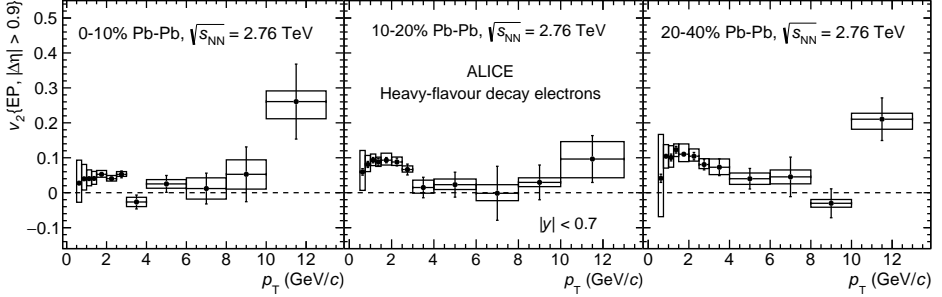


Figure 6.17: Elliptic flow of electron from heavy-flavour decays,  $v_2^{e^\pm \leftarrow HF}$ , in  $|y| < 0.7$  for various centrality intervals, in Pb-Pb collisions at  $\sqrt{s_{NN}} = 2.76$  TeV as function of the transverse momentum. The symbols are placed at the centre of the  $p_T$  interval. The vertical error bars represent the statistical uncertainty, the horizontal error bars correspond to the size of the  $p_T$  bin and the open boxes are the systematic uncertainties. The results are measured with the event plane method.

signal-to-background ratio. In all centrality intervals the  $v_2$  of heavy-flavour decay electrons is slightly increasing with  $p_T$  up to a  $p_T$  of 1.5 GeV/c where it reaches a maximum. A positive  $v_2$  is observed in all centrality classes, with a significance of  $5.9 \sigma$  in the  $p_T$  interval 2–2.5 GeV/c in semi-central collisions (20–40%), combining statistical and systematic uncertainties. At higher  $p_T$  the measured  $v_2$  of heavy-flavour decay electrons exhibits a slight decrease as  $p_T$  increases, being consistent within large uncertainties with zero for  $p_T$  greater than 4 GeV/c. This trend reflects the interplay between scatterings with the constituents of an expanding medium at low and intermediate  $p_T$  and the path-length dependence of the parton energy loss in the hot and dense matter at high  $p_T$ . For  $p_T > 6$  GeV/c the large statistics and systematic error bars do not allow to draw any strong physics conclusion.

Figure 6.18 shows the centrality dependence of the elliptic flow of heavy-flavour decay electrons in two  $p_T$  intervals (1.25–1.5 GeV/c and 2.5–3 GeV/c). In the  $p_T$  range  $1.25 \leq p_T \leq 1.5$  GeV/c the contribution from charm hadron decays is expected to be dominant in the heavy-flavour decay electron sam-

### 6.3 Heavy-flavour decay electrons measurements

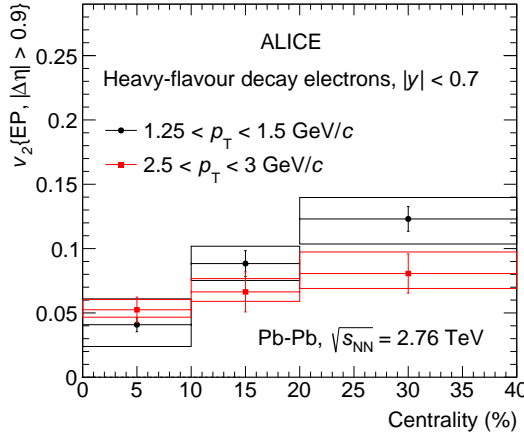


Figure 6.18: Elliptic flow of electron from heavy-flavour decays,  $v_2^{\epsilon\pm \leftarrow HF}$ , in  $|y| < 0.7$  as a function of the centrality class in Pb–Pb collisions at  $\sqrt{s_{NN}} = 2.76$  TeV. The symbols are placed at the centre of the centrality interval. The vertical error bars represent the statistical uncertainty, the horizontal error bars correspond to the size of the centrality bin and the boxes are the systematic uncertainties.

ple, whereas in the higher  $p_T$  interval the beauty hadron decays should start to be relevant. A significant decrease of the  $v_2$  magnitude towards central collisions is observed. This is consistent with a final state anisotropy driven by the initial geometrical anisotropy of the nucleons participating in the collision, which increases with its centrality. This suggests, together with the positive  $v_2$  of heavy-flavour decay electrons, that heavy quarks, mainly charm, participate in the collective expansion of the medium and confirms that they undergo significant interactions with the medium’s constituents.

At forward rapidity ( $2.5 \leq y \leq 4$ ), the elliptic flow of heavy-flavour decay muons has been measured with various methods in the centrality classes 0-10%, 10-20% and 20-40% [38]. Figure 6.19 shows the comparison between the elliptic flow of heavy-flavour decay electrons at mid rapidity and the one of heavy-flavour decay muons at forward rapidity in semi-central

## 6. Elliptic flow of heavy-flavour decay electrons

(20-40%) Pb-Pb collisions. The two-particle  $Q$ -cumulant method with a pseudo-rapidity gap larger than 1.7 was used to extract the  $v_2$  of heavy-flavour decay muons. The observed  $v_2$  of heavy-flavour decay leptons is similar at mid and forward rapidity.

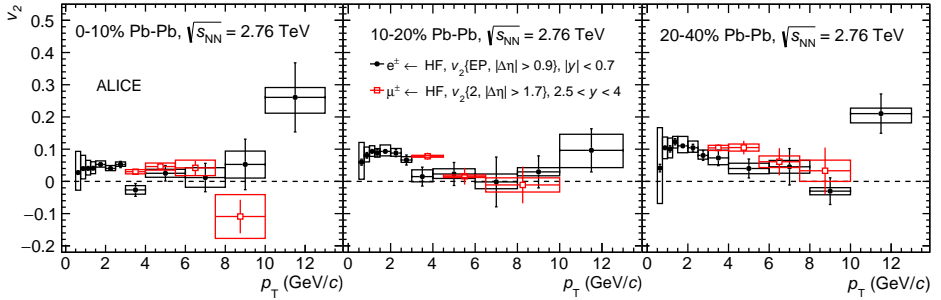


Figure 6.19: Elliptic flow of heavy-flavour decay electrons at mid rapidity ( $|y| \leq 0.7$ ) (black markers) compared to the elliptic flow of heavy-flavour decay muons at forward rapidity [38] ( $2.5 \leq y \leq 4$ ) (red markers) in the 20-40% centrality classes in Pb-Pb collisions at  $\sqrt{s_{NN}} = 2.76$  TeV. The symbols are placed at the centre of the centrality interval whose width is shown by the horizontal error bar. The vertical error bars and open boxes represent the statistical and systematic uncertainties, respectively.

**Uncertainties propagation** The error propagation for the background subtraction is based on an approximation of a second order error propagation [113, 114], where differently from the Gaussian approximation, not only linear effects of the error propagation are considered but also quadratic effects. This is necessary especially in case the systematic errors are large and where the non-linearity of the subtraction cannot be neglected anymore. The basic concept is that the statistical errors  $\sigma^{stat}(v_2^{e^{\pm} \leftarrow HF})$  as well as the upper/lower systematic errors  $\sigma_{\pm}^{sys}(v_2^{e^{\pm} \leftarrow HF})$  are both found by independently varying the errors of the input variables,  $E(R_{SB})$ ,  $E(v_2^{incl})$  and  $E(v_2^{backgr})$ , by one sigma ( $\sigma^{stat}$  or  $\sigma_{\pm}^{sys}$ ) up/down. The Gaussian ap-

### 6.3 Heavy-flavour decay electrons measurements

proximation has been tested summing in quadrature the relative systematic uncertainty of the different input variables, and the systematic uncertainties obtained under this approximation are found to be compatible with the default strategy adopted.

#### 6.3.1 Model comparison

Several theoretical model calculations are available for the elliptic flow coefficient  $v_2$  of heavy-flavour hadrons and their decay leptons.

Figure 6.20 shows the comparison of the measured heavy-flavour decay electron elliptic flow in the 20-40% centrality class with different theoretical model calculations.

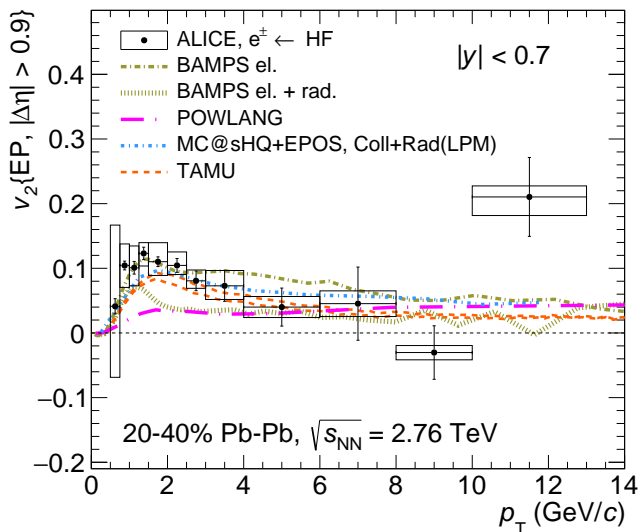


Figure 6.20: Heavy-flavour decay electrons  $v_2$  as a function of  $p_T$  in comparison with and model calculation including interactions of the  $c$  and  $b$  quarks with a hot, dense and deconfined medium. can qualitatively describe the data within uncertainties.

## 6. Elliptic flow of heavy-flavour decay electrons

---

The elliptic flow of heavy-flavour decay electrons is qualitatively described by the models including significant interactions of heavy quarks with a hydrodynamically expanding QGP. Mechanisms, like collisional processes and hadronization via recombination, which transfer to heavy quarks and heavy-flavour hadrons the elliptic flow generated during the system expansion, are required to reproduce the measured positive  $v_2$  of heavy-flavour decay electrons. Models that do not include a collective expansion of the medium or lack a contribution to the hadronization of charm quarks from recombination with light quarks from the medium (POWLANG and BAMPS el. + rad) predict in general a smaller anisotropy than observed in the data. It has been observed that those model underestimate as well the elliptic flow of prompt D mesons at mid rapidity [37] indicating that the results are consistent with each other. Similar observations were done at forward rapidity for the heavy-flavour decay muons [38].

---

## Chapter 7

# Elliptic flow of direct photons

---

Since the azimuthal anisotropy of direct photons depends strongly on their production mechanism, a measurement of elliptic flow allows to put additional constraints on their production time. Small flow would be associated with early production while a large, hadron-like flow would point towards late production. Similar to the heavy-flavour decay electrons analysis, the elliptic flow of direct photons  $v_2^{\gamma,dir}$  is obtained from the measurement of inclusive photons,  $v_2^{\gamma,inc}$ , by subtracting all photons from hadron decays,  $v_2^{\gamma,Background}$  as:

$$v_2^{\gamma,dir} = \frac{R_\gamma v_2^{\gamma,inc} - v_2^{\gamma,Background}}{R_\gamma - 1} \quad (7.1)$$

with  $R_\gamma = N_{\gamma,inc} / N_{\gamma,Background}$ . In the ALICE collaboration the preliminary measurements of direct photon elliptic flow has been measured using the event plane method [112]. In this chapter a new and independent

analysis is reported in which the scalar product method has been used to measure the elliptic flow coefficient in order to spot and remove possible ambiguities and experimental biases in the results introduced by the event plane method [77].

### 7.1 Inclusive photon reconstruction

Photons traveling through the detector has a non zero probability to convert in the material. In this thesis photons are reconstructed via their conversion products using a secondary vertex finder (V0 finder). A detailed description of the reconstruction technique can be found in [108, 115]. The neutral particles that can be reconstructed using the V0 method are  $\Lambda$  ( $\bar{\Lambda}$ ) and  $K_s^0$  decays and  $\gamma$  from conversions. In the following sections, the track cuts, the electron identification, the secondary vertex and photon reconstruction cuts are described.

#### 7.1.1 Electron identification

Particle identification (electron selection and pion rejection) has to be applied on the reconstructed V0 candidates ( $\gamma$ ,  $K_s^0$ ,  $\Lambda$  ( $\bar{\Lambda}$ )) decay products, in order to select only electrons that will be used for the photon reconstruction procedure. The identification of electrons in this analysis relies mainly on the  $dE/dx$  measurement in the TPC. In addition to the TPC  $dE/dx$  cuts, a  $5\sigma$  inclusion around the electron hypothesis in the TOF is used to further remove the hadronic background sources. However, since not all of the secondary tracks originating from the photon candidates reach the TOF, this cut is used only if the track can be matched to a signal in the TOF detector. The standard cuts for this analysis are TPC- $N\sigma$  between -3 and 5 and TOF- $N\sigma$  between -5 and 5. In addition, the pion contamination in the region, where the  $dE/dx$  curves start to overlap, is further reduced by removing all tracks within TPC- $N\sigma$  between -10 and 3 with respect to the expected pion energy loss for transverse momenta above 0.4 GeV/c.

## 7.1 Inclusive photon reconstruction

---

### 7.1.2 Topological cut selection

The decay (or conversion in case of  $\gamma$ ) topology is sketched in the right panel of Fig. 7.1. The reconstruction procedure starts with the selection of two oppositely charged secondary tracks. The impact parameters of the tracks ( $b, b^+$ ) with respect to the primary vertex are calculated. Tracks with a too small impact parameter are discarded according to the definition of primary tracks. Tracks were selected in the mid-rapidity region with a  $|\eta| < 0.8$  to ensure a uniform acceptance and efficiency in the TPC. It is required that the secondary tracks, coming from the secondary vertex  $V^0$ , have no kinks and fulfill the TPC refit condition, as well as the requirement of having at least 70 associated cluster in the TPC. Afterwards the distance of closest approach (DCA) in space between both tracks is calculated. The track pair is rejected if the measured DCA is larger than 1 cm.

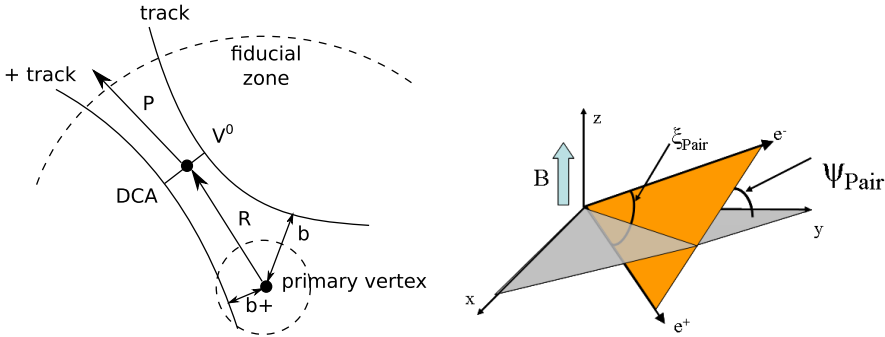


Figure 7.1: Left: representation of the  $V^0$  vertex topology, figure taken from [61]. Right panel: representation of the  $\Psi_{pair}$  angle as the angle between the plane of the electron and positron pair (colored in orange) and the bending plane of the magnetic field (in gray). The magnetic field is parallel to the beam pipe, which is represented by the  $z$  axis, figure taken from [116].

Based on the invariant mass of the  $e^+e^-$  pair and the pointing of the

## 7. Elliptic flow of direct photons

---

V0 to the primary vertex, the vertex finder calculates a  $\tilde{\chi}_\gamma^2$  value which reflects the level of consistency with the hypothesis that the V0 comes from a photon originating from the primary interaction. A cut on the  $\tilde{\chi}_\gamma^2$  value is applied at 30 to further reduce contamination in the photon sample. As for the single electron tracks also for the reconstructed photons a pseudo-rapidity cut is imposed ( $|\eta| < 0.8$ ). Their point of closest approach (DCA) is displaced from the primary vertex by a radius  $R$ , and their four momenta at this point add up such that the mother particle momentum vector  $P$  points towards the primary vertex. The momenta of both daughter tracks are extrapolated to the DCA and their sum is calculated as the particles momentum at the secondary vertex. A cut of 0.85 on the cosine of the angle between the reconstructed V0 momentum ( $P$ ) and the vector connecting the primary and secondary vertices is applied. To ensure the reconstruction of the secondary tracks in the TPC, secondary vertices with  $R_{Conv} > 180$  cm and  $Z_{Conv} > 240$  cm are rejected. Furthermore, all V0 candidates are required to have a  $R_{Conv} > 5$  cm to reduce the contamination from  $\pi^0$  and  $\eta$  Dalitz decays. The di-lepton momenta are almost parallel at the conversion point with no preferred direction of emission in azimuthal angle  $\varphi$  or polar angle  $\theta$  direction. As the particles propagate in the magnetic field, their opening angle in the transverse plane  $\Delta\varphi = \varphi^{e^+} - \varphi^{e^-}$  increases due to the curvature of the tracks, while the opening angle in the polar direction  $\Delta\theta = \theta^{e^+} - \theta^{e^-}$  stays constant. The situation is sketched in the right panel of Fig. 7.1. The angle  $\Psi_{pair}$  between the plane spanned up by the dilepton momenta, evaluated propagating the tracks at 50 cm from the production point, and the bending plane of the magnetic field is defined as

$$\Psi_{pair} = \arcsin\left(\frac{\Delta\theta}{\xi_{pair}}\right), \quad (7.2)$$

where  $\xi_{pair}$  is

$$\xi_{pair} = \frac{\vec{p}^+ \cdot \vec{p}^-}{|\vec{p}^+| \cdot |\vec{p}^-|}. \quad (7.3)$$

Therefore,  $\Psi_{pair}$  is the arcsine of the ratio between the difference of the angles of the two daughter tracks with the z-axis and the angle between the

## 7.1 Inclusive photon reconstruction

propagated daughter tracks. The default cut applied in this analysis consist of rejecting pairs if the calculated  $\Psi_{pair}$  is larger then 0.1 rad.

The left panel of Fig. 7.2 shows an Armenteros-Podolanski plot [117] for secondary vertices (without any selection cuts) for the 0-10% most central events in Pb-Pb collision at  $\sqrt{s_{NN}} = 2.76$  TeV.  $\alpha$  is the momentum asymmetry defined as:

$$\alpha = \frac{p_L^+ - p_L^-}{p_L^+ + p_L^-}, \quad (7.4)$$

where  $p_L^+$  and  $p_L^-$  are the longitudinal components of the total momentum for the positive and negative daughters, respectively, relative to the direction of the V0 momentum vector, and  $q_T$  is the transverse momentum component of the daughter momentum with respect to the V0 momentum defined as:

$$q_T = p_{daughter} \times \sin(\varphi_{mother} - \varphi_{daughter}). \quad (7.5)$$

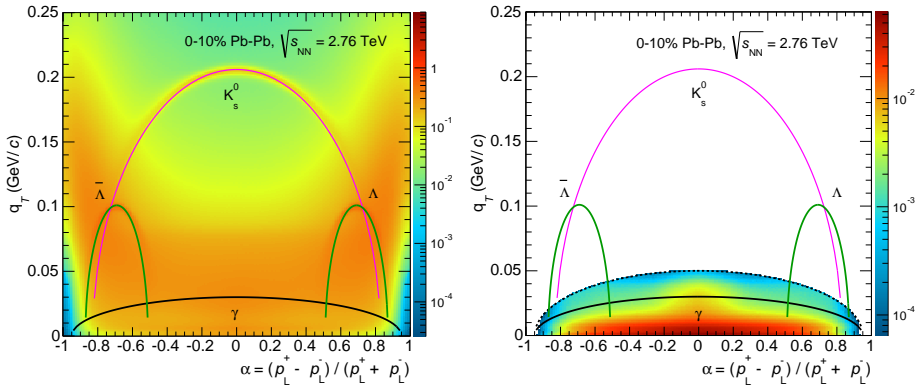


Figure 7.2: Armenteros-Podolanski plot for the 0-10% central Pb-Pb collisions of the remaining photon candidates before (left) and after (right) that all electron identification and photon reconstruction cuts have been applied. The coloured lines indicate the position of the V0 candidates [93].

## 7. Elliptic flow of direct photons

---

The relativistic particles coming from the physical decay lie on an ellipse due to energy and momentum conservation. The analytical expression for this particle in the  $(\alpha, q_T)$  plane, after setting daughters and mother particle masses  $m_1$ ,  $m_2$  and  $M$  respectively, is given by:

$$\left(\frac{\alpha - a}{b}\right)^2 + \left(\frac{q_T}{q_{T,\max}}\right)^2 = 1, \quad a = \frac{m_1^2 - m_2^2}{M^2}, \quad b = \frac{2q_{T,\max}}{\beta M} \quad (7.6)$$

where  $q_{T,\max}$  is the maximum possible momentum transfer of the daughter in the centre of mass. In addition to photon conversions, also the bands from the symmetric decay  $K_s^0 \rightarrow \pi^+\pi^-$  and the asymmetric decays of  $\Lambda \rightarrow \pi^-p$  and  $\bar{\Lambda} \rightarrow \bar{p}\pi^+$  are visible. For  $K_s^0$  and  $\gamma$ , since the decay products are of identical mass the  $a$  parameter is equal to zero and the ellipse is centered at the origin of the coordinate space, while for the  $\Lambda$  ( $\bar{\Lambda}$ ) the two bands are centered around  $\alpha = \pm 0.7$  respectively due to the mass difference of the decay products. The lines shown represent the different parameterization of the  $\gamma$ ,  $K_s^0$ ,  $\Lambda$  ( $\bar{\Lambda}$ ) decays in which the values of the parameters  $a$  and  $b$  are calculated taking inputs from [93]. The photons converting to  $e^+e^-$  in the detector material are distributed symmetrically in  $\alpha$  and are located in the low  $q_T$  region due to the small di-lepton opening angle. The right panel of Fig. 7.2 shows this distribution after all electron identification and reconstruction photon cuts have been applied. In the ALICE preliminary measurements of the direct photon  $v_2$  [112] and on the published  $p_T$  spectra [108] a straight cut at  $q_T = 0.05$  GeV/ $c$  was used. In this analysis a more sophisticated 2-dimensional elliptic cut, represented by the black dashed line in the right panel of Fig. 7.2, allows for an optimal separation of the photons from the remaining V0s. This parameterization is obtained that at  $\alpha = 0$  the  $q_T$  max accepted is equal to 0.05 GeV/ $c$ .

## 7.1 Inclusive photon reconstruction

---

### 7.1.3 Purity and efficiency

The performance of the photon reconstruction is characterized by an efficiency,  $\epsilon$ , and a purity,  $p$ , which are defined as:

$$\epsilon = \frac{N_{true,found}^{\gamma}}{N_{true}^{\gamma}}, \quad (7.7)$$

$$p = \frac{N_{true,found}^{\gamma}}{N_{found}^{\gamma}}. \quad (7.8)$$

The photon purity and efficiency are calculated in a Monte Carlo simulation based on HIJING including the full ALICE detector description, with the same selection cuts as for data. Figure 7.3 shows the photon efficiency (left panel) and purity (right panel) as a function of the transverse momentum of the  $\gamma$  for different centrality intervals.

Both, purity and efficiency, depend strongly on the photon selection cuts. The efficiency accounts for the fraction of photons that cannot be reconstructed due to inefficiencies in the track and V0 finding algorithm or due to detector acceptance and the application of particle identification cuts. The purity is the fraction of reconstructed photons, which can be assigned to true photons. In other words,  $(1 - p)$  is fraction of combinatorial background and contamination from  $\Lambda$  and  $K_s^0$  decays, which passes the selection cuts.

The photon reconstruction efficiency is about 45% at intermediate  $p_T$  and decreases towards lower momenta, since the track reconstruction efficiency deteriorates. At high  $p_T$ , the efficiency slightly decreases, since the separation power and thus the efficiency of the particle identification cuts decreases. The efficiency is some percent larger in mid-central compared to peripheral collisions due to the smaller detector occupancy. The photon purity at intermediate  $p_T$  is reaching about 95% for central and 99% in mid-central collisions. The purity is poorer at low  $p_T$  due to combinatorial background of photon candidates reconstructed at small radii  $R_{conv}$  in the ITS layers, where the track densities are very large.

## 7. Elliptic flow of direct photons

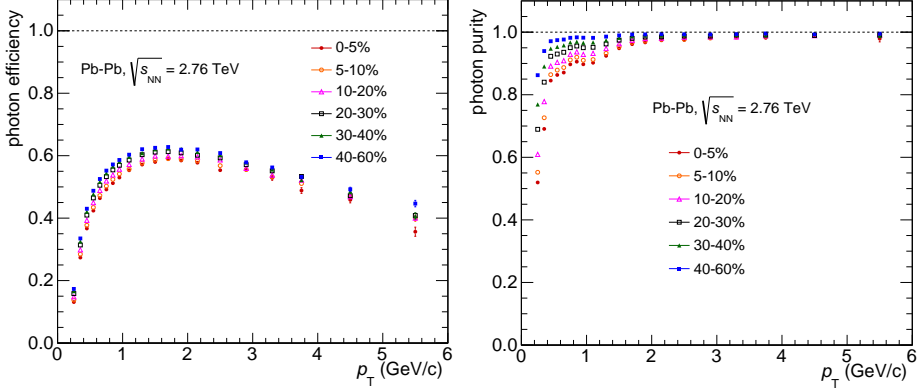


Figure 7.3: (left) Photon efficiency and (right) purity as a function of  $p_T$  for different centrality classes in Pb-Pb collision at  $\sqrt{s_{NN}} = 2.76$  TeV.

The different composition of the accepted pairs not coming from a real photon conversion process has been investigated in a MC. The largest fraction of combinatorial background is found to come from  $e^+e^-$  pairs not originating from the same parent ( $\sim 8\%$  up to  $p_T \leq 1$  GeV/c) and from pairs in which an electron track is correlated to a misidentified  $\pi/K/p$  track (4-5% up to  $p_T \leq 1$  GeV/c).

### 7.1.4 Inclusive photon $v_2$

In Fig. 7.4 the inclusive-photon elliptic flow as a function of the transverse momentum for different centrality ranges is shown. The measurements have been performed with the scalar product (red markers) and with the event plane method (black markers), using in both cases the three sub event technique described in section 3.2.1 and 3.1.1 respectively. The two methods provide compatible results, showing that there are no different biases in both methods. A pseudo-rapidity gap of 0.9 units has been imposed in both methods to suppress non-flow contributions to the measured  $v_2$ .

## 7.1 Inclusive photon reconstruction

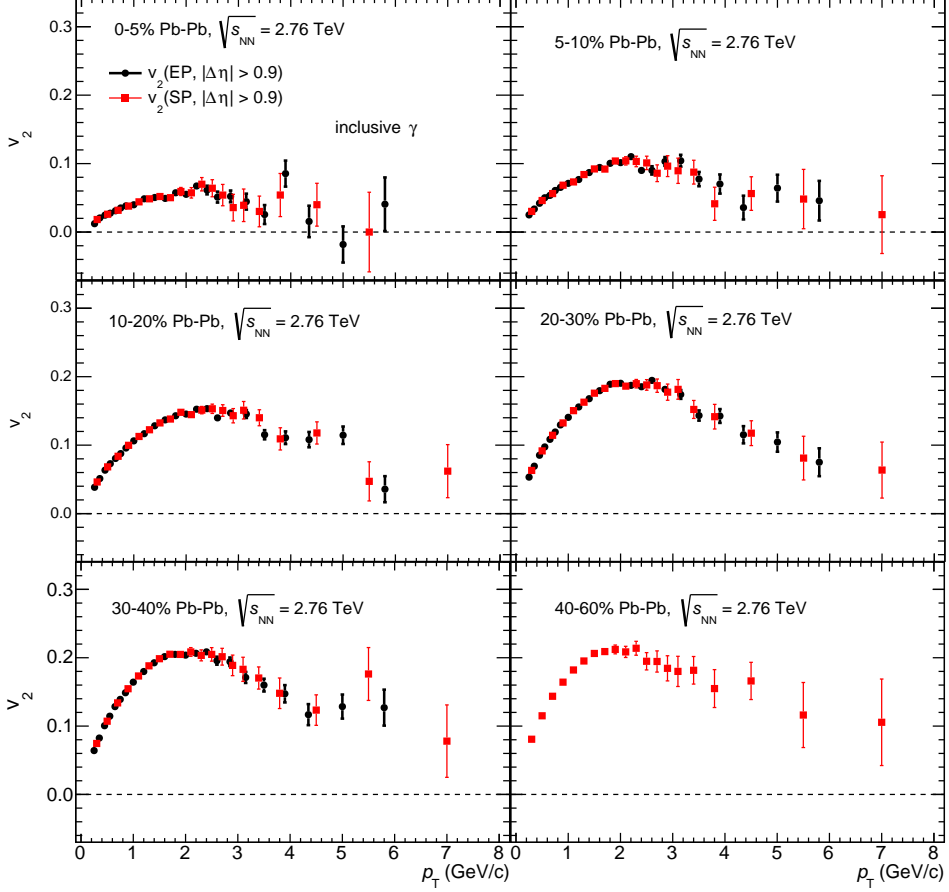


Figure 7.4: Comparison of the  $p_T$ -differential elliptic flow of inclusive photon measured with the scalar product (red markers) and with the event plane (black markers) methods in different centrality intervals in Pb-Pb collisions at  $\sqrt{s_{NN}} = 2.76$  TeV. In both measurements the same pseudo-rapidity gap of 0.9 unit is imposed.

---

## 7. Elliptic flow of direct photons

---

At low and intermediate  $p_T$  ( $p_T < 2.5/3$  GeV/ $c$ ) the results show an increase of  $v_2$  from central to peripheral events, while at higher  $p_T$  the elliptic flow decreases to zero. Since no differences with the scalar product method have been observed at the inclusive photon  $v_2$  level, in the rest of this chapter only the ALICE preliminary results obtained with the event plane method are reported [112].

### 7.1.5 Systematic uncertainties

Uncertainties related to track selection and electron identification were estimated by variation of the cuts. Systematic uncertainties on the inclusive photon  $v_2$  are estimated by the root mean square of results obtained by different selection cuts. For instance, uncertainties related to the tracking of low momentum particles were estimated by increasing the minimum  $p_T$  for electron tracks from 50 MeV up to 100 MeV. Since the photon yields are not corrected for efficiency and purity, a variation of the photon selection cuts also introduces small changes in both quantities and deviations allow to estimate the magnitude of possible contamination effects. Since local track densities become smaller at larger conversion radii, a significantly higher purity can be achieved by neglecting conversions in the first layers of the ITS material. Thus, the minimum conversion radius is varied from  $R_{min} = 5$  cm up to  $R_{min} = 10$  cm, corresponding to a removal of photons reconstructed in the firsts ITS layers. A variation in the Armenteros-Podolanski selection has been tested by tightening the maximum  $q_T$  accepted to 0.03 GeV/ $c$  in the photon parameterization and also applying a flat cut in  $\alpha$ , as used in previous analysis. The variation of all aforementioned photon selection cuts gives the dominant contribution to the total systematic uncertainty and they reach a maximum of about 10% at high transverse momentum.

The estimate of the systematic uncertainty of the electron selection includes a contribution estimated by the variation of the TPC  $dE/dx$  cuts. An additional electron identification selection has been studied. As for the heavy-flavour decay electron measurements, the particle identification based on the specific  $dE/dx$  in the ITS has been tested. This approach has been recently studied in the analysis to further suppress mainly the contamina-

## 7.2 Photon conversion background

---

tion of misidentified kaons and protons. Their contribution, even if small, has been observed in MC studies to contribute to the background pairs. The default electron selection in the ITS used in this analysis consist of selecting TPC electron candidates if their ITS- $N\sigma$  is between -2 and 2. The ITS requirements is imposed up to a  $p_T$  of 2 GeV/ $c$ . A maximum variation of 5% is observed in the 0-5% and 5-10% centrality classes where the contamination is estimated to be larger. In more peripheral collision the effect is estimated to be smaller than 2%.

The inclusive photon  $v_2$  in the 0-40% centrality class is calculated from the measurements in small centrality bins (Fig. 7.4) using the transverse momentum spectra as weight. Since the efficiency and purity are observed (Fig. 7.3) to slightly depend on the centrality, as a cross check, the purity and efficiency corrected yield is used as a weight in averaging the  $v_2$  from narrower centrality classes. Except for the low- $p_T$  point, this has been observed to be a rather small contribution of 2%. The different contributions have been added in quadrature in order to evaluate the total systematic uncertainty.

## 7.2 Photon conversion background

### 7.2.1 Photon background $v_2$

The decay-photon spectrum and its elliptic flow are estimated via the cocktail simulation as it was done in the case of the heavy-flavour decay electron analysis. Also in this case the dominant fraction of decay photons comes from the neutral pion decay. As described in detail in section 6.2.5, the neutral pion cocktail spectra and  $v_2$  are obtained via parameterizations of the measured neutral and charged pion spectra and  $v_2$  [79, 82, 108, 109]. The spectra of other hadrons are estimated from  $m_T$  scaling, while the anisotropies are estimated according to the  $KE_T$  scaling. The azimuthal anisotropy of the decay photons is determined by the anisotropy of the mother hadrons and the decay kinematics, where the decay kinematics are simulated by PYTHIA [110]. The total systematic uncertainty is calculated as the square root of the quadratic sum of all contributions already pre-

## 7. Elliptic flow of direct photons

sented in section 6.2.5 and the systematic uncertainties are estimated to be of the same magnitude.

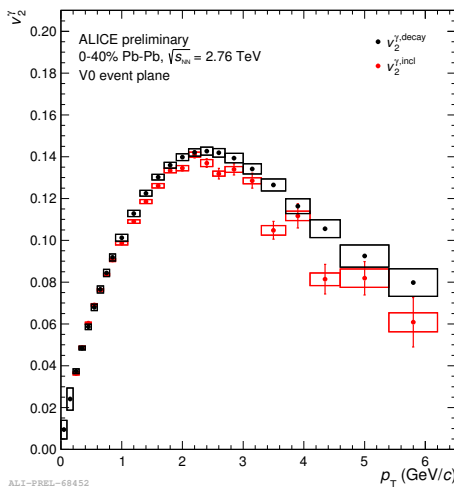


Figure 7.5: Comparison of the  $p_T$ -differential elliptic flow of inclusive (red markers) and decay photon (black markers) in 0-40% central Pb-Pb collisions at  $\sqrt{s_{NN}} = 2.76$  TeV.

Figure 7.5 shows a comparison of the measured inclusive-photon (measured with the event plane method) and the corresponding estimated decay-photon elliptic flow in 0-40% central Pb-Pb collisions at  $\sqrt{s_{NN}} = 2.76$  TeV [112]. At larger momenta,  $v_2^{\text{inc}}$  tends to be smaller than  $v_2^{\text{Background}}$ , which can be explained by a contribution of direct photons with a smaller  $v_2$  than the decay photons. Such a behavior is expected from the dominance of next-to-leading-order pQCD photons, which are mostly emitted before equilibration of the quark-gluon plasma and thus have zero azimuthal anisotropy. At low  $p_T$ , the agreement between the anisotropy of inclusive and decay photons could indicate that the inclusive photon measurements are dominated by the decay-photon background or that direct-photon  $v_2$  is in magnitude compared to the inclusive-photon flow.

## 7.2 Photon conversion background

---

### 7.2.2 Double ratio

The direct photon yield is extracted on a statistical basis by comparing the measured inclusive photon spectrum to the spectrum of photons from hadronic decays [49]. The yield of  $\pi^0$ s, which contribute up to  $\sim 80\%$  of the decay photons, was measured simultaneously with the inclusive photon yield. In addition to photons from  $\pi^0$  decays, the second and third most important contributions to the decay photon spectrum comes from  $\eta$  and  $\omega$  decays.

An excess of direct photons above the decay photon spectrum can be quantified by the double ratio:

$$R_\gamma = \frac{N_{\gamma,inc}}{N_{\gamma,Background}} = \frac{N_{\gamma,inc}/N_{\pi^0}}{N_{\gamma,Background}/N_{\pi^0}}, \quad (7.9)$$

where  $N_{\gamma,inc}$  is the measured inclusive photon spectrum,  $N_{\pi^0}$  a parameterization of the measured  $\pi^0$  spectrum, and  $N_{\gamma,Background}$  the calculated decay photon spectrum using a cocktail simulation. The double ratio has the advantage that some of the largest systematic uncertainties cancel completely or at least partially. The main sources of systematic uncertainties in the calculation of  $R_\gamma$  and the direct photon spectrum for the photon conversion analysis are related to the material budget of the ALICE detector and the Monte Carlo based efficiency corrections to the inclusive photon and  $\pi^0$  spectra. The material budget of the detector in  $|\eta| < 0.9$  up to  $R = 180$  cm is  $11.4 \pm 0.5\%$  of a radiation length corresponding to a conversion probability of about  $8.5\%$  for  $p_T < 1$  GeV/c [118]. A more detailed description of the single photon selection and especially of the additional  $\pi^0$  uncertainties can be found in [108, 118].

Within this analysis, the direct-photon elliptic flow is extracted using the ALICE preliminary [49] direct-photon excess measured in 0-40% central collisions reported in Fig. 7.6. The measurement indicates an excess of direct photons above unity. The measurements are compared with the expected  $R_\gamma$  for the prompt photon contribution as calculated with next-to-leading-order (NLO) perturbative QCD calculations. The prompt photon expectations in Fig. 7.6 were determined as  $1 + N_{coll} \gamma_{pQCD}/\gamma_{decay}$  where

## 7. Elliptic flow of direct photons

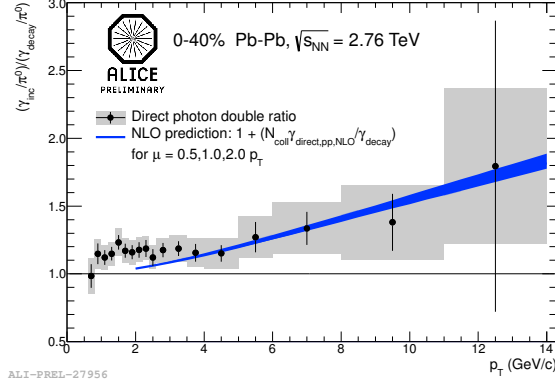


Figure 7.6: Direct-photon double ratio in Pb-Pb collisions at  $\sqrt{s_{\text{NN}}} = 2.76$  TeV for 0-40% centrality with NLO pQCD predictions.

the number of binary nucleon-nucleon collisions for a given centrality class was calculated within the Glauber Monte Carlo code [86]. The data are reasonably well described by the pQCD prediction at momenta above 3 GeV/c, where prompt photon production dominates over thermal photon production. At small transverse momenta, the data points are numerically above the pQCD prediction about 10-15%, which is usually attributed to the production of thermal photons. The uncertainties of the data are too large to test any details of the next-to-leading-order pQCD photon production.

### 7.3 Direct photon measurements

Since the ALICE preliminary direct photon excess is measured in 0-40% central collisions, the direct photon elliptic flow has been extracted in the same centrality range. The  $p_T$ -differential direct photon  $v_2$  is calculated as in equation 7.1 and the results are reported in Fig. 7.7 for the 0-40% central Pb-Pb collisions at  $\sqrt{s_{\text{NN}}} = 2.76$  TeV.

At low  $p_T$ , for  $1 < p_T < 3$  GeV/c, the elliptic flow is significantly larger than zero  $v_2^{\gamma,dir}$  with a magnitude similar to the observed charged pion el-

### 7.3 Direct photon measurements

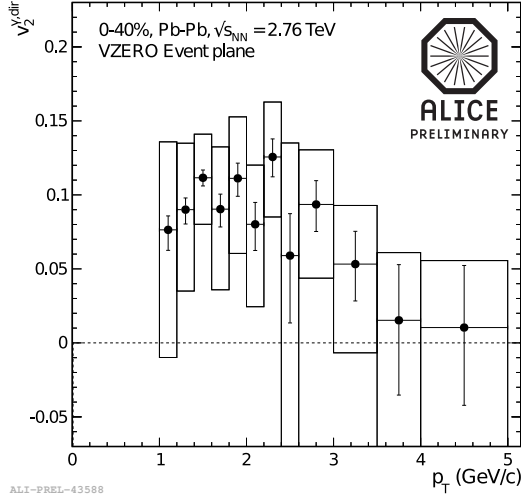


Figure 7.7: Direct-photon  $v_2^{\gamma,dir}$  in 0-40% Pb-Pb collisions at  $\sqrt{s_{NN}} = 2.76$  TeV.

liptic flow. At high  $p_T$ , the direct-photon anisotropic flow is consistent with zero, which is expected from the dominance of next-to-leading-order pQCD photons. A large  $v_2^{\gamma,dir}$  might lend support for a significant direct-photon emission from late stages of the system evolution where hadron flow has developed. Systematic uncertainties are mainly dominated by the uncertainties on the direct-photon excess  $R_\gamma$ , followed by the inclusive-photon elliptic flow.

#### 7.3.1 Model comparison

In Fig. 7.8 the direct photon spectra (left panel) and elliptic flow (right panel) are compared to theoretical model calculation. The elliptic photon flow predicted by the theoretical model falls severely short of the measured one. Recent hydrodynamical calculations [52, 54] include a substantial portion of thermal photons from the hot plasma phase and also a sizeable

## 7. Elliptic flow of direct photons

fraction from other sources in order to describe the observed direct-photon spectra. However, the emission from early stages of the system evolution yields a small  $v_2^{\gamma,dir}$  compared to the  $v_2$  of hadrons.

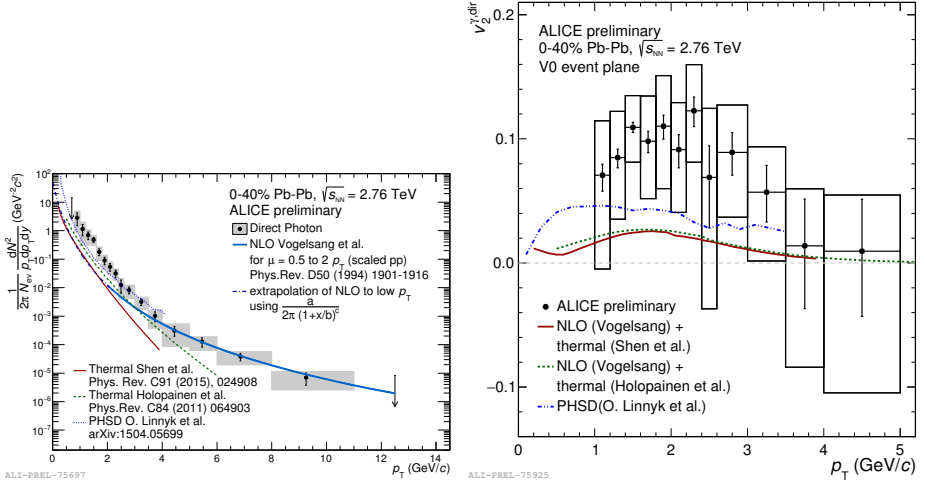


Figure 7.8: Direct photon spectra (left panel) and elliptic flow (right panel) compared to theoretical model calculation [52, 54, 57].

Furthermore, the current hydrodynamic approach [52], which implements a sudden transition from a thermalized liquid to non-interacting, free-streaming particles, does not allow for emission of photons by increasing collisions among the dilute hadrons after kinetic freeze-out. Such collisions processes are included in the PHSD approach which yields better agreement with the experimental data for both spectra and  $v_2$  [56, 57] at RHIC and at the LHC. Since all these additional hadronic photon emission processes occur during a stage where the hydrodynamic flow anisotropies have reached almost their final strength, their inclusion increases the direct photon elliptic flow. As it has been observed for the  $R_\gamma$ , the NLO predictions are in agreement with  $p_T$  spectrum above 4 GeV/c. Most theory predictions underestimate the direct photon spectra by factors of 2-10 at low transverse momentum.

### 7.4 Ongoing and future activities

In this section ongoing and possible further studies related to the azimuthal anisotropy of the direct photon are reported.

**Smaller centrality bins** Recently the direct photon production at mid-rapidity in Pb-Pb collisions at  $\sqrt{s_{\text{NN}}} = 2.76$  TeV has been measured in the transverse momentum range  $0.9 < p_{\text{T}} < 14$  GeV/ $c$ . Photons were detected via conversions in the ALICE detector material (PCM), as described in this thesis, or alternatively with the highly segmented electromagnetic calorimeter PHOS. The results of the two methods were combined and the direct photon spectra were measured for the 0-20%, 20-40%, and 40-80% most central collisions [119]. The combined PCM and PHOS double ratios  $R_{\gamma}$  measured for three centrality classes are shown in Fig. 7.9. A direct photon excess is observed for all centrality classes for  $p_{\text{T}} \geq 4$  GeV/ $c$ , and also for  $1 \leq p_{\text{T}} \leq 4$  GeV/ $c$  in the most central class.

In order to provide more precise constraints to theoretical model calculations, elliptic flow measurements could now be measured in smaller centrality classes with respect to the 0-40% preliminary measurements. Furthermore the experimental measurements of the direct photon flow could be also carried out using electromagnetic calorimeter PHOS in order to have an additional and independent measurement.

**Triangular flow** Higher order flow harmonics for the direct photons can provide better constraints on the shear viscosity over the entropy ratio used for the hydrodynamical model calculations, because, as for the hadrons [120], the shear viscosity is observed to suppress the higher harmonic flow coefficients more strongly than  $v_2$ . Measurements of the inclusive photon  $v_3$  are reported in Fig. 7.10 with the scalar product (red markers) and with the event plane method (black markers).

The triangular flow coefficient is observed to show a much less stronger centrality dependence compared to the elliptic flow, consistently with the picture that the  $v_3$  is purely driven by initial geometrical fluctuations of the nucleons participating in the collision. Also in this case a very good

## 7. Elliptic flow of direct photons

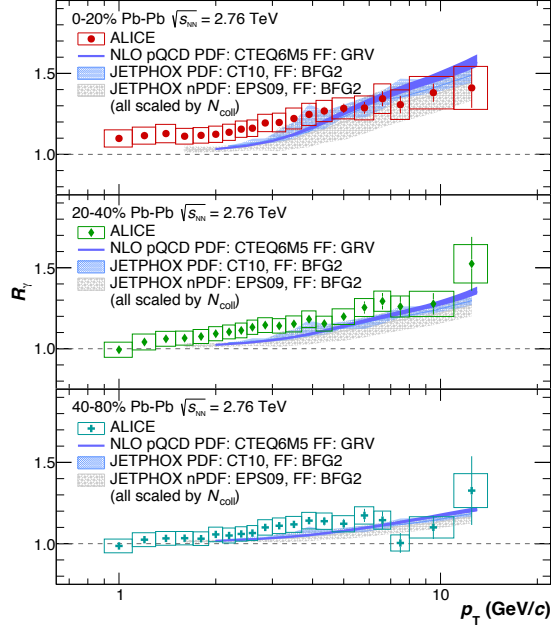


Figure 7.9: Combined PCM and PHOS double ratio  $R_\gamma$  in the 0-20%, 20-40%, and 40-80% centrality classes compared with pQCD calculations for nucleon-nucleon collisions scaled by the number of binary collisions for the corresponding the Pb-Pb centrality class.

agreement between the two methods has been observed for all the centrality classes. This agreement confirms that where the VZEROs detectors are used in the event plane method, the resulting  $v_2$  measurements are close to the r.m.s value measured with the scalar product method.

Furthermore there is also a new idea in which a large photon  $v_2$  is generated through a non-perturbative pre-equilibrium mechanism involving the initial magnetic field generated by the colliding nuclei [121]. The triangular flow, which is purely driven by initial density fluctuations and whose direction  $\Psi_3$  is therefore randomly oriented relative to the magnetic field,

## 7.4 Ongoing and future activities

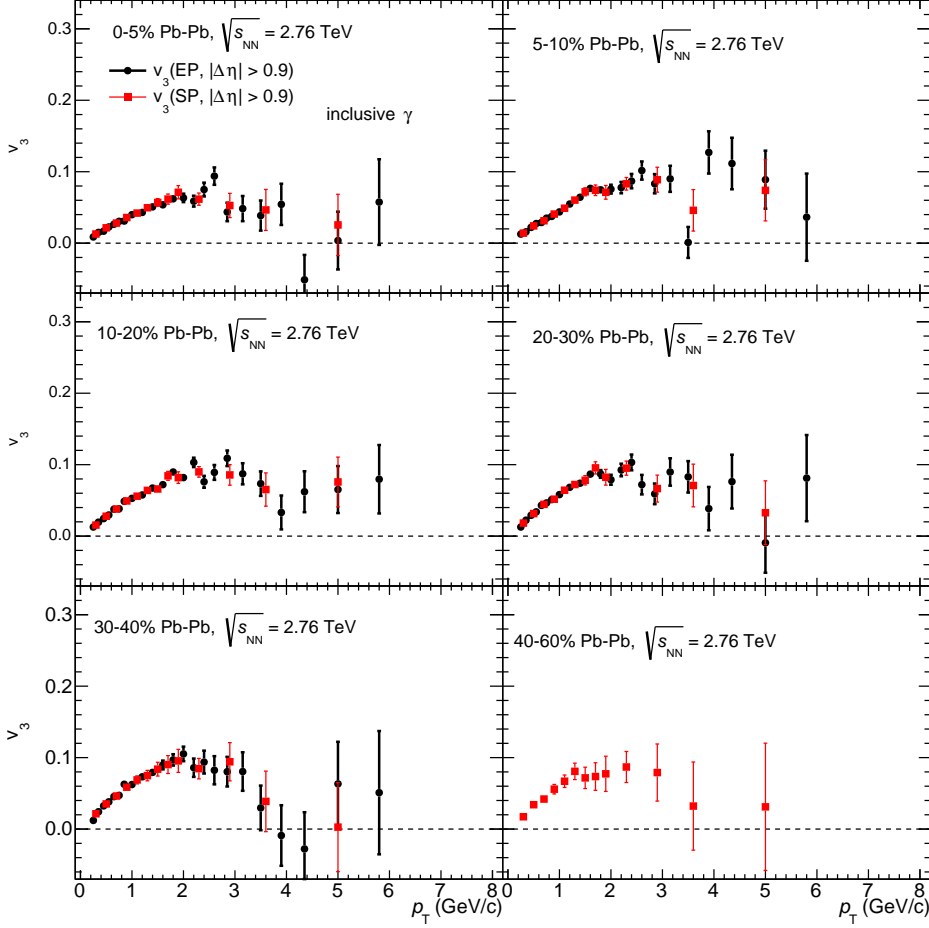


Figure 7.10: Comparison of the  $p_T$ -differential triangular flow of inclusive photon measured with the scalar product (red markers) and with the event plane (black markers) methods in several centrality intervals in Pb-Pb collisions at  $\sqrt{s_{NN}} = 2.76$  TeV. On both measurements the same pseudo-rapidity gap of 0.9 unit is imposed.

## 7. Elliptic flow of direct photons

---

is argued to be helpful to disentangle the thermal photon component from the pre-equilibrium photons.

Once the triangular flow of the direct photon will be available one can compute the ratio of the elliptic to triangular flow coefficient [52, 122]. This ratio is argued [52] to have a much reduced sensitivity to the prompt and pre-equilibrium photons that are understood to carry a small  $v_2$ . Compared to charged hadrons, the thermal photon ratio is observed to show stronger sensitivity to the shear viscosity of the medium. An experimental measurement of this ratio for direct photons will help shed light on the dynamical flow structure prior to the hadronic kinetic freeze-out.

---

---

# Conclusion

---

---

In this thesis the elliptic flow of the  $\phi$ -mesons, electrons from heavy-flavour decay and direct photons, measured in Pb-Pb collision with ALICE at the LHC is presented.

The development of the elliptic flow at the partonic stage can be probed by studying particles with a small hadronic cross section, like the  $\phi$ -meson, which are expected to be less affected by the hadronic stage. The  $\phi$ -meson is of particular interest since its mass is close to that of  $p$  and  $\Lambda$  baryons, which makes it an ideal candidate for testing both the mass ordering and the baryon-meson grouping at low and intermediate  $p_T$ , respectively.

Comparing the elliptic flow measured for several particle species, a mass ordering in the  $v_2$  measurements is observed for all centrality classes in the low  $p_T$  region (i.e.  $p_T < 3$  GeV/ $c$ ) attributed to the interplay between elliptic and radial flow. The  $v_2$  of the  $\phi$ -mesons follows qualitatively the mass scaling, however, for the lowest  $p_T$  bin measured there is an indication that the  $\phi$ -meson  $v_2$  is larger than the proton  $v_2$ .

In the VISHNU model, protons and  $\Lambda$ s experience a significant radial boost from the hadronic cascade (UrQMD), pushing their elliptic flows to larger transverse momenta with respect to the pure hydrodynamical model VISH2+1. The shift towards larger  $p_T$  is weaker for  $\Lambda$ s due to the smaller hadronic cross section for strange hadrons in the model. As a consequence

of the hadronic re-interaction implemented in VISHNU, the clear and well-defined mass ordering observed in the VISH2+1 model is not preserved anymore. The modification of the  $v_2^p(p_T)$  is nevertheless too large so that VISHNU fails to describe the protons, as well as VISH2+1. The measurements of the  $\phi$ -meson elliptic flow are qualitatively described by both model predictions, in which the double strange meson is rather weakly coupled to the hadronic medium and it decouples from the system almost immediately after the hadronization, without further developing its elliptic flow.

For higher  $p_T$  values the  $\phi$ -meson  $v_2$  appears to follow the band of baryons for central events within uncertainties. For peripheral collisions though, the  $v_2$  values of the  $\phi$ -meson shift progressively to the band of mesons, consistently with what has been observed for the transverse momentum particles ratio.

Further insight into the transport properties of the medium is provided by the measurement of the elliptic flow of heavy-flavour hadrons and heavy-flavour decay leptons. Contrary to light quarks and gluons, the formation time of heavy quarks, about  $1/(2m_{c \text{ or } b})$  where  $m$  is the mass of the quark, is expected to be smaller than the QGP formation time ( $\sim 1$  fm/c) and the heavy quarks have a very small annihilation rate. Due to their large mass it is not obvious that the  $c$  and  $b$  quarks would thermalize in the medium. At low and intermediate  $p_T$  ( $p_T < 6$  GeV/c), the  $v_2$  coefficient of heavy-flavour hadrons and their decay products is expected to be sensitive to the heavy-quark hadronization mechanism. Hadronization via the recombination of heavy quarks with light quarks from the thermalized medium could further increase the elliptic flow of heavy-flavour hadrons and their decay products. At high  $p_T$  the  $v_2$  measurements can constrain the path-length dependence of the in-medium parton energy loss, which is different for radiative and collisional energy loss. The measured elliptic flow results for electrons from heavy flavour are presented as a function of transverse momentum in the interval 0.5–13 GeV/c in three centrality classes (0-10%, 10-20%, and 20-40%). The  $p_T$  dependence of the heavy-flavour decay electron  $v_2$  shows a positive  $v_2$  at low and intermediate  $p_T$  in all centrality classes with a significance greater than  $5.9 \sigma$  in the  $p_T$  range 2-2.5 GeV/c in semi-central (20-40%) collisions, combining statistical and systematic uncertainties. This

## Conclusion

---

indicates that heavy quarks, mainly charm quarks, take part in the collective expansion of the medium formed in Pb-Pb collisions.

At higher  $p_T$  ( $p_T > 4$  GeV/ $c$ ) the measured  $v_2$ , which most probably originates from the path-length dependence of the partonic energy loss, is consistent with zero, within, however, large uncertainties. An increase of  $v_2$  as a function of the collision centrality is observed in particular at low transverse momentum ( $1.25 < p_T < 1.5$  GeV/ $c$ ). This trend is expected from the increase of the initial spatial anisotropy from central to peripheral collisions. The measured  $v_2$  is best described by models that predict significant interactions of heavy quarks with the medium and include mechanisms like collisional energy loss and hadronization via recombination, which transfer to heavy quarks and heavy-flavour hadrons the elliptic flow built-up during the system expansion.

The measurement of direct photons is a promising tool for the study of the early phase of ultra-relativistic nucleus-nucleus collisions. Since photons do not interact with the strongly-coupling medium created in these collisions, they carry undistorted information about the system at their production time. Recent hydrodynamical calculations predict a substantial portion of direct photons from early phases of the collision, where the anisotropic flow has not yet fully developed. Thus, the direct-photon azimuthal anisotropy is generally expected to be small compared to that of the hadrons. Measurements of the elliptic flow at RHIC and at the LHC exhibit an unexpectedly large elliptic flow, which cannot be explained within the picture of early direct photon production. The results provide a hint for a non-zero  $v_2$  for  $1 < p_T < 3$  GeV/ $c$  with a magnitude similar to that of the observed charged pions. Therefore, the observed large  $v_2$  of direct photons might lend support for a significant photon emission from the late stages of the system evolution where the hadron flow has already been built-up.



---

---

# Samenvatting

---

---

In dit proefschrift is de elliptische flow (stroming), gemeten in Pb–Pb botsingen door ALICE bij de LHC, van  $\phi$ -mesonen, elektronen uit het verval van zware quarks, en direct geproduceerde fotonen gepresenteerd.

De ontwikkeling van elliptische flow in het parton stadium kan onderzocht worden met behulp van deeltjes met een kleine werkzame hadronische doorsnede, zoals het  $\phi$ -meson, van welke verwacht wordt dat ze niet beïnvloed worden door processen in het hadronische stadium.

Wanneer elliptische flow van verschillende soorten deeltjes onderling vergeleken wordt, wordt een ordening naar massa zichtbaar in iedere centraliteitsklasse bij lage transversale impuls ( $p_T < 3 \text{ GeV}/c$ ), welke toegeschreven wordt aan een samenspel tussen elliptische en radiale flow. De  $v_2$  van het  $\phi$ -meson volgt deze massa ordening ongeveer, hoewel opgemerkt moet worden dat voor de laagste  $p_T$ -waarden waarbij de  $v_2$  gemeten is deze afhankelijkheid van massa niet gevolgd lijkt te worden. De metingen van de elliptische flow van het  $\phi$ -meson wordt kwalitatief beschreven vanuit hydrodynamische modelleringen, in welke het meson met twee s-quarks zwak gekoppeld is aan het hadronische medium, en zich vrijwel onmiddellijk na hadronisatie ontkoppelt, zonder verdere elliptische flow te ontwikkelen.

Metingen van elliptische flow van hadronen met zware quarks en leptonen geproduceerd als het verval van deze hadronen, verschaffen meer inzicht

in de transporteigenschappen het botsingsmedium. Bij lage en tussenliggende  $p_T$  ( $p_T < 6$  GeV/ $c$ ) is het te verwachten dat de  $v_2$  coëfficiënt van hadronen met zware quarks, evenals hun vervalproducten, gevoelig zijn voor de hadronisatiemechanismen voor zware quarks. Hadronisatie via de hercombinatie van zware en lichte quarks uit het medium dat in thermisch evenwicht verkeert zou de elliptische flow van zware quarks en hun vervalproducten toe kunnen doen nemen. Bij hoge  $p_T$  kunnen de  $v_2$  metingen de invloed van weglengte op energieverlies in het medium, hetwelk verschillend is voor verstrooiings- en stralingsprocessen, begrenzen. De  $v_2$  van elektronen die afkomstig zijn van het verval van hadronen bestaand uit zware quarks is positief bij lage en tussenliggende  $p_T$  in alle centraliteitsklassen, met een significantie van meer dan  $5.9 \sigma$  in het  $p_T$  interval 2-2.5 GeV/ $c$  in semi-centrale (20-40%) botsingen, wanneer statistische en systematische onzekerheden gecombineerd worden. Dit doet vermoeden dat zware quarks, voornamelijk charm quarks, deelnemen aan de uitdijning van het medium dat in Pb–Pb botsingen gevormd wordt.

Bij hoge  $p_T$  ( $p_T > 4$  GeV/ $c$ ) - hier is de gemeten  $v_2$  gevoelig voor energieverlies van partonen - is  $v_2$  in overeenstemming met nul, hoewel de meting grote onzekerheden heeft. De waargenomen  $v_2$  wordt het meest accuraat beschreven met modellen welke significante interacties, zoals energieverlies door verstrooiing en hadronisatie via hercombinatie, tussen zware quarks en het medium aannemen. Deze processen geven de elliptische flow, opgebouwd tijdens de expansie van het systeem, door aan zware quarks en hadronen.

De meting van direct geproduceerde fotonen is een veelbelovende methode om de vroege fase van ultrarelativistische nucleus–nucleus botsingen te bestuderen. Omdat fotonen niet interageren met het sterk gekoppelde medium dat in deze botsingen gecreëerd wordt, wordt de informatie over de productie van deze fotonen niet verstoord. Metingen van de elliptische flow van deze fotonen bij de LHC leveren echter onverwachte grote waarden op, welke niet vanuit vroege, directe fotonproductie verklaard kunnen worden. De metingen suggereren een  $v_2$  gelijk aan die van geladen pionen tussen  $1 < p_T < 3$  GeV/ $c$ . Dientengevolge doet deze observatie vermoeden dat er een significante fotonemissie plaats vindt in latere stadia van de systeemevolutie, in welke de hadronische flow reeds opgebouwd is.

---

---

# Bibliography

---

---

- [1] M. Peskin and D. Schroeder, *An introduction to quantum field theory*. Addison-Wesley, 1995.
- [2] Z. Fodor and S. Katz, “Critical point of QCD at finite T and  $\mu$ , lattice results for physical quark masses,” *JHEP* **0404** (2004) 050, [arXiv:hep-lat/0402006](#) [[hep-lat](#)].
- [3] I. Zakout and C. Greiner, “The quark-gluon-plasma phase transition diagram, Hagedorn matter and quark-gluon liquid,” [arXiv:1002.3119](#) [[nucl-th](#)].
- [4] S. Gupta, “Phases and properties of quark matter,” *J.Phys.* **G35** (2008) 104018, [arXiv:0806.2255](#) [[nucl-th](#)].
- [5] M. A. Stephanov, “QCD phase diagram and the critical point,” *Prog. Theor. Phys. Suppl.* **153** (2004) 139–156, [arXiv:hep-ph/0402115](#) [[hep-ph](#)]. [*Int. J. Mod. Phys.A*20,4387(2005)].
- [6] F.-M. Liu and S.-X. Liu, “Quark-gluon plasma formation time and direct photons from heavy ion collisions,” *Phys. Rev.* **C89** no. 3, (2014) 034906, [arXiv:1212.6587](#) [[nucl-th](#)].

- [7] J. Bjorken, “Highly Relativistic Nucleus-Nucleus Collisions: The Central Rapidity Region,” *Phys.Rev.* **D27** (1983) 140–151.
- [8] E. Schnedermann, J. Sollfrank, and U. Heinz, “Thermal phenomenology of hadrons from 200  $A$  GeV S+S collisions,” *Phys. Rev. C* **48** (Nov, 1993) 2462–2475.  
<http://link.aps.org/doi/10.1103/PhysRevC.48.2462>.
- [9] **STAR** Collaboration, J. Adams *et al.*, “Identified particle distributions in  $pp$  and Au + Au collisions at  $\sqrt{s_{NN}} = 200$  GeV,” *Phys. Rev. Lett.* **92** (Mar, 2004) 112–301.  
<http://link.aps.org/doi/10.1103/PhysRevLett.92.112301>.
- [10] **ALICE** Collaboration, B. Abelev *et al.*, “Pion, Kaon, and Proton Production in Central Pb–Pb Collisions at  $\sqrt{s_{NN}} = 2.76$  TeV,” *Phys.Rev.Lett.* **109** (2012) 252301, [arXiv:1208.1974 \[hep-ex\]](#).
- [11] S. Voloshin and Y. Zhang, “Flow study in relativistic nuclear collisions by Fourier expansion of Azimuthal particle distributions,” *Z.Phys.* **C70** (1996) 665–672, [arXiv:hep-ph/9407282 \[hep-ph\]](#).
- [12] **STAR** Collaboration, B. I. Abelev *et al.*, “Measurements of  $\phi$ -meson production in relativistic heavy-ion collisions at RHIC,” *Phys. Rev.* **C79** (2009) 064903, [arXiv:0809.4737 \[nucl-ex\]](#).
- [13] P. Kovtun, D. T. Son, and A. O. Starinets, “Viscosity in strongly interacting quantum field theories from black hole physics,” *Phys.Rev.Lett.* **94** (2005) 111601, [arXiv:hep-th/0405231 \[hep-th\]](#).
- [14] **STAR** Collaboration, J. Adams *et al.*, “Experimental and theoretical challenges in the search for the quark gluon plasma: The STAR Collaboration’s critical assessment of the evidence from RHIC collisions,” *Nucl.Phys.* **A757** (2005) 102–183,  
[arXiv:nucl-ex/0501009 \[nucl-ex\]](#).
- [15] **PHENIX** Collaboration, K. Adcox *et al.*, “Formation of dense partonic matter in relativistic nucleus-nucleus collisions at RHIC:

## BIBLIOGRAPHY

---

- Experimental evaluation by the PHENIX collaboration,” *Nucl.Phys.* **A757** (2005) 184–283, [arXiv:nuc1-ex/0410003](#) [[nuc1-ex](#)].
- [16] **ALICE** Collaboration, K. Aamodt *et al.*, “Elliptic flow of charged particles in Pb–Pb collisions at 2.76 TeV,” *Phys.Rev.Lett.* **105** (2010) 252302, [arXiv:1011.3914](#) [[nuc1-ex](#)].
- [17] **ATLAS** Collaboration, G. Aad *et al.*, “Measurement of the pseudorapidity and transverse momentum dependence of the elliptic flow of charged particles in lead-lead collisions at  $\sqrt{s_{NN}} = 2.76$  TeV with the ATLAS detector,” *Phys.Lett.* **B707** (2012) 330–348, [arXiv:1108.6018](#) [[hep-ex](#)].
- [18] **CMS** Collaboration, S. Chatrchyan *et al.*, “Measurement of the elliptic anisotropy of charged particles produced in PbPb collisions at  $\sqrt{s_{NN}}=2.76$  TeV,” *Phys.Rev.* **C87** no. 1, (2013) 014902, [arXiv:1204.1409](#) [[nuc1-ex](#)].
- [19] **STAR** Collaboration, J. Adams *et al.*, “Azimuthal anisotropy in Au+Au collisions at  $\sqrt{s_{NN}} = 200$  GeV,” *Phys. Rev. C* **72** (Jul, 2005) 014904. <http://link.aps.org/doi/10.1103/PhysRevC.72.014904>.
- [20] P. Huovinen, P. Kolb, U. W. Heinz, P. Ruuskanen, and S. Voloshin, “Radial and elliptic flow at RHIC: Further predictions,” *Phys.Lett.* **B503** (2001) 58–64, [arXiv:hep-ph/0101136](#) [[hep-ph](#)].
- [21] U. Heinz, C. Shen, and H. Song, “The viscosity of quark-gluon plasma at RHIC and the LHC,” *AIP Conf.Proc.* **1441** (2012) 766–770, [arXiv:1108.5323](#) [[nuc1-th](#)].
- [22] T. Hirano and Y. Nara, “Eccentricity fluctuation effects on elliptic flow in relativistic heavy ion collisions,” *Phys.Rev.* **C79** (2009) 064904, [arXiv:0904.4080](#) [[nuc1-th](#)].
- [23] E. Iancu, A. Leonidov, and L. McLerran, “The Color glass condensate: An Introduction,” [arXiv:hep-ph/0202270](#) [[hep-ph](#)].

- [24] Z. Qiu and U. Heinz, “Event-by-event shape and flow fluctuations of relativistic heavy-ion collision fireballs,” *Phys. Rev. C* **84** (Aug, 2011) 024911. <http://link.aps.org/doi/10.1103/PhysRevC.84.024911>.
- [25] C. Shen, U. Heinz, P. Huovinen, and H. Song, “Radial and elliptic flow in Pb+Pb collisions at the Large Hadron Collider from viscous hydrodynamic,” *Phys.Rev.* **C84** (2011) 044903, [arXiv:1105.3226 \[nucl-th\]](#).
- [26] H. Song, S. Bass, and U. W. Heinz, “Spectra and elliptic flow for identified hadrons in 2.76A TeV Pb + Pb collisions,” *Phys.Rev.* **C89** no. 3, (2014) 034919, [arXiv:1311.0157 \[nucl-th\]](#).
- [27] M. Bleicher, E. Zabrodin, C. Spieles, S. Bass, C. Ernst, *et al.*, “Relativistic hadron hadron collisions in the ultrarelativistic quantum molecular dynamics model,” *J.Phys.* **G25** (1999) 1859–1896, [arXiv:hep-ph/9909407 \[hep-ph\]](#).
- [28] R. Baier, Y. L. Dokshitzer, A. H. Mueller, S. Peigne, and D. Schiff, “Radiative energy loss of high-energy quarks and gluons in a finite volume quark - gluon plasma,” *Nucl.Phys.* **B483** (1997) 291–320, [arXiv:hep-ph/9607355 \[hep-ph\]](#).
- [29] C. A. Salgado and U. A. Wiedemann, “Calculating quenching weights,” *Phys. Rev.* **D68** (2003) 014008, [arXiv:hep-ph/0302184 \[hep-ph\]](#).
- [30] Y. L. Dokshitzer and D. Kharzeev, “Heavy quark colorimetry of QCD matter,” *Phys.Lett.* **B519** (2001) 199–206, [arXiv:hep-ph/0106202 \[hep-ph\]](#).
- [31] M. Djordjevic, “Collisional energy loss in a finite size QCD matter,” *Phys.Rev.* **C74** (2006) 064907, [arXiv:nucl-th/0603066 \[nucl-th\]](#).
- [32] D. Molnar and S. A. Voloshin, “Elliptic flow at large transverse momenta from quark coalescence,” *Phys.Rev.Lett.* **91** (2003) 092301, [arXiv:nucl-th/0302014 \[nucl-th\]](#).

## BIBLIOGRAPHY

---

- [33] V. Greco, C. Ko, and P. Levai, “Parton coalescence at RHIC,” *Phys.Rev.* **C68** (2003) 034904, [arXiv:nuc1-th/0305024](#) [nuc1-th].
- [34] M. Gyulassy, I. Vitev, and X. N. Wang, “High  $p_T$  azimuthal asymmetry in non-central A+A at RHIC,” *Phys. Rev. Lett.* **86** (2001) 2537–2540, [arXiv:nuc1-th/0012092](#) [nuc1-th].
- [35] E. V. Shuryak, “Azimuthal asymmetry at large  $p_T$  seem to be too large for a pure jet quenching,” *Phys. Rev. C* **66** (Aug, 2002) 027902. <http://link.aps.org/doi/10.1103/PhysRevC.66.027902>.
- [36] **ALICE** Collaboration, B. Abelev *et al.*, “D meson elliptic flow in non-central Pb–Pb collisions at  $\sqrt{s_{NN}} = 2.76$  TeV,” *Phys.Rev.Lett.* **111** (2013) 102301, [arXiv:1305.2707](#) [nuc1-ex].
- [37] **ALICE** Collaboration, B. B. Abelev *et al.*, “Azimuthal anisotropy of D meson production in Pb–Pb collisions at  $\sqrt{s_{NN}} = 2.76$  TeV,” *Phys.Rev.* **C90** no. 3, (2014) 034904, [arXiv:1405.2001](#) [nuc1-ex].
- [38] **ALICE** Collaboration, J. Adam *et al.*, “Elliptic flow of muons from heavy-flavour hadron decays at forward rapidity in Pb–Pb collisions at  $\sqrt{s_{NN}} = 2.76$  TeV,” [arXiv:1507.03134](#) [nuc1-ex].
- [39] **STAR** Collaboration, L. Adamczyk *et al.*, “Elliptic flow of non-photonic electrons in Au+Au collisions at  $\sqrt{s_{NN}} = 200, 62.4$  and 39 GeV,” [arXiv:1405.6348](#) [hep-ex].
- [40] **PHENIX** Collaboration, A. Adare *et al.*, “Heavy Quark Production in  $p + p$  and Energy Loss and Flow of Heavy Quarks in Au+Au Collisions at  $\sqrt{s_{NN}} = 200$  GeV,” *Phys.Rev.* **C84** (2011) 044905, [arXiv:1005.1627](#) [nuc1-ex].
- [41] J. Uphoff, O. Fochler, Z. Xu, and C. Greiner, “Open Heavy Flavor in Pb+Pb Collisions at  $\sqrt{s_{NN}} = 2.76$  TeV within a Transport Model,” *Phys.Lett.* **B717** (2012) 430–435, [arXiv:1205.4945](#) [hep-ph].

- [42] J. Uphoff, O. Fochler, Z. Xu, and C. Greiner, “Heavy vs. light flavor energy loss within a partonic transport model,” *J.Phys.Conf.Ser.* **509** (2014) 012077, [arXiv:1310.3597 \[hep-ph\]](#).
- [43] M. He, R. J. Fries, and R. Rapp, “Heavy Flavor at the Large Hadron Collider in a Strong Coupling Approach,” *Phys.Lett.* **B735** (2014) 445–450, [arXiv:1401.3817 \[nucl-th\]](#).
- [44] M. Nahrgang, J. Aichelin, P. B. Gossiaux, and K. Werner, “Influence of hadronic bound states above  $T_c$  on heavy-quark observables in Pb + Pb collisions at the CERN Large Hadron Collider,” *Phys.Rev.* **C89** no. 1, (2014) 014905, [arXiv:1305.6544 \[hep-ph\]](#).
- [45] R. Baier, D. Schiff, and B. Zakharov, “Energy loss in perturbative QCD,” *Ann.Rev.Nucl.Part.Sci.* **50** (2000) 37–69, [arXiv:hep-ph/0002198 \[hep-ph\]](#).
- [46] K. Werner, I. Karpenko, M. Bleicher, T. Pierog, and S. Porteboeuf-Houssais, “Jets, Bulk Matter, and their Interaction in Heavy Ion Collisions at Several TeV,” *Phys.Rev.* **C85** (2012) 064907, [arXiv:1203.5704 \[nucl-th\]](#).
- [47] W. Alberico, A. Beraudo, A. De Pace, A. Molinari, M. Monteno, *et al.*, “Heavy flavors in AA collisions: production, transport and final spectra,” *Eur.Phys.J.* **C73** (2013) 2481, [arXiv:1305.7421 \[hep-ph\]](#).
- [48] L. E. Gordon and W. Vogelsang, “Polarized and unpolarized isolated prompt photon production beyond the leading order,” *Phys. Rev. D* **50** (Aug, 1994) 1901–1916.  
<http://link.aps.org/doi/10.1103/PhysRevD.50.1901>.
- [49] **ALICE** Collaboration, M. Wilde, “Measurement of Direct Photons in pp and Pb–Pb Collisions with ALICE,” *Nucl.Phys.* **A904-905** (2013) 573c–576c, [arXiv:1210.5958 \[hep-ex\]](#).

## BIBLIOGRAPHY

---

- [50] **PHENIX** Collaboration, A. Adare *et al.*, “Centrality dependence of low-momentum direct-photon production in Au+Au collisions at  $\sqrt{s_{NN}} = 200$  GeV,” *Phys.Rev.* **C91** no. 6, (2015) 064904, [arXiv:1405.3940 \[nucl-ex\]](#).
- [51] **PHENIX** Collaboration, X. He, “Phenix highlights,” *Nucl.Phys.* **A931** no. 0, (2014) 32 – 40. <http://www.sciencedirect.com/science/article/pii/S0375947414003418>.
- [52] C. Shen, U. W. Heinz, J.-F. Paquet, I. Kozlov, and C. Gale, “Anisotropic flow of thermal photons as a quark-gluon plasma viscometer,” *Phys.Rev.* **C91** no. 2, (2015) 024908, [arXiv:1308.2111 \[nucl-th\]](#).
- [53] C. Shen, U. Heinz, J.-F. m. c. Paquet, and C. Gale, “Thermal photons as a quark-gluon plasma thermometer reexamined,” *Phys. Rev. C* **89** (Apr, 2014) 044910. <http://link.aps.org/doi/10.1103/PhysRevC.89.044910>.
- [54] H. Holopainen, S. S. Räsänen, and K. J. Eskola, “Elliptic flow of thermal photons in heavy-ion collisions at energies available at the BNL Relativistic Heavy Ion Collider and at the CERN Large Hadron Collider,” *Phys. Rev. C* **84** (Dec, 2011) 064903. <http://link.aps.org/doi/10.1103/PhysRevC.84.064903>.
- [55] R. Chatterjee, H. Holopainen, I. Helenius, T. Renk, and K. J. Eskola, “Elliptic flow of thermal photons from event-by-event hydrodynamic model,” *Phys.Rev.* **C88** (2013) 034901, [arXiv:1305.6443 \[hep-ph\]](#).
- [56] O. Linnyk, V. Konchakovski, W. Cassing, and E. Bratkovskaya, “Photon elliptic flow in relativistic heavy-ion collisions: hadronic versus partonic sources,” *Phys.Rev.* **C88** (2013) 034904, [arXiv:1304.7030 \[nucl-th\]](#).
- [57] O. Linnyk, V. Konchakovski, T. Steinert, W. Cassing, and E. Bratkovskaya, “Hadronic and partonic sources of direct photons in relativistic heavy-ion collisions,” [arXiv:1504.05699 \[nucl-th\]](#).

- [58] **PHENIX** Collaboration, A. Adare *et al.*, “Observation of direct-photon collective flow in  $\sqrt{s_{NN}} = 200$  GeV Au+Au collisions,” *Phys.Rev.Lett.* **109** (2012) 122302, [arXiv:1105.4126 \[nucl-ex\]](#).
- [59] **PHENIX** Collaboration, I. Tserruya, “Photons and low-mass dileptons: results from PHENIX,” *Nucl.Phys.* **A904-905** (2013) 225c–232c, [arXiv:1211.6002 \[nucl-ex\]](#).
- [60] **ALICE** Collaboration, F. Carminati *et al.*, “ALICE: Physics Performance Report, Volume I,” *Journal of Physics G: Nuclear and Particle Physics* **30** no. 11, (2004) 1517.  
<http://stacks.iop.org/0954-3899/30/i=11/a=001>.
- [61] **ALICE** Collaboration, B. Alessandro *et al.*, “ALICE: Physics Performance Report, Volume II,” *Journal of Physics G: Nuclear and Particle Physics* **32** no. 10, (2006) 1295.  
<http://stacks.iop.org/0954-3899/32/i=10/a=001>.
- [62] **ALICE** Collaboration, K. Aamodt *et al.*, “The ALICE experiment at the CERN LHC,” *Journal of Instrumentation* **3** no. 08, (2008) S08002. <http://stacks.iop.org/1748-0221/3/i=08/a=S08002>.
- [63] **ALICE** Collaboration, K. Aamodt *et al.*, “Alignment of the ALICE Inner Tracking System with cosmic-ray tracks,” *Journal of Instrumentation* **5** no. 03, (2010) P03003.  
<http://stacks.iop.org/1748-0221/5/i=03/a=P03003>.
- [64] **ALICE** Collaboration, J. Alme, Y. Andres, H. Appelshauser, S. Bablok, N. Bialas, *et al.*, “The ALICE TPC, a large 3-dimensional tracking device with fast readout for ultra-high multiplicity events,” *Nucl.Instrum.Meth.* **A622** (2010) 316–367, [arXiv:1001.1950 \[physics.ins-det\]](#).
- [65] **ALICE** Collaboration, M. J. Kweon, “The Transition Radiation Detector for ALICE at LHC,” *Nucl. Phys. A* **830** no. arXiv:0907.3380, (Jul, 2009) 535c–538c. 4 p.  
<http://cds.cern.ch/record/1191722>.

## BIBLIOGRAPHY

---

- [66] **ALICE** Collaboration, A. Akindinov *et al.*, “Performance of the ALICE Time-Of-Flight detector at the LHC,” *The European Physical Journal Plus* **128** no. 4, (2013) .  
<http://dx.doi.org/10.1140/epjp/i2013-13044-x>.
- [67] **ALICE** Collaboration, G. De Cataldo, “Performance of the High Momentum Particle Identification Detector in ALICE at LHC,”  
<http://cds.cern.ch/record/1741655>.
- [68] **ALICE** Collaboration, M. Ippolitov *et al.*, “Status and Performance of the ALICE/PHOS Electromagnetic Calorimeter,”  
<http://cds.cern.ch/record/1742147>.
- [69] **ALICE** Collaboration, P. Cortese *et al.*, “ALICE Electromagnetic Calorimeter Technical Design Report,”  
<https://cds.cern.ch/record/1121574>.
- [70] **ALICE** Collaboration, A. Klimov *et al.*, “High-speed electronics of the T0 detector for the ALICE experiment (CERN),”  
*Phys.Atom.Nucl.* **72** (2009) 286–292.
- [71] **ALICE** Collaboration, E. Abbas *et al.*, “Performance of the ALICE VZERO system,” *Journal of Instrumentation* **8** no. 10, (2013) P10016. <http://stacks.iop.org/1748-0221/8/i=10/a=P10016>.
- [72] **ALICE** Collaboration, C. H. Christensen *et al.*, “The ALICE Forward Multiplicity Detector,” *Int.J.Mod.Phys.* **E16** (2007) 2432–2437, [arXiv:0712.1117](https://arxiv.org/abs/0712.1117) [nucl-ex].
- [73] **ALICE** Collaboration, “ALICE Photon Multiplicity Detector (PMD): Technical Design Report,”  
<https://cds.cern.ch/record/451099>.
- [74] **ALICE** Collaboration, R. Arnaldi *et al.*, “Performance of a forward hadron calorimeter for the ALICE experiment,”  
<http://cds.cern.ch/record/409740>.

- [75] **ALICE** Collaboration, “Technical Design Report for the Muon Forward Tracker,”. <http://cds.cern.ch/record/1981898>.
- [76] **ALICE** Collaboration, R. Bellwied, “ALICE EMCal Physics Performance Report,” *ArXiv e-prints* (Aug., 2010) , [arXiv:1008.0413](https://arxiv.org/abs/1008.0413) [[physics.ins-det](#)].
- [77] M. Luzum and J.-Y. Ollitrault, “Eliminating experimental bias in anisotropic-flow measurements of high-energy nuclear collisions,” *Phys.Rev.* **C87** no. 4, (2013) 044907, [arXiv:1209.2323](https://arxiv.org/abs/1209.2323) [[nucl-ex](#)].
- [78] A. M. Poskanzer and S. A. Voloshin, “Methods for analyzing anisotropic flow in relativistic nuclear collisions,” *Phys. Rev. C* **58** (Sep, 1998) 1671–1678.  
<http://link.aps.org/doi/10.1103/PhysRevC.58.1671>.
- [79] **ALICE** Collaboration, B. Abelev *et al.*, “Anisotropic flow of charged hadrons, pions and (anti-)protons measured at high transverse momentum in Pb–Pb collisions at  $\sqrt{s_{NN}}=2.76$  TeV,” *Phys.Lett.* **B719** (2013) 18–28, [arXiv:1205.5761](https://arxiv.org/abs/1205.5761) [[nucl-ex](#)].
- [80] I. Selyuzhenkov and S. Voloshin, “Effects of nonuniform acceptance in anisotropic flow measurements,” *Phys. Rev. C* **77** (Mar, 2008) 034904. <http://link.aps.org/doi/10.1103/PhysRevC.77.034904>.
- [81] **STAR** Collaboration, C. Adler *et al.*, “Elliptic flow from two- and four-particle correlations in Au+Au collisions at  $\sqrt{s_{NN}} = 130$  GeV,” *Phys. Rev. C* **66** (Sep, 2002) 034904.  
<http://link.aps.org/doi/10.1103/PhysRevC.66.034904>.
- [82] **ALICE** Collaboration, B. B. Abelev *et al.*, “Elliptic flow of identified hadrons in Pb–Pb collisions at  $\sqrt{s_{NN}} = 2.76$  TeV,” [arXiv:1405.4632](https://arxiv.org/abs/1405.4632) [[nucl-ex](#)].
- [83] A. Bilandzic, “Anisotropic flow measurements in ALICE at the Large Hadron Collider.” Phd thesis, 2011. Nikhef and Utrecht University, The Netherlands.

## BIBLIOGRAPHY

---

- [84] A. Bilandzic, R. Snellings, and S. Voloshin, “Flow analysis with cumulants: Direct calculations,” *Phys. Rev.* **C83** (2011) 044913, [arXiv:1010.0233 \[nucl-ex\]](#).
- [85] **ALICE** Collaboration, B. B. Abelev *et al.*, “Performance of the ALICE Experiment at the CERN LHC,” *Int.J.Mod.Phys.* **A29** (2014) 1430044, [arXiv:1402.4476 \[nucl-ex\]](#).
- [86] **ALICE** Collaboration, B. Abelev *et al.*, “Centrality determination of Pb–Pb collisions at  $\sqrt{s_{NN}} = 2.76$  TeV with ALICE,” *Phys.Rev.* **C88** no. 4, (2013) 044909, [arXiv:1301.4361 \[nucl-ex\]](#).
- [87] R. Glauber and G. Matthiae, “High-energy scattering of protons by nuclei,” *Nucl.Phys.* **B21** (1970) 135–157.
- [88] M. L. Miller, K. Reygers, S. J. Sanders, and P. Steinberg, “Glauber modeling in high energy nuclear collisions,” *Ann. Rev. Nucl. Part. Sci.* **57** (2007) 205–243, [arXiv:nucl-ex/0701025 \[nucl-ex\]](#).
- [89] G. de Barros, B. Fenton-Olsen, P. Jacobs, and M. Ploskon, “Data-driven analysis methods for the measurement of reconstructed jets in heavy ion collisions at RHIC and LHC,” *Nucl.Phys.* **A910-911** (2013) 314–318, [arXiv:1208.1518 \[hep-ex\]](#).
- [90] M. Masera, G. Ortona, M. G. Poghosyan, and F. Prino, “Anisotropic transverse flow introduction in monte carlo generators for heavy ion collisions,” *Phys. Rev. C* **79** (Jun, 2009) 064909. <http://link.aps.org/doi/10.1103/PhysRevC.79.064909>.
- [91] N. Borghini, “Characterization and analysis of azimuthally sensitive correlations,” *J.Phys.* **G31** (2005) S15–S22, [arXiv:nucl-th/0409024 \[nucl-th\]](#).
- [92] N. Borghini and J. Ollitrault, “Azimuthally sensitive correlations in nucleus-nucleus collisions,” *Phys.Rev.* **C70** (2004) 064905, [arXiv:nucl-th/0407041 \[nucl-th\]](#).

- [93] K. Olive *et al.*, “Particle Data Group,” *Chin. Phys.* **C38** (2014) 090001.
- [94] X.-N. Wang and M. Gyulassy, “HIJING: A Monte Carlo model for multiple jet production in  $pp$ ,  $pA$  and  $AA$  collisions,” *Phys. Rev.* **D44** (1991) 3501–3516.
- [95] I. Belikov, P. Z. Khristov, M. Ivanov, T. Kuhr, and K. Safarik, “Bayesian approach for combined particle identification in alice experiment at lhcb,” <https://cds.cern.ch/record/865616>.
- [96] N. Francesco. Private communication.
- [97] **ALICE** Collaboration, B. B. Abelev *et al.*, “ $K^*(892)^0$  and  $\phi(1020)$  production in Pb–Pb collisions at  $\sqrt{s_{NN}}=2.76$  TeV,” *Phys.Rev.* **C91** no. 2, (2015) 024609, [arXiv:1404.0495 \[nucl-ex\]](#).
- [98] **STAR** Collaboration, B. Abelev *et al.*, “Mass, quark-number, and  $\sqrt{s_{NN}}$  dependence of the second and fourth flow harmonics in ultra-relativistic nucleus-nucleus collisions,” *Phys.Rev.* **C75** (2007) 054906, [arXiv:nucl-ex/0701010 \[nucl-ex\]](#).
- [99] **PHENIX** Collaboration, A. Adare *et al.*, “Scaling properties of azimuthal anisotropy in Au+Au and Cu+Cu collisions at  $\sqrt{s_{NN}} = 200$  GeV,” *Phys.Rev.Lett.* **98** (2007) 162301, [arXiv:nucl-ex/0608033 \[nucl-ex\]](#).
- [100] D. Teaney, J. Lauret, and E. V. Shuryak, “Flow at the SPS and RHIC as a quark gluon plasma signature,” *Phys.Rev.Lett.* **86** (2001) 4783–4786, [arXiv:nucl-th/0011058 \[nucl-th\]](#).
- [101] P. Huovinen, P. Kolb, U. W. Heinz, P. Ruuskanen, and S. Voloshin, “Radial and elliptic flow at RHIC: Further predictions,” *Phys.Lett.* **B503** (2001) 58–64, [arXiv:hep-ph/0101136 \[hep-ph\]](#).
- [102] **PHENIX** Collaboration, A. Adare *et al.*, “Deviation from quark-number scaling of the anisotropy parameter  $v_2$  of pions, kaons,

## BIBLIOGRAPHY

---

- and protons in Au+Au collisions at  $\sqrt{s_{NN}} = 200$  GeV,” *Phys.Rev.* **C85** (2012) 064914, [arXiv:1203.2644](#) [nucl-ex].
- [103] R. Snellings, “How much does the hadronic phase contribute to the observed anisotropic flow at the LHC?,” *EPJ Web Conf.* **97** (2015) 00025, [arXiv:1411.7690](#) [nucl-ex].
- [104] **STAR** Collaboration, L. Adamczyk *et al.*, “Centrality and transverse momentum dependence of elliptic flow of multi-strange hadrons and  $\phi$  meson in Au+Au collisions at  $\sqrt{s_{NN}} = 200$  GeV,” [arXiv:1507.05247](#) [nucl-ex].
- [105] **ALICE** Collaboration, B. Abelev *et al.*, “Measurement of electrons from semileptonic heavy-flavour hadron decays in pp collisions at  $\sqrt{s} = 7$  TeV,” *Phys. Rev.* **D86** (2012) 112007, [arXiv:1205.5423](#) [hep-ex].
- [106] **ALICE** Collaboration, A. Dubla, “Elliptic flow of heavy-flavour decay electrons in Pb–Pb collision at  $\sqrt{s_{NN}} = 2.76$  TeV with ALICE,” *J. Phys. Conf. Ser.* **509** (2014) 012062, [arXiv:1311.5429](#) [hep-ex].
- [107] N. M. Kroll and W. Wada, “Internal pair production associated with the emission of high-energy gamma rays,” *Phys. Rev.* **98** (Jun, 1955) 1355–1359. <http://link.aps.org/doi/10.1103/PhysRev.98.1355>.
- [108] **ALICE** Collaboration, B. B. Abelev *et al.*, “Neutral pion production at midrapidity in pp and Pb–Pb collisions at  $\sqrt{s_{NN}} = 2.76$  TeV,” *Eur. Phys. J.* **C74** no. 10, (2014) 3108, [arXiv:1405.3794](#) [nucl-ex].
- [109] **ALICE** Collaboration, B. B. Abelev *et al.*, “Production of charged pions, kaons and protons at large transverse momenta in pp and Pb–Pb collisions at  $\sqrt{s_{NN}} = 2.76$  TeV,” *Phys. Lett.* **B736** (2014) 196–207, [arXiv:1401.1250](#) [nucl-ex].

- [110] T. Sjostrand, S. Mrenna, and P. Z. Skands, “A Brief Introduction to PYTHIA 8.1,” *Comput. Phys. Commun.* **178** (2008) 852–867, arXiv:0710.3820 [hep-ph].
- [111] S. Agostinelli *et al.*, “Geant 4 simulation toolkit,” *Nuclear Instruments and Methods in Physics Research Section A: Accelerators, Spectrometers, Detectors and Associated Equipment* **506** no. 3, (2003) 250 – 303. <http://www.sciencedirect.com/science/article/pii/S0168900203013688>.
- [112] **ALICE** Collaboration, D. Lohner, “Measurement of Direct-Photon Elliptic Flow in Pb–Pb Collisions at  $\sqrt{s_{NN}} = 2.76$  TeV,” *J.Phys.Conf.Ser.* **446** (2013) 012028, arXiv:1212.3995 [hep-ex].
- [113] G. D’Agostini and M. Raso, “Uncertainties due to imperfect knowledge of systematic effects: General considerations and approximate formulae,” arXiv:hep-ex/0002056 [hep-ex].
- [114] G. D’Agostini, “Asymmetric Uncertainties: Sources, Treatment and Potential Dangers,” *ArXiv Physics e-prints* (Mar., 2004) , physics/0403086.
- [115] F. Bock. Master thesis, 2012. <http://www.physi.uni-heidelberg.de/~fbock/Masterthesis.pdf>. Physikalisches Institut at the University of Heidelberg.
- [116] T. Dahms. Master thesis, 2005. [https://www.phenix.bnl.gov/WWW/publish/tdahms/master-thesis/tdahms\\_thesis.pdf](https://www.phenix.bnl.gov/WWW/publish/tdahms/master-thesis/tdahms_thesis.pdf). Stony Brook University.
- [117] J. Podolanski and R. Armenteros, “Analysis of V-events,” *The London, Edinburgh, and Dublin Philosophical Magazine and Journal of Science* **45** no. 360, (1954) 13–30. <http://dx.doi.org/10.1080/14786440108520416>.
- [118] **ALICE** Collaboration, B. Abelev *et al.*, “Neutral pion and  $\eta$  meson production in proton-proton collisions at  $\sqrt{s} = 0.9$  TeV and

## BIBLIOGRAPHY

---

- $\sqrt{s} = 7$  TeV,” *Phys. Lett.* **B717** (2012) 162–172, [arXiv:1205.5724 \[hep-ex\]](#).
- [119] **ALICE** Collaboration, J. Adam *et al.*, “Direct photon production in Pb–Pb collisions at  $\sqrt{s_{NN}} = 2.76$  TeV,” [arXiv:1509.07324 \[nucl-ex\]](#).
- [120] Z. Qiu, C. Shen, and U. Heinz, “Hydrodynamic elliptic and triangular flow in Pb–Pb collisions at  $\sqrt{s} = 2.76$  ATeV,” *Phys. Lett.* **B707** (2012) 151–155, [arXiv:1110.3033 \[nucl-th\]](#).
- [121] G. Basar, D. Kharzeev, D. Kharzeev, and V. Skokov, “Conformal anomaly as a source of soft photons in heavy ion collisions,” *Phys. Rev. Lett.* **109** (2012) 202303, [arXiv:1206.1334 \[hep-ph\]](#).
- [122] C. Shen, U. Heinz, J.-F. Paquet, and C. Gale, “Thermal photon anisotropic flow serves as a quark-gluon plasma viscometer,” in *Proceedings, 6th International Conference on Hard and Electromagnetic Probes of High-Energy Nuclear Collisions (Hard Probes 2013)*. 2014. [arXiv:1403.7558 \[nucl-th\]](#). <http://inspirehep.net/record/1287938/files/arXiv:1403.7558.pdf>.



---

---

# Curriculum Vitae

---

---

**PostDoctoral Fellow** 2016-present  
*GSI Helmholtz Centre for Heavy Ion Research*

**PhD candidate (Subatomic physics)** 2011-2015  
*Utrecht University, the Netherlands*

**Thesis title:**  
*"Elliptic flow at different collision stages"*

**MSc. Physics (Physics of Fundamental Interactions)** 2008-2010  
*University of Turin and INFN, Italy*

**Thesis title:**  
*" $D^+$  meson reconstruction from  $K^-\pi^+\pi^+$  decay in  $pp$  collisions at  $\sqrt{s} = 7$  TeV with the ALICE detector"*

**BSc. Physics** 2005-2008  
*University of Turin and INFN, Italy*

**Thesis title:**  
*"Neutron photo-production in a close cavity for BNCT treatments"*

